Ultrafast laser-induced modification of optical glasses : a spectroscopy insight into the microscopic mechanisms

Konstantin Mishchik

▶ **To cite this version:**

Konstantin Mishchik. Ultrafast laser-induced modification of optical glasses : a spectroscopy insight into the microscopic mechanisms. Other [cond-mat.other]. Université Jean Monnet - Saint-Etienne, 2012. English. NNT : 2012STET4012 . tel-00966418

HAL Id: tel-00966418

https://theses.hal.science/tel-00966418

Submitted on 26 Mar 2014

HAL is a multi-disciplinary open access archive for the deposit and dissemination of scientific research documents, whether they are published or not. The documents may come from teaching and research institutions in France or abroad, or from public or private research centers.

L'archive ouverte pluridisciplinaire **HAL**, est destinée au dépôt et à la diffusion de documents scientifiques de niveau recherche, publiés ou non, émanant des établissements d'enseignement et de recherche français ou étrangers, des laboratoires publics ou privés.

Université Jean Monnet – Saint-Étienne
L'école doctorale "Sciences, Ingénierie, Santé"

Transformation photo-assistée de diélectriques pour l'optique par laser à impulsions ultra-brèves : études des mécanismes microscopiques.

par

Konstantin MISHCHIK

Thèse présentée pour obtenir le grade de Docteur en Sciences
en spécialité Optique, photonique et hyperfréquences.

Soutenue le 12 Juillet 2012 devant le jury composé de:

Prof. Bernard CHAMPAGNON	(Université Claude Bernard, Lyon)	Rapporteur
Prof. Javier SOLIS	(Instituto de Óptica – CSIC, Madrid)	Rapporteur
Dr. Matthieu LANCRY	(Université Paris 11 – Sud, Orsay)	Examinateur
Prof. Youcef OUERDANE	(Université Jean Monnet, Saint-Étienne)	Examinateur
Dr. Razvan STOIAN	(Université Jean Monnet, Saint-Étienne)	Co-directeur
Prof. Aziz BOUKENTER	(Université Jean Monnet, Saint-Étienne)	Directeur

Jean Monnet University – Saint-Étienne

Ultrafast laser-induced modification of optical glasses: a spectroscopy insight into the microscopic mechanisms.

by

Konstantin MISHCHIK

Thesis presented in partial fulfillment of the requirements
for the degree of Doctor of Philosophy
in the subject of Optics, photonics and hyperfrequencies.

Defended on the 12 July 2012 before the committee:

Prof. Bernard CHAMPAGNON	(Université Claude Bernard, Lyon)
Prof. Javier SOLIS	(Instituto de Óptica – CSIC, Madrid)
Dr. Matthieu LANCRY	(Université Paris 11 – Sud, Orsay)
Prof. Youcef OUERDANE	(Université Jean Monnet, Saint-Étienne)
Dr. Razvan STOIAN	(Université Jean Monnet, Saint-Étienne)
Prof. Aziz BOUKENTER	(Université Jean Monnet, Saint-Étienne)

Abstract

Local refractive index changes (RIC) are the building blocks of laser-induced optical functions in bulk transparent materials. These are essential for integrated photonic applications where model material such as fused silica plays a paramount role. Depending on the regime of laser interaction, particularly on the energetic dose, pulse duration and focusing conditions, ultrashort pulses can induce positive isotropic refractive index changes (usually denoted as type I) or produce self-arranged nanoscale layered structures resulting in form birefringence (type II). Using the birefringence and the associated anisotropic light scattering properties characteristic of the ordered nanostructures, polarization sensitive devices were designed and fabricated.

As these types of RIC have consequences in the functionality and the performances of 3D embedded optical devices, an investigation of the laser-induced structures is particularly useful. As primary stages of laser modification are crucial in the development of birefringent regions, we firstly investigated single and multiple pulse irradiation regimes. We observed that nanoscale reorganization is preceded by nuclei formation, which result from voids generation due to self-focusing effects, or from a bulk nano-roughness induced upon multiple pulse irradiation.

We applied photoluminescence (PLM) and Raman microscopy (RM) to investigate defect formation and glass network reorganization paths. These are major factors in changing the electronic properties of fused silica and, consequently, its optical constants. Reorganization of the glass network can equally affect the refractive index via the changes in glass density. These may be either positive or negative and we tried to expose the specific phenomena responsible for this antagonist behavior.

The proposed spectroscopy study distinguishes type I and type II regions by E'_δ and non-bridging oxygen hole centers (NBOHC) formation and distribution. Additionally, RM reveals signs of compaction of the glass network in the refractive index changes region. At the same time, zones with high concentration of NBOHC where no visible RIC and densification signs were detected. Assuming that these zones are precursors of permanent visible modification, where defects generation occurs as a result of bond breaking after self-trapped exciton relaxation, we propose a scenario of cold defect-assisted densification realized in type I irradiation regime. This, thereby, revises the densification paths in fused silica.

Résumé

Le changement local de l'indice de rfraction (CLIR) est l'élément constitutif des fonctions optiques créées par laser dans des matériaux transparents. Ce changement est essentiel pour les applications photoniques intégrées utilisant des matériaux comme la silice. Selon le régime de l'interaction et en particulier en fonction de la dose d'énergie déposée, de la durée de l'impulsion laser et des conditions de focalisation on peut induire un CLIR isotrope et positif (dit de type I) ou produire à l'échelle nanométrique des structures auto-arrangées prsentant une biréfringence (type II).

Nous avons utilisé ces deux types de modifications photoinduites par impulsion ultra brève pour concevoir et réaliser des composants optiques allant du simple guide canal enterré à des dispositifs sensibles à la polarisation.

En parallèle au développement d'applications photoniques nous avons étudiés les mécanismes microscopiques à l'origine de la modification des propriétés optiques des diélectriques utilisés (silice et BK7). L'étude a porté sur les effets photoinduits aussi bien par une impulsion unique que ceux dus à un train d'impulsions. Nous avons mis en évidence, par exemple, l'existence d'une phase précédant la réorganisation à l'échelle nanométrique conduisant l'apparition de l'anisotropie optique.

Nous avons appliqué les techniques de micro photoluminescence (MPL) et microspectroscopie Raman (MR) pour étudier la formation des défauts ponctuels et des chemins de réorganisation de la structure du verre. Les modifications photoinduites jouent un rôle important dans le changement des propriétés électroniques de la silice fondue et, par conséquent, de ses constantes optiques. Elles affectent ainsi l'indice de réfraction et peuvent conduire à une modification de la densité du verre.

L'étude spectroscopique a permis de dresser une cartographie des modifications photoinduites en distinguant les régions de type I et de type Il ainsi qu'en identifiants les défauts ponctuels associés : centres E'_δ et oxygènes non pontant (NBOHC). En outre, MR a révélé les zones ayant subi une compaction du réseau vitreux. Dans le même temps, nous avons identifiés des zones à forte concentration de NBOHC où aucun signe visible de CLIR n'a été détecté. Ces zones correspondant aux premières phases de modification de la structure du verre pourraient jouer le rôle de précurseur pour les modifications macroscopiques ; indice de réfraction et anisotropie optique. L'ensemble de ces résultats spectroscopiques nous a permis de revisiter les schémas de densification dans la silice et de proposer un scénario de densification à froid assistée par les défauts générés suite à la relaxation des excitons auto-piégés.

Contents

Chapter 1

Introduction

In the past decade, ultrashort laser sources have made a decisive impact on three-dimensional (3D) processing of transparent materials for photonic applications. At first, the short duration of femtosecond laser pulses allows to concentrate laser energy of only few μJ to intensity values reaching tens of TW/cm^2. That is enough to excite and modify even transparent materials via nonlinear mechanisms of energy deposition. Secondly, absorption processes developing on a few hundreds of femtoseconds impact directly the electronic system which occurring on a much shorter timescale than other effects related to the atomic network such as heat diffusion or thermo-elastic relaxation. This specific time decoupling of excitation and relaxation events allows to precisely control the interaction and produce modifications on a micrometric and submicrometric scales. The consequence is the formation of a local refractive index change (RIC) and the onset of an embedded optical functions. This is crucial for the concept of laser fabricated integrated optics, a field that presents paramount technological importance.

The use of transparent dielectrics has a particular interest. Translation of the single laser spot into the bulk of the dielectric material with the ability of irradiation to induce both positive and negative refractive index changes permits three dimensional photo-drawing of various optical components. For example, in many cases the positive refractive index variation is mandatory in waveguide writing [DMSH96]; however, the modulation of refractive indices opens the door to the achievement of more complex photonic devices. Present demonstrations include the fabrication of passive optical functions such as waveguides, couplers, gratings, binary data storage devices, lenses and Bragg gratings (see for example [IWNS06, GM08] and references therein), but also active optical devices like waveguide amplifiers and lasers [SSB+00, DVTO+07]. Thus, direct-writing of optical devices using ultrafast laser pulses has potential applications in telecommunications, optical sens-

ing and optical signal processing domains. The challenge is to optimize and upgrade their performances by developing better or novel optical functions related to local index variation.

During the development of laser photoinscription in the first years, mostly isotropic index changes associated with light transport were investigated. This is the typical regime for low-loss waveguiding. However, in the interaction of ultrashort laser pulses with specific materials (for example, with fused silica) a novel phenomenon occurs. Together with smooth material modification, the self-formation of organized volume nano-sheet arrays inside the laser traces leading to form birefringence was observed [KS08, THS08]. The resulting layered structures show different refractive indices with respect to the surrounding and are oriented perpendicular to the electric vector of the driving field. The type of modification depends on the regime of laser interaction, particularly on the energetic dose, pulse duration and focusing conditions and leads to a new class of optical polarization functions. Both regimes require further investigation of the responsible light-matter interaction processes.

For understanding the mechanisms causing the structural changes, various spectroscopic studies including photoluminescence and Raman spectroscopy were proposed in the literature. Luminescence was often reported in the laser damaged fused silica and considered as an effective way to characterize the glass structure in the modified regions. The number of works concerning defects producing in the femtosecond modified silica, however, is still small [WJS+99, CHRK03, KD03, ZRG+06, Rei06] and they do not give a complete and satisfactory picture. Additional information about atomic structure of modified fused silica is provided by Raman spectroscopy [CTRK01, SB02, ZRG+06, PSS08, BBS+08, STS+11], complementing the investigation procedure.

These observations reveal a particularly complex character of light-glass interaction. As a result, the following key mechanisms were considered as responsible for index changes: thermal mechanism (fictive temperature model), when higher density silica develops after fast quenching from a high-temperature melt [CTRK01]; non-thermal mechanism, when index changes occurs due to generation of color centers [ZRG+06], density changes resulting from defects-induced structural network reorganization (defect-induced densification) [DMSH96, HM98], and mechanical contributions, when compaction and rarefaction of material occur after pressure wave launch [GM97].

However, the role of each mechanisms in the material modification is yet not well understood and requires quantification. The investigation is moreover complicated by the different experimental conditions employed in various groups for providing the damage, that can provide non-general results and

lead to ambiguity of the conclusions. Moreover, several fundamental unresolved questions remain, which give incomplete understanding of modified silica structure. These issues involve specific band assignments and a clear addressing of the defect distribution in the laser-modified zones, characterizing different types of silica structure. Considering global rearrangements, there is no yet direct evidence if indeed melting and rapid quenching occurs or defect-caused densification takes place. Glass equally may experience a combination of defect formation and structural relaxation toward metastable equilibrium. Finally, the mechanism leading to form birefringence and its precursors is still unclear.

We therefore employed an extensive procedure involving spatial resolved coupled photoluminescence and Raman spectroscopy to obtain information allowing to investigate both defects formation and subsequent reorganization of the glass network on micrometric scale. The study involves a spatial and spectral parametric approach allowing to observe index transitions in different regimes of interactions. Thereby RIC zones can be directly associated with a specific network reorganization and, in addition, the sequence of involved relaxation mechanisms can be extracted from the measured data.

By understanding the relaxation mechanisms and by controlling them via selective energy deposition, we equally aim at promoting ultrafast lasers as microfabrication tools for processing bulk transparent materials. We attempt to follow the physical processes associated to laser-induced modification of bulk transparent materials, and we also seek for control factors in order to generate optical structures with arbitrary optical properties. This puts forward the challenge of defining the energetic and structural differences between the birefringent and the isotropic regions. This work provides thus preliminary steps to optimal laser processing of novel functionalities with several conceptual demonstrations of examples of complex light transport and polarization devices .

The thesis is organized as follows.

In Chapter 2 the topological and the electronic structure of fused silica are presented. The atomic structure of the ideal fused silica network is defined by the short- and medium-range order; the microscopic parameters characterizing such order are introduced. The influence of the medium-range order on the physical parameters of fused silica is considered based on the fused silica polymorphs. The real fused silica network is in addition characterized by the presence of various defects of the short- and medium-range order structure, that affects its electronic structure. Thus, the topological and electronic structure are the main factors affecting the refractive index of pure and modified fused silica. These aspects are reviewed in the corresponding sections.

Chapter 3 gives an overview of the mechanisms leading to permanent material modifications induced by ultrashort irradiation in fused silica. This includes photoionization processes strongly affected by the nonlinear propagation of the femtosecond laser pulses. Further deposition of energy into the network via various relaxation pathways is indicated. Several models leading to permanent refractive index changes such as thermal heating (fictive temperature model), pressure compaction, and defect-assisted densification are discussed while trying to elucidate their advantages in structural modification of fused silica network during the ultrafast writing.

In Chapters 4 and 5 the experimental irradiation setup is displayed and the procedure of photowriting of the permanent index traces is explained. Isotropic smooth modification of refractive index (type I) and birefringent (type II) types of traces can be usually written using different focusing and energetic conditions, thus processing windows are determined. A parametric microscopy study is performed using optical transmission and phase contrast microscopy. We equally consider secondary light emission generated during writing procedure. Monitoring of both coherent (harmonics generation) and non-coherent (luminescence) light emission allows *in situ* control of the developing birefringence and damage transition. Finally, using optimal laser pulse and focusing parameters, polarization sensitive devices are demonstrated.

Chapters 6 and 7 describe the results of spectroscopic investigation in fused silica. Combining the means of photoluminescence and Raman spectroscopy, a rather detailed picture of the structural changes and their spatial repartition could be extracted. If photoluminescence provide information about the defect structure of the network, Raman spectroscopy gives information about global network reorganization. Based on available measurement data, we discuss the role of different pathways of energy relaxation that may cause the change of refractive index during ultrafast writing.

Relying on the results obtained for fused silica, a model glass with a relatively simple structure, the experiments were expanded on borosilicate crown BK7 multicomponent glass that preserves a main silicate network. Important aspects of BK7 glass processing and PL and Raman spectroscopy results are described in Chapter 8.

Finally, the conclusion part resumes the main experimental results and the discussion section, putting forward a synthesis of the proposed transformation scenarios. A perspectives section offers an emphasis on the expected impact of the fundamental questions regarding laser-assisted transformation of fused silica approached here and on the associated photonic applications as well.

Chapter 2

Fused silica structure and optical properties

Amorphous fused silica (a-SiO_2) is the pure form of the silica glass. A concentration of impurities lower than 0.5% makes it optically transparent in a wide spectral range (from 180 nm in the ultraviolet region to 2.5 μm in the infrared region). Apart from its optical properties, it is mechanicaly stable, highly chemical inert and has a high softening temperature (1585 °C). All these characteristics determine a wide use in manufacturing of optical components. The structure of silica was considered in numerous books and monographies [Sos65, Bru70, Bru71, Hea94]. Here several properties important in the context of the present work will be presented.

2.1 Local order in silica structure

The structural unit of most silicon dioxide allotropic forms is the SiO_4 tetrahedron. It consists of four oxygen atoms placed in the corners of the tetrahedron, with a silicon atom in the center. The bonding between Si and O atoms is sufficiently strong that it forms very rigid structures with a O–Si–O angle $\phi_T = \cos^{-1}(-1/3) \approx 109.5°$. This type of bonding is partially covalent and partially ionic bond, with an excess of negative charge on the oxygen atoms [Pau60].

In contrast to the various polymorphs of crystalline quartz, fused silica has an amorphous (non-crystalline) structure. This means that long-range order between atoms is not defined, and only short-range order exists. Connected to each other, the tetrahedra form a three-dimensional continuous network which could be characterized by the following local order parameters as indicating in Fig. 2.1:

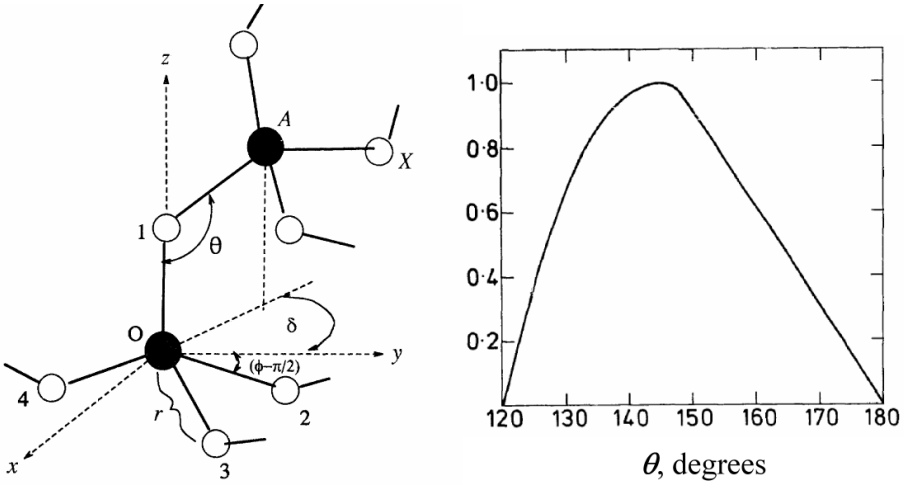

Figure 2.1: a) Segment of SiO_2 network presenting its local order parameters: the length of the Si–O bond r, interbonding Si–O–Si angle θ, and intertetrahedral tilt angle δ [BGME93]. b) Statistical distribution of the Si–O–Si bonding angles in amorphous SiO_2, as determined from X-rays diffraction data by [MW69].

- mean distances between atoms. The most important parameter is the mean equilibrium Si–O bond length r, however, the mean distances between O–O and Si–Si could also be considered. The distances between Si–O (1.6 Å), O–O (2.6 Å) and Si–Si (3.2 Å) are well known from X-ray and neutron diffraction data;

- mean Si–O–Si bridging angle θ, formed by two adjoining tetrahedra. It could vary between 120 and 180 degrees, with the mean value of 144° (Fig. 2.1b);

- mean dihedral or tilt angle, δ, between adjoining SiO_4 tetrahedra, that share a common oxygen atom.

The exact structure of the network, however, are not yet established. The different models were proposed from the early concepts of random network [Zac32] to a more recent model assuming existence of microscopic clusters in silica network of ≈20 Å, where correlations between its structural parameters are well defined [DBA90, dG02]. But more important is that each network will be characterized by its own r, θ, and δ averaged on some macroscopic range. This representation give us a model of ideal glass, which assumes that each oxygen atom is connected to two atoms of silicon, that means a fully

polymerized network. However, in the real case there are always oxygen atoms which are connected only with one Si. Such atoms are called non-bridging oxygens (NBO). Depending on the number of terminating oxygen atoms, the SiO_4 tetrahedra could be labeled as follows: Q_4, Q_3, Q_2, Q_1, Q_0. This implies fully polymerized tetrahedra with no NBO, and silicon atoms bonded with 3, 2, 1, 0 bridging oxygen respectively.

Despite the presence of terminating oxygen atoms, the overall topology of the fused silica network consists of closed loops containing a certain number n of –Si–O– segments called n-membered rings, $(–Si–O–)_n$. That is why, usually speaking about the fused silica structure, one could operate with ring statistics, which is the distribution of rings with different n across the whole network. Typically fused silica consists from rings where n varies from 3 to 8, with the mean value 6, [BGME93, AK03].

In the present work two types of high-purity fused silica glass samples were used. *Corning 7980-5F* is a synthetic glass, produced by hydrolysis of $SiCl_4$ molecules when spraying into oxygen-hydrogen flame. According to Brückner classification of commercially available glasses with respect to their properties and structure, this is type III glass [Bru70]. This is the so called "wet silica" since a high concentration of OH-groups in the order of 800–1000 ppm (in weight fractions) is present. It does not possess metallic impurities, however, it could contain Cl in quantities less then 1 ppm. The other sample being used is Heraeus *Infrasil* glass. This is type I silica glass, produced by fusion from natural quartz in vacuum. It contains a very low amount of OH-groups (less then 8 ppm), so it is also called "dry silica", but it is rich in metallic impurities (∼20 ppm).

In the present work most experiments were performed using *Corning 7980* glass, and only in some specific experiments *Infrasil* was chosen particularly for investigating the effects of the OH-group impurities.

2.2 Silica polymorphs

Fused silica is just one of the silica polymorphs (modifications of a substance having the same chemical formula but different structure). Most of these polymorphs are crystalline and constructed with the tetrahedral SiO_4 units (common for fused silica). Quartz is the most wide-spread polymorph. It is stable until 573 °C, when it transforms to its β-phase. Gradually increasing temperature one can obtain tridymite and crystobalite forms until reaching the temperature of ∼1700 °C when crystobalite melts. Polymorphs produced this way are stable only at high temperatures so they are called β or "high" phases. However, by slow cooling the material, their α or "low" phases can

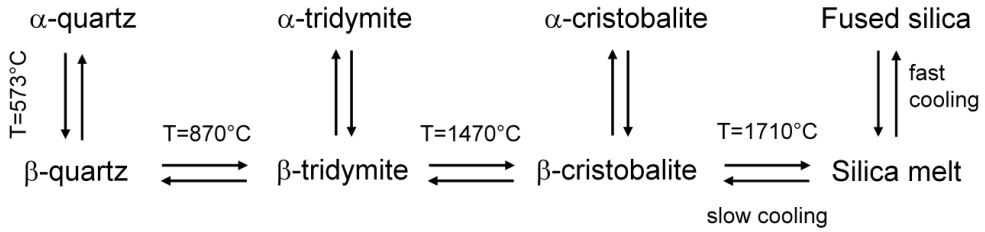

Figure 2.2: Diagram of the phase transition paths between silica polymorphs at 1 atmosphere pressure, as controlled by temperature.

be reached. The diagram of the phase transitions between major silica polymorphs is presented in Fig. 2.2. Some polymorphs like coesite and stishovite can be produced not only at high temperatures but also under high pressures.

Since the chemical composition of polymorphs is identical, the variety of their physical and optical properties is determined only by their network organization. This subject is very important in the context of this work, because in fused silica a connection between network reorganization and changes in its physical and optical properties can be relatively easily established. This knowledge may be directly used for characterization of changes induced by laser processing of silica (a rather simple glass) and even for more complex silicate glasses. Table 2.1 includes the data on the properties of major silica polymorphs, such as refractive index and density, and also structural characteristics like mean bonding distance, interbonding angle, and ring statistics.

The main observation coming from the Table 2.1 is the strong correlation between the refractive indices of polymorphs and their densities. Plotting them on the graph (Fig. 2.3), one can observe the linear dependency of the refractive index versus density, with the slope $dn = 0.44 d\rho/\rho\,\mathrm{cm}^3/\mathrm{g}$. This behavior is in agreement with Lorentz-Lorenz formula (see discussion later in section 2.4), which predicts a similar slope. That makes the density change as the major factor of refractive index variation. A deviation from this trend, which appears in cases of β-quartz and β-cristobalite could be explained by changing the molar polarisabilities with density [SO97, Lit09].

Table 2.1: Silica polymorphs.

Name	Refractive index[1,2]	Density[2] (g/cm^3)	r(Si–O) (Å)	θ(Si–O–Si)	Rings	References
Fused silica	1.458	2.20	1.62	144	$\langle 6 \rangle$[3]	[Bru70, MW69]
α–Quartz	1.549	2.65	1.61	143.6	6	[LPW80, Kih90, HG91]
β–Quartz	1.537	2.53	1.59	153.4	6	[Kih90, TKD01, HG91]
α–Tridymite	1.471	2.25	1.59	152.8	6	[Gra67, Gra01, Bau77]
β–Tridymite	—	2.23	1.56	171.7	6	[Dol66]
α–Cristobalite	1.484	2.32	1.60	146	6	[Dol65, Pea73]
β–Cristobalite	1.468	2.28	1.61	148	6	[Pea73]
Coesite	1.596	2.92	1.61	150	4,8	[SCS62, LP81]
Keatite	1.519	2.50	—	—	5	[Kea54, SKV59]
Moganite	1.527	2.55	1.61	143.5	4,6,8	[min, HP01, KH94]
Stishovite[4]	1.81	4.29	1.78	—	—	

[1] Mean refractive index is presented. Averaging accounts for the dispersion and the incidence of the light with respect to crystallographic axis in crystalline solids.

[2] Data from [min, web, Bru70, Sos65, Hea94, Sos29a, Sos29b, LSB06, Gra67].

[3] Angle brackets mean the averaged value.

[4] Elementary unit of stishovite is Si connected with 6 atoms of O, so the packing of stishovite is more dense.

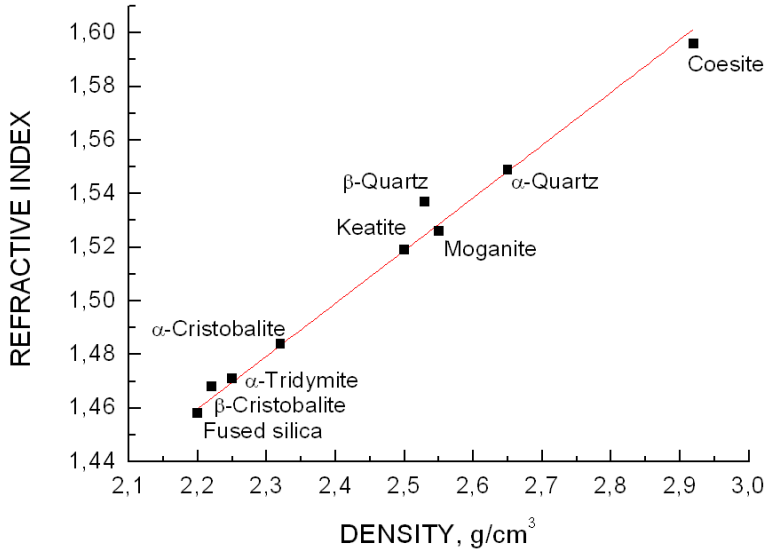

Figure 2.3: Dependency of the refractive index on the density of different 4-coordinated silica polymorphs, showing a slope of $dn = 0.44 d\rho/\rho\,\mathrm{cm}^3/\mathrm{g}$.

In addition, one should emphasize the correlation between interbonding angle θ and the density of polymorphs. This correlation is particularly visible in low-high (α–β) phases transformation of quartz and cristobalite. Lower density phases have higher interbonding angles (up to 180 degrees for trydimite). Bond lengths are equally changed, but this factor affects density to a lesser extent. The same tendency has been observed for pressure compacted quartz crystobalite and coesite [DP94]. Thus, the packing of silicon tetrahedra is more efficient when the interbonding angles are lower

It is difficult to state if the ring statistics has a particular influence on the density of polymorphs. Ring statistics, however, should affect their mechanical properties. The existence of less rigid 8-membered rings allow lower strain accumulation in the network if compare to 6-membered ones [Tho83]. Thus, coesite can be efficiently compacted. In addition, it seems that the appearance of 8-membered rings is accompanied by 4-membered ones. The latters occupy a lower volume and this is another argument for efficient compaction of coesite. The denser phase is, however, unstable. Since the vibrations of these rings have characteristic frequencies, Raman spectroscopy can be employed for revealing ring statistics [SMN81, GBME84, KH94].

Amorphous fused silica also has a variety of structures. The useful ap-

proach of the structure assignment is based on a thermodynamics description, where the values r, θ, δ discussed above are not random, but distributed according to some function of the temperature of the glass. In this case each type of a silica could be addressed using a scale of so-called *fictive temperatures*, T_f. The concept of fictive temperature was first introduced by Tool [Too46] and it characterizes the non-equilibrium state by the temperature where, if exposed to it, the glass would be in equilibrium with its environment without physical or chemical adjustment (structural relaxation).

In practice, glass structure is achieved by rapid cooling of the glass melt. Thus, one can consider the glass structure with the as-determined fictive temperature as an equilibrium structure of fused silica at a higher temperature, which was frozen-in during its fast quenching to the room temperature. On the other hand, if the cooling rate is very slow, then the silica melt can be crystallized to β-crystobalite and later to α-quartz – the most stable form of silica polymorphs. On the contrary, if the cooling is going fast, then the network during its reorganization cannot follow the equilibrium path ending in a crystalline structure. Thus, solidification happens with lack of crystallinity and with the generation of n-membered rings with n different then 6. This discussion will be in Sec. 3.3 in the context of laser irradiation process.

It should be noted that the fictive temperature model does not uniquely define the structural state of a glass and such one-parameter description has only a limited quantitative significance [Rit56]. Firstly, it is assumed that equilibrium structure should be achieved before quenching; however, it can be not the case in fast structural changes happening after laser irradiance. Secondly, the more correct description of the structure should not be based on only one parameter (temperature) but it should equally include a pressure variable, since quite high pressure values can be reached during laser-matter interaction. The thermodynamic state functions (e.g. enthalpy $H(S, p)$), therefore, should be used for structure characterization.

2.3 Intrinsic defects

In the following a discussion about the physical and chemical imperfections of the glass matrix is given. All imperfections in the fused silica network structure such as different violations of short-range order are called defects. These structural changes are accompanied by changes of the electronic structure of the material (color centers). The latters can be detected, for example, using absorption, photoluminescence (PL), or electron paramagnetic resonance (EPR) spectroscopy.

Absorption and PL spectroscopy methods are based on changes in the

optical properties. The procedure relies on the fact that changes of the electronic structure of the material induced by defects are equivalent to the appearance of the additional energy levels on the energy level diagrams. If new level states are located in the forbidden band of the silica glass, then transitions in between these levels, to conduction or from valence bands determine the appearance of characteristic absorption and photoluminescence characteristics.

Moreover, in the case when the generated defects have unpaired electrons, they will show paramagnetic properties and, therefore, they can be studied by the EPR technique due to the capabilities of this method to sense the atomic environment of the unpaired electron of paramagnetic defects.

Before considering defect structures, it is important to take into account the electronic structure of silica, which is illustrated in Fig. 2.4. As it was reported [CS77, OR83], its valence band is composed of the electronic states of the $2p$ orbital electrons of oxygen and the ones located on the Si–O bonds. The band is rather wide and the corresponding states exists in the range 0 to -26 eV. The most important part of it is the top of the valence band situated from 0 to approximately -5 eV, since these states play an important role in the electronic transitions of many defects considered below. It was shown that the top of the valence band is predominately composed of nonbonding oxygen $2p$ orbitals (fully occupied state shown in Fig. 2.6a). The conduction band, placed 9 eV above the valence band is composed from $3s$ oxygen states, as well as significant part of p and d silicon states.

2.3.1 Stable point defects

Today numerous reviews exist concerning optical and spectroscopic properties of various defects in silica, see for example [Sku00, Gri00, Gri91, Sku98, PI98, Sku01, SHHK05] and the references therein. We shall first consider just intrinsic defects which are usually observed in laser damaged fused silica.

We will be concerned with relatively long-living defects, so they can be detected long time after the damage even at room temperatures. Their topological structures, electronic properties, optical absorption and photoluminescence bands are summarized in Figures 2.5, 2.6 and Table 2.2.

$\mathbf{E}'$ center. These paramagnetic centers are one of the most common centers existing in silica glass, being usually detected by EPR or by a characteristic band absorption at 5.7 eV. It can be presented as a Si dangling bond with a trapped electron generated in following reaction,

$$\equiv\text{Si–O–Si}\equiv \rightarrow \equiv\text{Si}\cdot + \cdot\text{O–Si}\equiv, \tag{2.1}$$

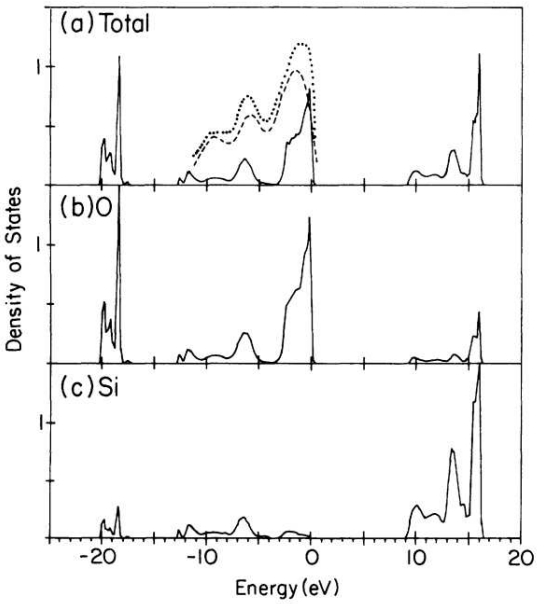

Figure 2.4: a) Calculated electronic density of states (DOS) of silica with the photoemission data (dotted and dash lines). b) and c) Projection of DOS on the O and Si states. Data are taken from [OR83]

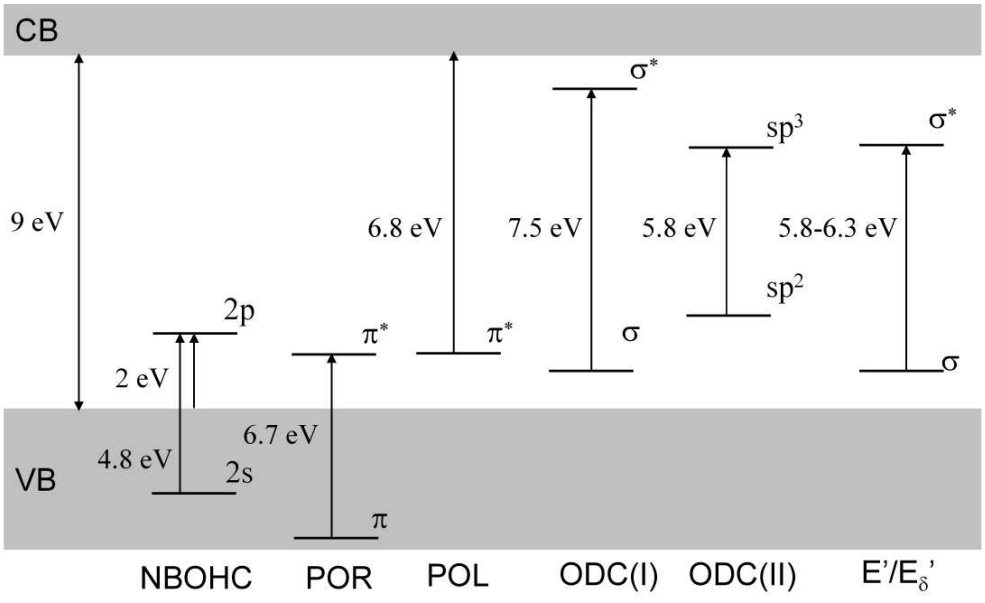

Figure 2.5: Band gap structure of permanent silica defects from Refs. [OR83, PI98, SMM+05].

where sign "–" means single bond and "·" is an unpaired electron. This reaction can happen after breaking of strained Si–O bonds and often occurs after relaxation of self-trapped excitons (STE, a discussion concerning these unstable defects will be given later). From the family of E' centers one can emphasize E'_δ [see for example [GF86, KKP+00, SMM+05, Bus07] and references therein]. As suggested by different models, structurally, this center can be presented as an unpaired spin shared by a cluster of several Si atoms, where the amount of Si atoms in the clusters varies from 2 to 5. However, the most plausible explanation is that only two silicon atoms share one electron [SMM+05]. Therefore, it is a positively charged center, which can be represented by the structural formula $\equiv Si\cdot^{+}Si\equiv$. With this type of defect a photoluminescence band at 2.2 eV (560 nm) could be assigned. Firstly reported for γ-irradiated oxygen deficit glasses, it was observed by EPR means. Its existence was then confirmed in other type of silicas too. Nishikawa *et al.* [NWI+96] found a strong correlation between the 2.2 eV luminescence band emitted by Si implanted fused silica excited with a 325 nm wavelength radiation from a HeCd laser source and the EPR signal of E'_δ centers. Later, 2.2 eV luminescence band was reported in fused silica damaged with nanosecond pulsed UV laser under different excitation conditions [KD03].

Oxygen deficiency center, ODC(I). This is a neutral oxygen vacancy, having the formula ($\equiv$Si–Si$\equiv$). For the reason that these are diamagnetic centers, EPR technique cannot be applied to them and most information comes from optical studies. ODC(I) has an absorption peak centered at 7.6 eV and two PL bands at 2.7 and 4.4 eV. One of the possible mechanisms of forming ODC(I) is the relaxation of self-trapped excitons, because one of the channels of STE de-excitation goes with the dissociation of molecular oxygen out of the silica network according to the reaction

$$\equiv Si–O–Si\equiv \rightarrow \equiv Si–Si\equiv + O. \tag{2.2}$$

The second mechanism arises from a close structure between E' and ODC(I) centers: under heat treatment and UV exposure of sample these defects can transform reciprocally into each other [Sku98]

$$2 \equiv Si\cdot \leftrightarrow \equiv Si–Si\equiv. \tag{2.3}$$

Divalent Si, ODC(II). For one of the observed defects which has absorption located at 3.15, 5.05 and 6.9 eV and two photoluminescence bands at 2.7 eV (460 nm) and 4.4 eV (280 nm), a model of divalent Si, i.e. atoms of Si only with two bridging oxygens (=Si:) was proposed. This model is still argued, and a different assignment of these bands, corresponding to unrelaxed oxygen vacancy can be proposed.

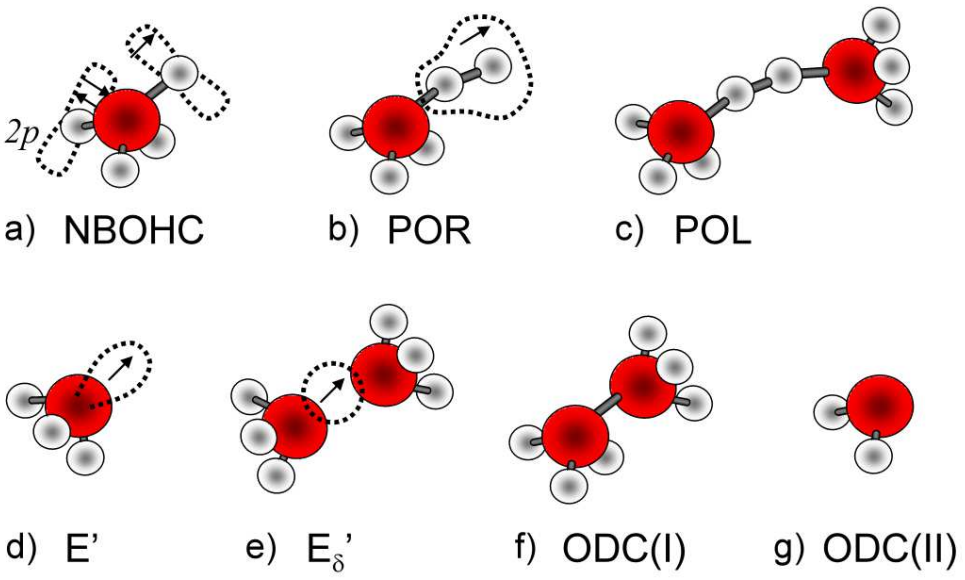

Figure 2.6: Structural models for oxygen excess defects: a) non-bridging oxygen hole center, NBOHC, b) peroxy radical, POR, c) peroxy linkage, POL; and defects with deficit of oxygen: d) $E^{'}$ and e) $E^{'}_{\delta}$ centers, f) relaxed oxygen vacancy, ODC(I) and g) divalent silicon, ODC(II). Spin states are indicated by the arrows.

Non-Bridging Oxygen Hole Center (NBOHC). These defects belong to the group of oxygen-excess centers, occurring in oxygen-rich silica, but they are also generated in laser-, particle-, radiation–damaged, and shock–wave compressed silica. The commonly accepted model depicts this center as a dangling O bond with an unpaired electron on his $2p$-orbital. It has two characteristic absorption bands situated at 2 and 4.8 eV and photoluminescence at 1.9 eV (650 nm) upon excitation in these two absorption bands, with the decay constant of approximately $\sim$10 μs. The 2 eV absorption bands correspond to a transition from the $2p$-orbital belonging to one of the three nearest-neighbor oxygen atoms (as schematically outlined in Fig. 2.6) to the half-filled orbital of the non-bridging oxygen [Sku01]. For the 4.8 eV absorption band a transition from the Si–O σ-orbital to the half-filled $2p$ orbital of the non-bridging oxygen was proposed. This defect can be generated either by breaking strained Si–O bonds as described above in Eq. 2.1 forming a pair of NBOHC and $E^{'}$ centers or by breaking silanol Si–O–H groups forming a single NBOHC.

Peroxy radical (POR). One commonly studied defect is the peroxy

Table 2.2: Optical absorption and associated photoluminescence band peak positions of intrinsic defects in silica glasses.

Defect	Absorption peak position, eV	Photoluminescence band peak position, eV (nm)
E' center	5.78	
E'_δ center	∼5	2.2 (560)
NBOHC	1.97, 4.8	1.9 (650)
ODC(I)	7.6	2.7 (460), 4.4 (280)
ODC(II)	3.15, 5.05, 6.9	2.7 (460), 4.4 (280)
POR	1.9, 4.8, ∼7	
POL	6.4	
Interstitial O_2	>6.5, 1.621, 0.975	0.975 (1270)
Interstitial O_2^-	3.8, 4.4, 5.2	2 (590)
Interstitial O_3	4.8	0.975 (1270)

radical, particularly because in the EPR spectroscopy it often dominates the EPR spectra in oxygen-excess glasses. As other defects above, it equally involves a dangling bond center ≡Si–O–O· with an electron localized on the O–O π orbital. Two absorption bands at 1.9 eV and 7.7 eV were assigned to it; however, there is certain indications that the 4.8 eV band is also related to PORs [Gri91]. Isochoric annealing of γ-irradiated silica samples shows an increase of concentration of POR accompanied by a decrease in the concentration of NBOHC and E' centers [GM98] indicating an inter-relation. This can be explained by the reaction of these defects with atomic oxygen, which is generated by dissociation of molecular oxygen or ozone during thermal bleaching:

$$O_3 \rightarrow O_2 + O, \tag{2.4}$$

$$\equiv Si\cdot + O_2 \rightarrow \equiv Si–O–O\cdot, \tag{2.5}$$

$$\equiv Si–O\cdot + O \rightarrow \equiv Si–O–O\cdot. \tag{2.6}$$

An opposite trend of the POR and NBOHC pair appears during 5 eV UV light exposure. The concentration of POR decreases, while the concentration of NBOHC increases. The probable reaction for POR photobleaching is:

$$\equiv Si–O–O\cdot + \hbar\omega \;\rightarrow\; \equiv Si–O\cdot + O. \tag{2.7}$$

Another mechanism of this defect generation was proposed by Edwards and Fowler [EF82]. Accordingly, a peroxy linkage (see below) is involved in a

dissociation process:

$$\equiv\text{Si–O–O–Si} \rightarrow \equiv\text{Si–O–O}\cdot + \cdot\text{Si}. \tag{2.8}$$

Peroxy linkage (POL). The POL defect is a diamagnetic center, which is described by the formula ≡Si–O–O–Si≡. It has an absorption band around 6.4 eV. The defect can be formed by mobile oxygen which associates with nearest bridging oxygen. The assignment of any absorption or PL to POL remains, however, controversial. For example, it was shown that 3.8 eV absorption band could be related to this type of defects [NTO+89]; however, more likely, it is attributed to interstitial Cl_2 [AKM+91, KHSH05]. Additionally, this assumption is not supported by theoretical estimations [PI98].

Interstitial molecular oxygen O_2 and ozone O_3. It was mentioned above that atomic oxygen can be generated during laser modification of fused silica by different ways. Being a very reactive chemical element, it tends to form other defects incorporated into the silica network or to form molecules if two or three interstitial oxygen atoms react with each other. The generated molecular oxygen and ozone being quite stable molecules, can travel freely in the bulk of fused silica. The diffusion coefficient for the temperature range of 1200–1500 K can be estimated by formula

$$D = D_0 \exp\left(-Q/kT\right), \tag{2.9}$$

where pre-exponent D_0=6.7×10^{-5} cm^2/s , Q=1.01 eV is the activation energy for high-OH content glasses and T is the temperature of the glass [KKH+05]. Extrapolating this ratio for higher temperatures the diffusion coefficient D ∼2×10^{-7} cm^2/s for the temperature T=2000 K near the softening point can be obtained. For the characteristic time of resolidification $t = 1\,\mu$s, a diffusion length $l_d = 2\sqrt{Dt}$ can be estimated in the order of 10 nm. This is enough to observe oxygen separation in the laser affected zone.

Molecular oxygen can be detected by several absorption bands at 0.975 eV and 1.6 eV bands and associated photo-emission of radiation at 0.975 eV, but also by its characteristic Raman scattering at 1550 cm^{-1}. With the O_2^- centers several absorption bands at 3.8 eV (weak), 4.4 eV and 5.2 eV were connected [Rol79] as well a complex luminescent band centered at about 2 eV (620 nm) and composed with equidistant smaller bands placed at 0.11–0.12 eV from each other in the green–IR spectral region [RLK61, BS70, FSS07]. The latters come from the luminescent transitions of the higher vibrational states of O_2^- molecules.

We equally point out on the instability of O_2^- and O_3 molecules. For example, ozone molecules can be photodestructed by photons with $\hbar\omega >$ 4 eV.

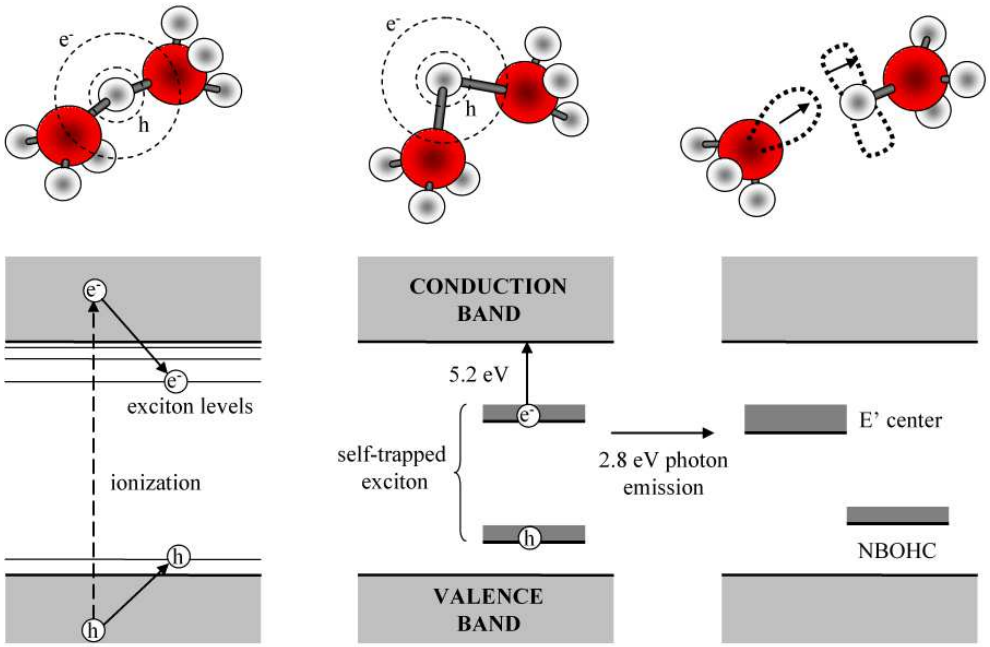

Figure 2.7: Structural model and schematic diagram of STE generation and of its relaxation involving E′-center and NBOHC formation

2.3.2 Self-trapped excitons

A particular defect of unstable nature appears when the electron can be directly transported to the conduction band, leaving a hole in the valence band. This happens after laser excitation by a multiphoton absorption process. An electron and a hole can be bounded together by Coulomb forces, collectively refereed as exciton; electrically neutral electronic excitation. In materials with a small dielectric constant, the Coulomb interaction between an electron and a hole may be strong and the excitons, thus, tend to have a small diameter, of the same order as the interatomic distance (so-called Frenkel excitons). In a deformable lattice (with a high polarization of the matrix) excitons tend to self-trap. That leads to charge and energy localization. Since the self-trapped excitons (STE) are means of channeling electronic excitation, a major source of interest towards them comes from further energy transfer into atomic processes such as network defect formation. Generation of excitons equally leads to the appearance of additional levels below the conduction band border, that changes the optical properties of the glass.

Modeling of the self-trapped excitons in crystalline SiO_2 [FHS90, SS90] supports a picture of this defect as a hole primarily localized on an oxygen

and an electron primarily localized on a neighboring silicon (Fig. 2.7). Localization of the hole results in a small atomic displacement of oxygen atom that deepens the potential well where the carrier is situated. This constitutes the origin of the self-trapping phenomena. This oxygen being displaced substantially from its regular lattice site, distorts the silica network and weakens the Si–O–Si bond. Further displacement of the oxygen atoms results in the formation of dangling oxygen and silicon bonds, which represent NBOHC and E′-centers according to Eq. 2.1 or complete liberation of oxygen with ODC(I) formation according to Eq. 2.2. Each relaxation channel is correlated with the formation of transient and permanent lattice defects.

Self-trapping and subsequent relaxation of these defects, allow to observe optical changes either at very short timescales after the pulse arrival or at low temperatures. To this extent, the dynamics of femtosecond laser interaction with fused silica was investigated intensively in the last decades. Transient interferometry measurements performed in the frequency and time domains provide essential information on the real and imaginary parts of the refractive index changes. This allows to observe the dynamics of excited carriers in dielectrics. By implementing such time-resolved techniques in SiO_2 it was revealed that the excitons self-trap in time on a scale of the order of 150 fs after free-carriers generation [SG93, ADS+94, MGD+97, QGM+99] in self-induced matrix deformations. Transient absorption experiments show an increase of absorption at 5.2 eV, which corresponds to the peak of the STE absorption band [PDGM96]. Finally, after approximately 1 ns [GGL+10], when STEs recombine, they produce a characteristic luminescence at 2.8 eV [JGM+92, GMP+96, RCS+07].

2.4 Optical properties of fused silica

The aim of this section is to give an overview of physical phenomena responsible for changes in the optical properties of fused silica e.g. absorption coefficient, reflectivity and refractive index. The relation between the microscopic properties of matter either at structural or at electronic level and the macroscopical optical properties will be outlined.

It is known that the modern theory of dispersion is based on existing charges (electrons and ions) in solid materials. In amorphous dielectrics, the mean charge and the mean dipole moment are equal to zero, so electromagnetic field of this dipoles is also equal to zero. However, in an external and periodically changing electric field $\mathbf{E}$, electrons and ions are moving out of their equilibrium states and induced dipoles appear. The ensemble of these oscillating dipoles creates its own field $\mathbf{P}$, which superposes with the external

one. Consequently, an electric displacement field $\mathbf{D}$ exists in the bulk.

$$\mathbf{D} = \varepsilon_0 \mathbf{E} + \mathbf{P}. \tag{2.10}$$

Here ε_0 is the vacuum permittivityIn linear optics it is assumed there is no contribution to the field from other dipoles and the induced electric field $\mathbf{P}$ is proportional to the incident field $\mathbf{P} = \varepsilon_0 \chi \mathbf{E}$, where χ denotes for the permittivity of material. Therefore, $\mathbf{D}$ writes as

$$\mathbf{D} = \varepsilon_0 (1 + \chi)\mathbf{E} = \varepsilon \mathbf{E}, \tag{2.11}$$

where ε is the dielectric constant. This relation determines the propagation properties of the waves in the media, since, according to Maxwell's equation, ε is proportional to the n^2, where n is the refractive index of the material. Thus, the refractive index depends on the permittivity χ, which in its own way is a function of the number of oscillators (density of material ρ) and their polarizabilities α (in fact α is a tensor, but because of the random distribution of dipoles in the amorphous media one can use mean polarizability which is scalar). In solids, where the field acting on the dipole is affected by surrounding dipoles, the local field should be considered. This leads to the Lorentz-Lorenz (Clausius-Mosotti) relation between refractive index and the material properties

$$\frac{n^2 - 1}{n^2 + 2} = \frac{\rho}{M}\alpha, \tag{2.12}$$

where ρ is the material density and M is the molar weight of glass. Differentiating both left and right parts, this equations can be rewritten in a form showing a dependency of the refractive index change with the densification of silica $d\rho/\rho$:

$$dn = \frac{(n^2 - 1)(n^2 + 2)}{6n}(1 + \Omega)\frac{d\rho}{\rho}. \tag{2.13}$$

Here Ω defined as $(d\alpha/\alpha)/(d\rho/\rho)$ is the ratio of the relative polarizability change to the relative density change. A comparison of previously determined values of Ω suggests that it depends upon the origin of densification and the chemical composition of glass [SO97]. In cases where fused silica is irreversibly compacted, a value of -0.19 ± 0.04 for Ω is consistently found. Therefore, for fused silica having a refractive index $n = 1.459$ for green light, we obtain the relation $dn = 0.43 d\rho/\rho$, which coincides with the value $dn = 0.44 d\rho/\rho$ obtained from the slope of the refractive indices of silica polymorphs plotted as a function of their densities (Fig. 2.3). For elastically (reversible) compacted glasses, a value of -0.38 for Ω was found [VSR66]. Thus, the ratio $dn = 0.33 d\rho/\rho$ can be obtained, that explains a deviation from the general behavior in α–β transition of quartz and cristobalite.

In general, a material cannot polarize instantaneously, so a response to an applied field as a function of time is used:

$$\mathbf{P}(t) = \varepsilon_0 \int_{-\infty}^{t} \chi(t - t^{'})\mathbf{E}(t^{'})dt^{'}. \tag{2.14}$$

Instead of considering the variable field in the time domain, one can expand the polarization field in Fourier series as a sum of monochromatic components $\mathbf{P}(\omega) = \varepsilon_0\chi(\omega)\mathbf{E}(\omega)$. Equivalently to Eq. 2.11 we can write:

$$\mathbf{D}(\omega) = \varepsilon(\omega)\mathbf{E}(\omega), \tag{2.15}$$

where

$$\varepsilon(\omega) = \varepsilon^{'}(\omega) + i\varepsilon^{''}(\omega), \tag{2.16}$$

is the complex dielectric function.

In the same way, polarizability could be thought as a function of frequency $\alpha(\omega)$, having different properties in different spectral ranges. The total polarizability can be divided in three parts: electronic (due to the displacement of the electronic shells around the nuclei), ionic (due to the displacement of charged ions) and dipolar (due to the reorientation of dipoles in the electric field) are all with their particular time and spectral characteristics. However, at the optical frequencies only the electronic part has main contribution [Kit53], so we will not account for the other terms. Finally, optical properties defined by the state of the electrons (since the optical responses of free and bound electrons are different) and their surroundings. We can therefore distinguish particular behavior for free and bound carriers.

Free electrons generated during the interaction with femtosecond laser pulses endow the material with metallic properties. Together with bond electrons they induce ultrafast changes to its optical properties:

$$\tilde{\varepsilon} = \varepsilon + \Delta\varepsilon_{Drude} + \Delta\varepsilon_{tr} \tag{2.17}$$

where ε is the normal dielectric function, $\Delta\varepsilon_{tr}$ represent changes induced by the transient defects and $\Delta\varepsilon_{Drude}$ is contribution of free electrons. The latter depends on the concentration of conduction electrons $n_e(t)$ and could be described in first approximation by Drude model:

$$\Delta\varepsilon_{Drude} = -\frac{n_e e^2}{\varepsilon_0 m\omega^2}\frac{1}{1 + i\frac{1}{\omega\tau_D}} \tag{2.18}$$

where m denotes the optical effective mass of the electrons and τ_D is the Drude damping time.

The dynamics of such ultrafast changes of the dielectric function, however, was not the subject of present work. More detailed works this subject is concerned, for example, in [SvdL00, Tem04] and in references therein.

A big change in the mean structural parameters of fused silica such as mean Si–O distance and mean Si–O–Si angle, or mean dihedral angle, should affects mean polarizability of the bound electrons. That causes permanent refractive index changes. On the other side, defects in the fused silica networks lead to the appearance of absorption bands in the optical spectrum of the fused silica. According to Lorentz theory of dispersion, the appearance of absorption levels will change the real part of refractive index in the vicinity of an absorption band. These changes could be calculated using Kramers-Kronig relations [LL84]

$$\varepsilon^{'}(\omega) - 1 = \frac{1}{\pi} P \int \frac{\varepsilon^{''}(x)}{x - \omega} dx \tag{2.19}$$

$$\varepsilon^{''}(\omega) = -\frac{1}{\pi} P \int \frac{\varepsilon^{'}(x) - 1}{x - \omega} dx, \tag{2.20}$$

where P denotes the Cauchy principal value. We see that the real and imaginary parts of such a function are not independent, so that the changes in one part cause the variation of the other.

2.5 Conclusions

We have outlined the main concepts describing the fused silica network. They include the ideal network structure characterized by its short-range order, as well as consideration of defects in such network. We have equally discussed here several factors affecting the optical properties of fused silica, in particular its refractive index. One can conclude that according to Lorentz-Lorenz formula the refractive index mainly depends on the density and electronic polarizability of atoms forming fused silica. Modifications in the fused silica network under femtosecond radiation affects both these factors. Additionally, these modifications could be measured using spectroscopy means: photoluminescence spectroscopy reflects the appearance of defect states and Raman spectroscopy shows macroscopic structural changes in fused silica network. Thus, data obtained in the spectroscopic experiments which reflect structural changes in the fused silica network should be treated with the aim of describing its refractive index changes.

Chapter 3

Interaction of femtosecond laser pulses with glass materials

The aim of this chapter is to present the mechanisms leading to permanent modifications induced by ultrashort irradiations. They are schematically illustrated on the timescales chart in Fig. 3.1. We first describe the main energy deposition mechanisms via the photoionization and formation of an electron-hole plasma. The presence of these carriers could strongly affect the propagation, especially of the ultrashort pulses. This is described in the subsequent section. The chapter ends with a review of the energy relaxation pathways and an analysis of their role to the material modification and optical properties changes.

3.1 Photoionization processes

It is known that the interaction between the material and visible and near infrared light takes places via the electronic subsystem. In dielectrics electrons are strongly coupled to the ions, resulting in a wide gap appearing between the valence and conduction bands. In fused silica the energy of this gap is equal to E_g=9 eV (see Fig. 2.4). Since the photon energy is small compared to the material band gap, no linear absorption takes place. This define the transparency of dielectrics in the considered spectral range. However, the use of focused femtosecond pulses allows to reach laser intensities sufficiently high for triggering the processes of nonlinear optical absorption (photoionization), leading to generation of free electrons in the conduction band.

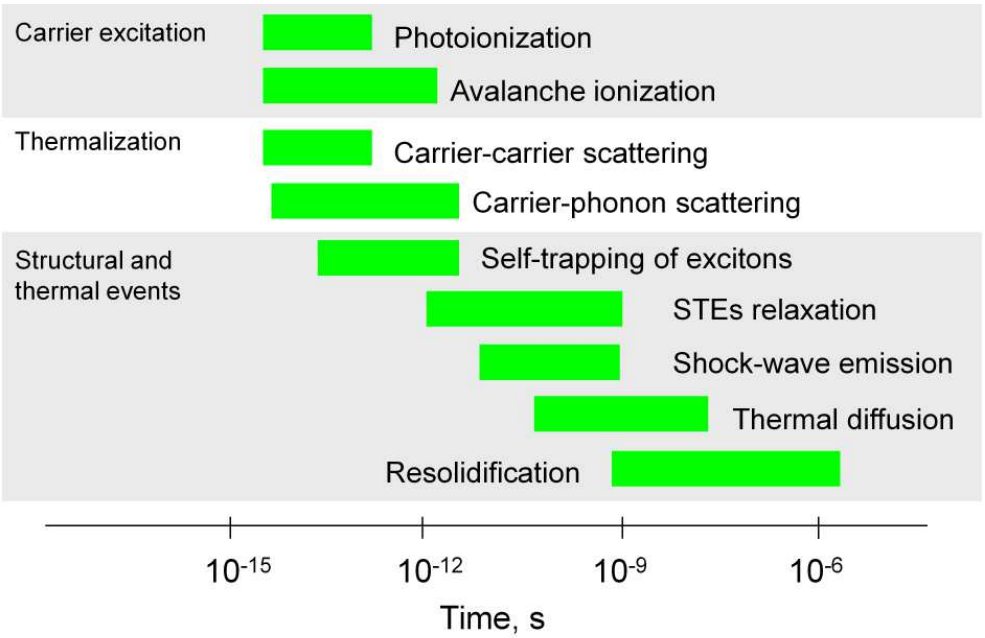

Figure 3.1: Timescales of the physical phenomena associated with the interaction of a femtosecond laser pulse with transparent materials according to [GM08].

3.1.1 Nonlinear ionization

The transition of the electron to the conduction band could be realized by the simultaneous absorption of several photons having a total energy that exceeds the energetic barrier (Fig. 3.2a) and allows sufficient kinetic energy to sustain the oscillation in the field (quiver energy). This effect is called *multiphoton ionization* (MPI) [NGM85]. Its probability is given by the following relation

$$w_{MPI} = \sigma_N I^N, \tag{3.1}$$

where N is the number of simultaneously absorbed photons, I is the laser intensity and σ_N is the corresponding crossection of N-photon absorption. For fused silica irradiated by 800 nm (1.55 eV) laser pulses, N is given by integer part of the ratio $E_g/\hbar\omega + 1$, which is equal to 6. For weak fields such absorption is hardly possible, because of the extremely small crossection of this process. However, the strong power dependence and the strong laser intensity available in the femtosecond laser pulses increase the probability of ionization sufficiently. Thus, the MPI is considered as the main mechanism of free carrier generation in the dielectric materials [TSZ+06].

Ionization in solids could also happen via intermediate states. These could be defect levels caused by impurities presented in the dielectrics or point defects (Fig. 3.2c). The probability of ionization will be described by the formulas similar to the 3.1 but with different power dependencies and corresponding ionization cross-sections determined by the reduction in the gap. In repetitive character of interaction of laser pulses with surface or bulk of the material, when intermediate states were generated in previous cycle of interaction, this leads to an *incubation* effect. In this case a significant reduction of threshold for multiple-shots experiments in comparison with single-shot experiments was observed because of the reduced cross-section of the ionization from intermediate states [RL+99].

Competitive to the MPI mechanism of free electron generation is the *tunneling ionization* [Kel58]. Under strong electric fields the disturbance of valence and conduction band is possible depicted in Fig. 3.2d, creating dynamic variation of the gap and leading to possibility of the electron to tunnel from the valence to conduction band.

The occurrence of a particular type of ionization is dependent on the material parameters such as the band gap E_g, the reduced optical mass of the carriers m, and is equally influenced by laser parameters: instantaneous intensity and frequency. The frontiers between the various regimes of ionization can be qualitatively described by the adiabatic (Keldysh) parameter γ equal to

$$\gamma = \frac{\omega}{e}\sqrt{\frac{cnm\varepsilon_0 E_g}{2I}} \tag{3.2}$$

where e is the elementary charge and c is speed of light. It could be represented as the ratio of the frequency of light to the characteristic frequency of tunneling, so it naturally defines the limits where different ionization regimes take place. For cases of high laser frequencies and low field, when $\gamma >> 1$, multiphoton ionization takes place. On the other hand for low frequencies and strong laser fields, when $\gamma << 1$, tunnel ionization is possible. For laser parameters such as λ=800 nm, τ=150 fs and the following material parameters $m = 0.6m_e$=5.8×10^{-28}g, n=1.45, the Keldysh parameter is equal to unity for an intensity of the laser pulse around 3.5×10^{13} W/cm^2. This corresponds to values, that can be easily achieved by focusing 100 nJ laser pulses with an objective of NA=0.3. This means that in such energetic regimes photoionization could be described neither by the multiphoton nor by tunneling ionization alone, but by a partial combination of the two. Thus, a more general frame has been proposed to account for such interplay [Kel65, Gru07].

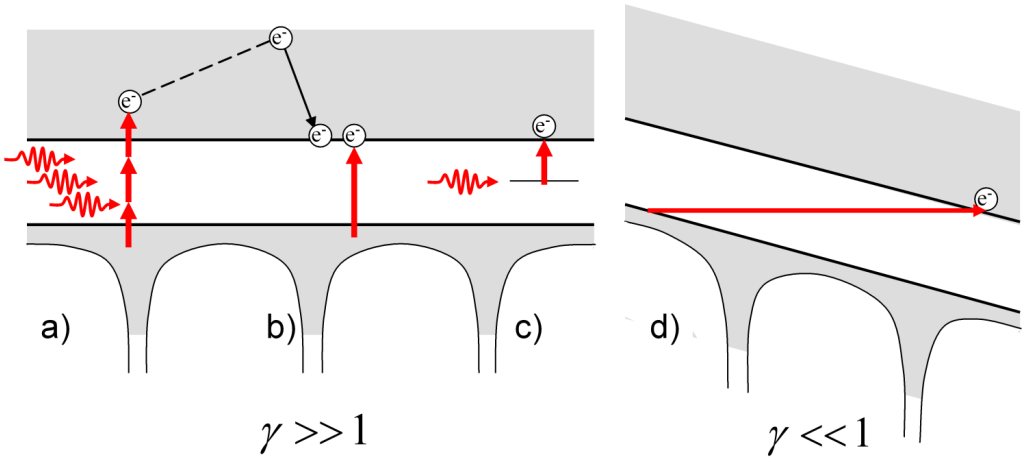

Figure 3.2: Ionization processes in the solids: a) multiphoton ionization, b) impact (avalanche) ionization, c) contribution of defect states, d) band structure perturbed by strong laser field leading to tunneling ionization.

3.1.2 Collisional ionization

Upon the interaction of ultrashort laser pulses with the free electrons produced by MPI and tunneling ionization represent an initial population in the CB. Their average kinetic energy continuously increases due to free-electron absorption mechanism, or *inverse bremsstrahlung*, upon their interaction with the field and scattering on ions. When the kinetic energy of free electrons exceeds a certain critical value $E > E_{cr} > E_g$ (Fig. 3.2b), then it eventually leads to knocking out of the bonded electrons after interaction with neutral atoms. This process is called *impact ionization*. In the CB instead of one energetic electron, two relatively cold ones are appearing. Since the probability of the impact ionization given by the formula

$$w_{imp}(t) = \sigma_{coll} I(t) n_e(t) \tag{3.3}$$

is proportional to the initial concentration of seed electrons $n_e(t)$, this process has an avalanche character and it could be developed quite fast if the time of interaction with the laser field is higher than the collisional time, $\tau_p >> \tau_{coll}$ (allowing a sufficient number of collisional events). Thus, avalanche ionization becomes important for sub-picosecond and longer pulses. However, for short femtosecond pulses the processes of nonlinear photoionization are dominant.

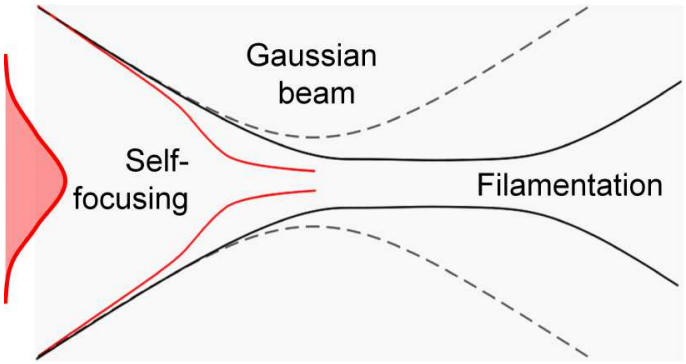

Figure 3.3: Schematic regimes of nonlinear propagation of focused Gaussian beams (dashed gray curve). Two regimes can be realized: self-focusing (red curve) due to nonlinear Kerr effect and filamentation propagation (black curve) due to the competition of the Kerr effect and diffraction divergence or plasma defocusing.

3.2 Nonlinear propagation of pulses

Various nonlinear effects resulting from the strong laser fields in the material and the additional free electrons appearing in the focal region are also contributing in determining the spatio-temporal propagation of the laser pulses. The high laser intensities reached in the femtosecond pulse can drive various nonlinear effects, making the case of propagation of femtosecond laser pulses to be particular, even in comparison with picoseconds one, since femtosecond laser pulses carry much higher peak intensity in pulses of the same energy.

The amplitude of the laser field is the crucial parameter defining the nonlinear properties of laser-matter interaction, since the response of amorphous media to the external field becomes dependent on it [Boy07] according to the following relation:

$$\mathbf{P} \approx \varepsilon_0(\chi^{(1)} + 3/4\chi^{(3)}|E|^2)\mathbf{E} \tag{3.4}$$

where $\chi^{(3)}$ is the nonlinear permittivity. Eq. 3.4 depicts the nonlinear Kerr effect, which determines in a first approximation the dependency of the refractive index of the medium on the intensity of laser field according to

$$n(I) = n_0 + n_2 I, \tag{3.5}$$

where $n_2 = 3\chi^{(3)}/4n_0^2\varepsilon_0 c$ is the nonlinear refractive index. For fused silica the n_2 was found to be $n_2 = 2.48 \times 10^{-16}\,\mathrm{cm}^2/W$ and for borosilicate crown (BK7) at $n_2 = 3 \times 10^{-16}\,\mathrm{cm}^2/W$.

As a result, the laser beam having an initial Gaussian spatial profile induces a transverse refractive index variation within the material with a larger refractive index at the center of the beam than at its periphery, acting as a positive lens. The beam can be self-trapped when the effect of the self-induced lens exactly balances the diffraction divergence of the laser beam. In this process a beam of light propagates with a constant diameter as illustrated in Fig. 3.3. This happens if the power of laser beam reaches the critical value [DR06]

$$P_{cr} = \frac{\lambda^2}{4\pi n_0 n_2}, \tag{3.6}$$

where λ is the wavelength of the laser field. For fused silica we estimate the critical power at P_{cr}=1.4 MW, that corresponds to pulse of 140 fs carrying the energy of about 200 nJ. If the beam power is greater than critical value $P > P_{cr}$ then self-focusing can occur.

At high intensities photoionization, taking place in the focal region induces additional nonlinear processes, complicating the effect of nonlinear propagation of the laser pulses. The nonlinear energy transport in the case of a single laser pulse in the irradiated sample can be evaluated using a pulse propagation code based on the nonlinear Schrödinger formalism in the slow varying envelope approximation [CSF+05, SCF+02, BBS+07], or solving the set of Maxwell's equation [HBT+07, PMB+11]. Except of laser and material parameters, an important role in energy deposition is determined by the focusing conditions. Taking into account numerical apertures (NA) of focusing objectives, it is natural to consider extreme cases of focusing: tight[1] and loose focusing defined by high and low values of NA. Here we give an outline of these studies.

3.2.1 Moderate to tight focusing

Considering moderate to tight focusing of laser pulses (NA∼0.5) the energy deposition occurs in the Rayleigh zone with a shift of the maximum electronic energy concentration towards the direction of the pulse arrival. This specific shape of the electron cloud is described by the interplay of several key phenomena during pulse propagation as self-focusing, phase modulation, defocusing on carrier plasmas as well by depletion of electrons in the focal plane. According to the scenario in [BBS+07] where the time-resolved exposure is investigated, the focused beam illuminates the geometrical focus

[1] Despite in the literature tight focusing is usually referenced by the use of objective with NA>0.9, in the text it means the values of NA∼0.5, which could also be called "moderate to tight focusing" or "rather tight focusing".

only in the first moments of irradiation. There, due to the emergence of a low density plasma but also due to amplification of self-focusing as the momentary intensity increases, a screening effect develops. The energy starts to be scattered away and agglomerates at later times in regions preceding the geometrical point of focusing. This equally leads to the free electrons concentration and laser field intensity saturation in the region of interaction. According to different estimation laser intensity reaches the values in the order of $10^{13}\,\mathrm{W/cm^2}$ [CSF+05, BBS+07, PMB+11] and electron concentration reaches the maximum values from $3{\times}10^{20}\,\mathrm{cm^{-3}}$ [CSF+05, BBS+07] up to critical values in the order of $10^{21}\,\mathrm{cm^{-3}}$ [PMB+11]. The critical value of electronic concentration $n_{cr} = \varepsilon\omega^2 n_e^2 \varepsilon_O m_e/e^2$ calculated according to the Drude model using Eq. 2.18 defines the conditions when efficient laser filed screening happens. We estimate the value of $n_{cr}{=}3.6{\times}10^{21}\,\mathrm{cm^{-3}}$ for 800 nm light.

3.2.2 Loose focusing

On the other hand, considering loose focusing (NA$\sim$0.1), one can achieve the regime when effects of light self-focusing due to Kerr effect is compensated by the free electrons creating the negative contribution to the refractive index and acting as negative lens, leading to light defocusing. Thus the region of plasma generation elongates towards the direction of pulse propagation forming so-called filaments. In such filaments laser intensities do not exceed values of $10^{13}\,\mathrm{W/cm^2}$ and electronic concentration are limited at $10^{20}\,\mathrm{cm^{-3}}$ by self-defocusing leading to a clamping process [CSF+05].

3.3 Modification of the fused silica network

The energy deposited in the electronic subsystem is then transferred to the lattice via collisions with phonons. The number of electrons and their energetic spectrum are the important parameters in relaxation processes. For femtosecond pulses the processes of energy absorption and redistribution to the phonons can be temporarily decoupled, since the main energy transfer takes place from the hot electrons after the pulse has stopped. The detailed kinetics of the electronic excitation/relaxation processes can be investigated by considering the electron energy distribution function [KRVS00, SI12] or using rate equations approach [BSR10, Ret04].

Eventually, structural changes occurs via 1) conventional heat deposition and thermo-elastic relaxation processes resulting in a phase transformation of the dielectric material and 2) electronically induced structural transitions

(e.g. defects), as schematically indicated in Fig. 3.1. This involves global reorganization of the fused silica network that can be described in terms of changes of the mean angle and distances between Si and O atoms, changes in ring statistic of fused silica network and point defects formation.

Let us first consider a gentle regime of interaction with the glass such as the one realized under loose focusing condition. This regime appears not to be able to induce temperature increase enough to melting or softening of the glass network. Indeed, if we will take into account an average kinetic energy of electrons in the order of E_k ~13 eV [BBS+07], the full energy of the electrons will be E_e=E_k+E_g=22 eV=3.5×10^{-18} J. Let us calculate the temperature elevation considering that all electronic energy transfers to the lattice heat. In this case specific energy E=$n_e E_e$ transfers to the glass E=$c_{fs}\rho\Delta T$, where c_{fs} is the specific heat capacity of fused silica, c_{fs}=1.052 J/g·K and ρ is the density of fused silica glass equal to 2.2 g/cm^3. Thus the order of temperature elevation ΔT could be estimated using the following ratio

$$\Delta T = \frac{n_e E_e}{c_{fs}\rho} \sim 150K \tag{3.7}$$

One should note that according to this relation an overestimated value of the temperature increase is obtained. Some part of the energy goes to the luminescence or the stable defects generation, so the local temperature increase will be lower.

This may be considered as a limitation of the loose focusing regime. On the contrary, this condition could be surpassed for tighter regimes. If the electron concentration exceed the value of 10^{21} cm^{-3}, then the efficient melting could take place.

Thus, to the possible mechanisms of the femtosecond laser induced network reorganization different processes were proposed: rapid temperature elevation and rapid cooling [CTRK01], defect formation after STEs relaxation [HM98, ZRG+06] via free electrons, and densification by the pressure wave generated as a result of the rapid relaxation of stress in response to the volume changes in the exposed region [GM97, STS+11]. Overall network reorganization could be an effect of only one process as well as contribution of all three factors together. Hereafter we will discuss the roles of these mechanisms in the network reorganization and refractive index changes.

3.3.1 Viscoelastic relaxation and glass transition

In the hypothesis that the local temperature exceeds the value when softening happens, the isotropic refractive index changes observed have been attributed to localized melting and rapid resolidification of the glass. This process is

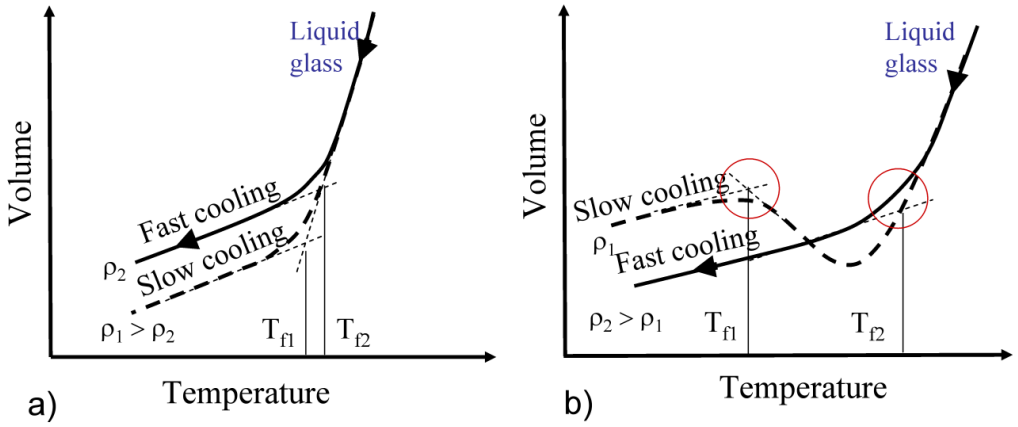

Figure 3.4: Schematic volume-temperature diagrams for a) common glasses and b) fused silica under various cooling rates. On the abscissa T_{fi}, i=1,2 means glassification temperature for slow (cooling rate of seconds)and fast cooling (cooling rate of milliseconds and shorter), defining fictive temperature structure of glasses and consequent densities ρ_i.

illustrated on the following volume-temperature diagram shown in Fig. 3.4. In common glasses a rise and fall of temperature determine lower densities as indicated in Fig. 3.4a. However in fused silica due to an anomalous behavior at the region 1000–1500 °C, the density and refractive index of the material is higher if the glass is quenched from a higher temperature. Thus, if the material in the focal volume melts and then quenches, we expect a higher refractive index and a higher density in the irradiated region for fused silica compared to the non-irradiated region. The temperature range, where glassification happens define the fictive temperature of glass. According to the experimental results, with the increase of fictive temperature of type I/III silicas both its density and refractive indices are augmented [Bru70].

Generally, the model predicts the behavior of the density and the refractive index changes for many glasses and especially for fused silica. The crucial point of this model is that the new phase is achieved by cooling down from the liquid glass phase. During cooling the glassy network adjusts its configuration to the corresponding equilibrium one, unless the cooling is going very fast. In this case, an "internal" time to adjust network configuration defined by the glass viscosity becomes higher than the "external" time controlled by the cooling rate. The rearrangements of the network can not follow the cooling process and the freezing of the structure happens. The time needed for a small deviation of the structure to come to the equilibrium form is defined

by viscoelastic relaxation time given by

$$\tau_r = \eta/G, \tag{3.8}$$

where η is viscosity of silica glass, and G is bulk modulus. At temperatures close to the softening point at the range of 1500–1700 K, η should be of the order of 10^6–10^5 Pa·s [GRD08] and G around 30 GPa, so the time needed to silica to reach its equilibrium form can be estimated higher than 10 μs. Practically, this equilibrium will not be reached, because after few picoseconds cooling takes place and at times $\sim$1 μs the area of interaction are already cold. Only if the interaction between the heat source and matter takes a longer time, the standard fictive temperature model is valid, as in the cases of thermal [GG83b] heating or continuous CO_2 laser laser irradiation [MVC+10].

The maximum rate of densification predicted by the fictive temperature model is only 0.2 % [Bru70, She04] achieved at the T_f=1550 °C, leading to maximal refractive index changes Δn =5×10^{-4} [Bru70]. That contradicts with higher refractive index changes achieved in multipulse regime of irradiation, up to 10^{-2}, reported in the literaure [DMSH96, GM97, SB02, WNCT02].

Finally, the fictive temperature model is defined under ambient pressure, despite it was reported that pressures up to several GPa could be generated in the focal region [JRG+03]. That eventually leads to ambiguity in the determination of fused silica structures using scales of fictive temperatures.

3.3.2 Pressure compaction

Mechanical densification arises from volume changes happening after fast energy deposition into the focal zone. After a fast temperature increase of the fused silica network, the heated material should exhibit thermal expansion. Since this process lasts only several picoseconds, it could be described as isochoric which leads to pressure increase in the heated zone. The evaluation of pressure elevation based on the estimated temperature changes and thermal expansion coefficient of fused silica is given by

$$\Delta p = \alpha_T Y \Delta T, \tag{3.9}$$

where α is the linear thermal expansion coefficient, $\alpha_T = 0.59\times10^{-6}$, Y is the Young modulus of fused silica at the room temperature, Y=73.3 GPa. For a temperature elevation up to the softening point (ΔT$\sim$1500 °C) this formula give a pressure increase of Δp=65 MPa. This estimation is not enough to create strong permanent refractive index changes, since it has been reported that shock pressure which induces irreversible damage of fused silica taken

at room temperature must be higher than several GPa [ORS+99]. However, if the fused silica state is near or above the transition temperature, the value of the applied pressure leading to permanent modifications is of the order of several hundreds of MPa. This could be achieved during interactions with the light.

More extreme regimes could be observed at tight focusing, when microexploisons were reported [GM97, JRG+03, GJN+06, MBR+09]. Energy densities at that regions could reach values which are sufficient to evaporate the silica. Considering generated silica phase as a mixture of gases of atomic oxygen and silicon, one could estimate generated pressure using simple thermodynamic ratio

$$p = 3/2 n_i k_B T \tag{3.10}$$

where n is the concentration of atoms in fused silica, n_i=2.2×10^{22} cm^{-3}, k_B is the Boltzmann constant, k_B=1.38×10^{-23} J/K. Thus at the evaporation temperature, which is estimated to be of 2500 °C, the Eq. 3.10 gives the minimum pressure value of 1.1 GPa. That could be enough to trigger a shock wave, leaving hollow void zone in the region of the focus due to rarefaction and causing densification in the vicinity of the focus. Lower density regions can also appear at lower temperatures following mechanical rarefaction [MBR+09].

3.3.3 Defect-assisted densification

The effect of defects formation on densification was also described in the literature. Summarizing data on particle bombardment, electron and neutron beams, γ-rays and UV irradiation, several ideas of densification by defects were proposed [Pri72, DD96, SO97]. According to Primak [Pri72], defect-assisted densification could be considered as a relaxation of stress induced in their vicinity that leads to the compaction. Douillard and Duraud [DD96] proposed a two step process. In a first step, the generation and accumulation of stable defects in fused silica network takes place that consequently triggers a network reorganization. This appears after the defect concentration exceeded some critical concentration. STE relaxation is considered as the origin of the stable defects pairs in silica (E' and NBOHCs) and the critical concentration of defect centers was estimated on the order of 10^{18} cm^{-3} [DD96]. Network reorganization process could be accompanied by the formation of smaller rings as was suggested by Friebele and Higby [FH88]. Molecular dynamics performed on silica samples rich in defects (generated by UV-irradiation or some other way) [ZLS04, ZAF+06] confirm the tendency of density increase, interbonding angles decrease and changes in ring statistics.

Lattice transformation has in this case a local character. In the first

approximation the induced densification will be a function of the number of the breaking bonds, which directly depends on the radiation dose. The major consequence of this is the accumulation of damage or transformation effects. Since after material modification the number of broken bonds is much smaller than the number of total bondings in the specific volume, by following pulses it is more probable to create defect pairs leading to local transformation in new place of the same volume. Such accumulation of the locally modifying regions then leads to continuous changes in density or refractive index as a function of accumulated energetic dose.

3.4 Conclusions

We have identified the main ionization mechanisms feeding the transient electronic gas. Together with the nonlinear propagation of ultrashort pulses, these processes define the spatio-temporal energy deposition and its consequent relaxation in laser affected zone. We showed that depending on the energetic and focusing conditions, strong (determined by self-focusing) and soft (filamentation) interactions regimes can be achieved. Finally, we described main concepts related to the material changes resulting after energy relaxation. Its relaxation paths are determined by different interaction conditions achieved in these two regimes.

Chapter 4

Experimental setup for laser processing

The experimental setup consists of an irradiation system (ultrafast laser) with spatio-temporal shaping capacities and a real-time detection system made of optical phase contrast microscope. The schematic sketch of the setup is presented in Fig. 4.1. The aim of the following section is to give only a brief overview of the working principles of its elements, whereas a detailed description of its abilities could be founded elsewhere [Coh, San05, MB07, Mau10]. In addition, photoluminescence and Raman post-mortem analysis will be presented in the next chapters.

4.1 Generation of femtosecond laser pulses

Ultrashort infrared light pulses were produced by the laser system schematically represented in Fig. 4.2. It includes a Vitesse oscillator (Coherent) and a RegA 9000 amplifier (Coherent) and produce pulses with a spectrum of 13 nm FWHM bandwidth centered around 800 nm. Both are pumped by a continuous wave laser (Verdi) which consists of two power diodes (808 nm) pumping a Nd:YVO4 crystal with an intra-cavity frequency doubling LBO crystal to match the Ti:Sapphire absorption spectrum. The system delivers τ_p=130 fs (FWHM) pulses with an energy approaching 6 μJ, and the output beam has a $1/e^2$ diameter of about 5 mm. This system has a high repetition rate (RR) which could be varied between 10 and 250 kHz, that is advantageous in multiple pulse bulk photoinscription of photonic devices.

A mechanical Uniblitz LS6 shutter was employed to pass the laser pulses to the region of modification. It is characterized by the time of the opening t_o=700 μs, that allows to control the number of pulses acting in the

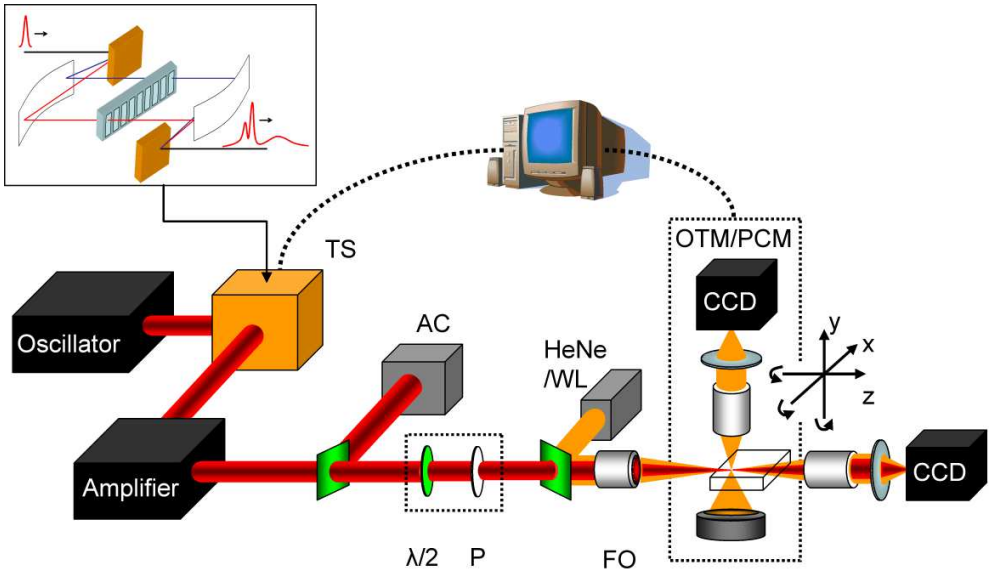

Figure 4.1: Illustration of the experimental setup. TS: temporal shaper illustrated in the top inset. FO: focusing objective. OTM-PCM: Optical transmission and phase contrast microscopy for investigating the sample modification. AC: Autocorrelator or other pulse characterization apparatus, HeNe-WL: Helium Neon laser source (emitting at 633 nm) and white light source for waveguide characterization, $\lambda/2$+P: half-lambda plate and polarizer allowing variable attenuation of the laser power. The setup permits the temporal pulse design and subsequent optimization of laser induced bulk modification.

interaction with the precision up to N_{min}=140 pulses at 100 kHz and up to N_{min}=14 pulses at 10 kHz. These are defined by the number of the pulses passing through the shutter during the opening and closing cycle. The rather long time of the opening window limits the application of shutter when attempting to study the damage produced by a low number of pulses. Only material changes produced by a number of pulses sufficiently exceeding N_{min} could be investigated since the effect on the material changes of the pulses during the opening-closing cycle is smaller than the effect of irradiation during a long exposure. For cases when high precision of the acting pulses is needed, pulses could be extracted manually out of amplifier or another low repetition laser system was employed.

As indicated, this system is equipped with a temporal shaping apparatus. This allows to compensate group velocity dispersion introduced by the optical elements on the optical path or to arbitrary change the time envelope of the

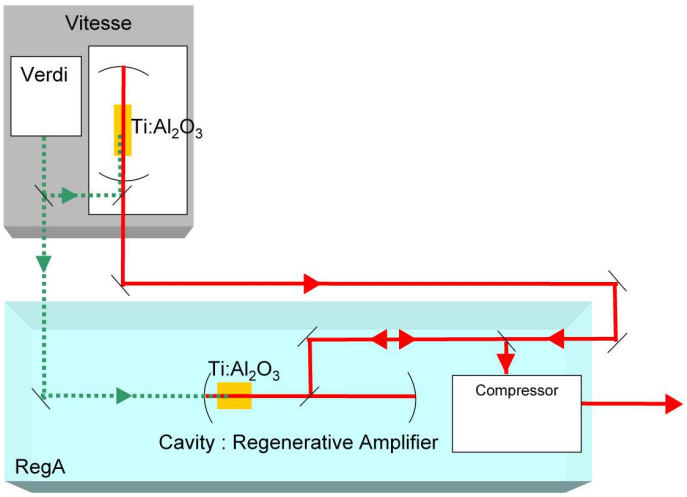

Figure 4.2: Schematic representation of a regeneratively amplified femtosecond laser system from Coherent. The green arrow represents the pump beam and the red arrow the seed and amplified femtosecond pulses.

produced pulses. Using this setup the effect of the form of the pulse on the resulting glass modification could be studied. The temporal shaping apparatus, depicted on the inset in Fig. 4.1 was constructed on the base of a zero dispersion stretcher, where a computer programmable liquid crystal modulator was inserted in its Fourier plane. This allow phase filtering of the spectral components, resulting in the change of the form of the output pulse. Detailed description of the employed pulse shaping technique is not the subject of the present work and could be found elsewhere [Mau10], as well as general pulse shaping methods [Wei00, SBWH10].

The setup allows the variation of the energy and polarization of the laser pulses. Variable attenuation of the laser pulse energy was performed with the help of a rotating half-lambda plate and polarizer. Optionally, another rotating half-lambda or quarter-lambda plates could be added on the optical path to rotate polarization of the incident laser beam or to transform it to the circular one.

Characterization of the produced pulses was performed by a portable autocorrelator PulseCheck from APE, home-made crosscorrelator and Swamp Optics GRENOUILLE devices. Pulse durations were measured in diverse points in the laser path even after the focusing objective to guarantee the shortest pulse duration. The spectra of the femtosecond pulses were recorded by a portable spectrometer from OceanOptics.

4.2 Focusing of laser pulses

Several long working distance objectives were used to focus laser pulses inside the transparent materials. Among them we used a 50× microscope objective OB1 (Nikon L Plan, working distance 17 mm, nominal numerical aperture NA=0.45), a 20× microscope objective OB2 (Mitutoyo MPlan, working distance 20 mm, nominal numerical aperture NA=0.42) and a 5× microscope objective OB3 (Mitutoyo MPlan, working distance 30.5 mm, nominal numerical aperture NA=0.14). For practical use, a main importance has the geometrical size of the focusing region, since most of the energy leading to material transformation is deposited in a limited region around the focus. The NA of the objective is the main factor defining this area; however, it also depend on the intensity profile of the radiation filling the entrance pupil of the objectives. To this extent two major cases should be considered: illumination with a plane wave and with the Gaussian beams. The delivery are an Airy and a Gaussian profiles in the focus respectively. The intermediate cases arise when beam diameter is higher than the entrance pupil, a process called truncation. In this case, only the central part of the beam filling the objective is focused resulting in a hybrid intensity profiles in the focal plane.

Typically, nominal numerical apertures are calculated for the plane wave uniformly illuminating the pupil. This gives underestimated values of the beam diameter in the focal region for real beams. For this reason the values of NA were recalculated from the actual experimental focusing conditions. Hereafter, effective numerical apertures NA_{eff} of objectives will be used, that should give the same spot diameter under illumination with a plane wave.

Let us discuss some general equations expressing the diameter of the spot in the focal plane

$$d = K\frac{\lambda f}{D} = K\frac{\lambda\sqrt{1-NA^2}}{2NA}. \tag{4.1}$$

Here K is a constant depending on the pupil illumination, f is the focal length of the objective and D – its output pupil diameter.

For uniform pupil illumination, the image spot takes the form of an Airy disk, where intensity drops to the $1/\mathrm{e}^2$ level at the diameter

$$d_{1/e^2(plane)} = 1.64\frac{\lambda\sqrt{1-NA^2}}{2NA}. \tag{4.2}$$

If the pupil illumination is made by a Gaussian profile, the result is also a Gaussian profile. The diameter of this will be given by the formula

$$d_{1/e^2(gauss)} = \frac{4\lambda f}{\pi D_0}. \tag{4.3}$$

where D_0 is the input diameter of the Gaussian beam measured at the $1/e^2$ level.

When the pupil illumination is between these two cases, it is helpful to introduce the truncation ratio $T = D_0/D$ depending on which, the intensity profile in the focus approaches either an Airy disk or a Gaussian profile. Calculation of the beam diameters could be made then using formula presented in the work of Urey [Ure04]. The effect of the changes of the real focal spot diameter could be determined by defining effective numerical aperture NA_{eff}, giving the same diameter at the level $1/e^2$ of an Airy disc.

To preserve sufficient pulse energy, we employed most of the time a rather low truncation ratio. For $T = 1$ (case of the objective OB1), the fractional power loss is only 13.5 %, beam diameter in the focus increases if compared with the diffraction-limited spot. In this case $K_{1/e^2} = 1.83$, that corresponds to a situation equivalent to the use of NA_{eff}=NA×1.64/1.83 = 0.40, lower than the nominal NA=0.45. $T = 0.5$ (case of the objective OB2) approximates the situation of non-truncated gaussian beam; however, the diameter of the input beam is lower than the diameter of the pupil. The objective is not filled effectively and the spot diameter increses since $K_{1/e^2} = 2.51$, leading to the lowering of the nominal NA=0.42 to NA_{eff}=0.3. By analogy one obtain NA_{eff}=0.09 for OB3.

The expressions for the focusing area displayed above are valid in air; however, during focusing into the bulk several additional effects arise. While the beam waist in the focus keeps the same, the confocal parameter is scaled by n where n is the refractive index. Another very important effect is spherical aberration, occurring from the non-ideal focusing of marginal (or off-axis) rays. Differences in the geometrical paths obtained between marginal and axial rays incident on the flat interface between air and glass lead to the elongation of the focal region and to the increase of the beam waist diameter with additional artifacts around the axis.

The effect of the blur is higher for high NA objectives and for higher focusing depths of the pulses. For that reason the use of the high-NA objectives (NA_{eff}=0.4) was limited to the depth of 200 μm, where no significant changes in the focal zone were observed so spherical aberration could be neglected [HTS+05]. To work deeper in the bulk, low-NA objective should be applied or spherical aberration compensated as a function of the working depth [MMBH+08].

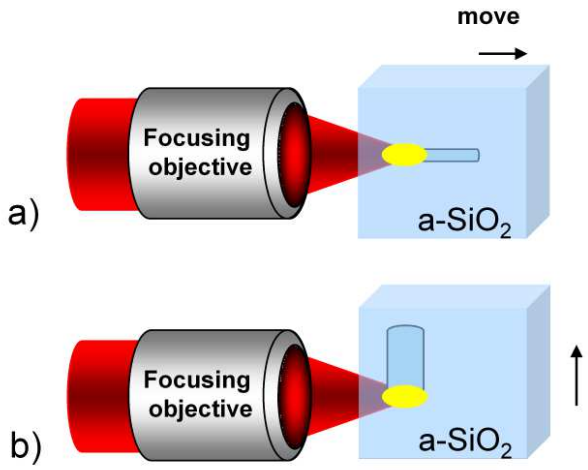

Figure 4.3: Geometries of writing used when the laser beam is fixed and sample is moving. a) Longitudinal writing, with movement parallel to the laser axis, keeps the symmetry of the beam during writing. b) Transverse writing, perpendicular to the laser axis, leads to nonsymmetric traces produced during writing.

4.3 Geometry of bulk photoinscription

As a target material polished fused silica parallelepipedic samples (10×20×3 mm) were employed, mounted on a XYZ motion controller that allows translation parallel or perpendicular to the laser propagation axis. This makes possible 3D imprinting of structures in the bulk. Movement of the sample parallel (longitudinal writing) or perpendicular (transverse writing) could be employed for writing the optical devices. In case of longitudinal writing, the motivation is related to the ability of replication of the symmetry of the laser beam during writing with respect to the optical axis. The produced traces have a small diameter even using low NAs. A schematic description of the geometry is given in Fig. 4.3a. Transverse writing delivers elliptical traces with a size given approximately by the confocal parameter of the focused beam (Fig. 4.3b), thus, this method requires the use of tight focusing or beam shaping techniques for producing traces with cylindrical symmetry. For this reason a longitudinal writing configuration was used in this work unless otherwise mentioned in the text.

In addition to dynamic studies, when sample is translated, static damage can be produced, when sample does not move. The number of pulses acting on the material during writing is the essential parameter affecting the

material changes in both situations. It is controlled by the time of exposure of the area. In static conditions this is performed with the shutter and the exposure duration is simply defined by its opening time.

A different picture takes place during dynamic writing. In this case, since after the arrival of each pulse the focusing point is moved away, only a certain amount of pulses interacts with each single point. For longitudinal writing, the effective number of interacting pulses will depend on the velocity of sample translation and size of the irradiated zone,

$$N_{eff} = RR\frac{L}{nv}, \tag{4.4}$$

where RR is the repetition rate of laser, n is the refractive index of sample, v is velocity of the translation stage movement and L is the length of interaction, which was taken as the size of the visible plasma luminescence in the direction of the sample movement.

In both, static and dynamic, irradiation regimes of modifications it is assumed that the material is completely relaxed before the new pulse arrival. If this is not a case, then heat accumulation effects is possible. In the present study no major changes in the material modification were observed in fused silica for repetition rates up to 200 kHz. This is in agreement with previous studies of different groups reporting that heat accumulation effect play an important role at MHz regime of irradiation [EZN+08]. These are defined by the characteristic time of heat diffusion from the irradiation zone. Thus we can roughly estimate the characteristic time of the focal zone cooling, being equal to $\sim$1 μs. It is nevertheless to be noted that even if the cooling occurs faster, a mechanical relaxation (stress release) is slower and takes place on a longer time.

4.4 In situ observation of permanent modifications

The produced changes in the refractive index were monitored by an Olympus BX41 optical microscope installed directly on the experimental table. 2D optical transmission microscopy (OTM) or positive phase contrast microscopy (PCM) pictures could be directly observed *in situ*. OTM mode indicates spatially resolved regions of absorption, and PCM allows to estimate produced modifications in terms of phase retardation qualitatively. The PCM technique transforms the phase information to the intensity variation and provides a 2D map of refractive index changes where positive and negative RIC are visible as black and white zones respectively on a gray background

(positive PCM). A Sony CCD camera XCLU1000 mounted on the microscope enables the image acquisition with a CCD array of 1600×1200 pixels with pixel size of 4.4 μm × 4.4 μm. Cross-polarization/birefringence microscopy was performed using Carl Zeiss Axio Imager microscope.

For sufficiently long traces, the positive refractive index changes allow light guiding, with characteristics that could be estimated from near or far field measurements of the propagating modes. For this case light from the HeNe laser source with a wavelength of 633 nm, attenuated Ti:sapphire laser light with a wavelength of 800 nm or light produced by white light source could be injected into the waveguides with the help of the focusing optics. Far field or near field was recorded using the Sony CCD camera either directly or with the help of a magnifying imaging microscope constructed at the output of the waveguide.

The refractive index profile of an embedded waveguide can be reconstructed by capturing the near field intensity distribution of the fundamental mode and solving the inverse Helmholtz problem [MB83, MC96]. The other technique is based on the estimation of the numerical aperture of the emitted output light by the relation NA=$\sqrt{2n\Delta n}$. Despite the fact that these procedures do not give exact refractive index distributions we employed them for qualitative estimation.

Processing of glasses is often accompanied by visible luminescence in the region of the interactions or emission of secondary radiation. This was equally investigated in the visible, near infrared and ultraviolet optical regions by recording the plasma luminescence images with the CCD and measuring the spectra of the emitted radiation using a portable Ocean Optics USB2000 spectrometer. The signal was collected by the optical fiber using a matching lens setup to obtain a good filling.

4.5 Conclusion

A processing setup was presented that include irradiation systems with pulse control characteristics and *in-situ/ex-situ* observation means.

Chapter 5

Femtosecond laser processing of bulk fused silica

5.1 Type I and type II regimes of interaction

As indicated before, the optical properties of a modified glass depend on the regime of laser interaction and, particularly, fused silica shows some peculiar properties upon ultrafast light exposure as a function of the irradiation conditions. We firstly explore the effects of laser multipulse irradiation in static and dynamic regimes that allow the photoinscription of particular optical functions. Fig. 5.1, represents a summary of irradiation regimes produced using focused 150 fs laser pulses by the objective OB1. Multishot conditions and the velocity of translation were chosen in such a way that static and dynamic traces were written with the equal effective number of pulses.

At low energy densities, with powers below or near the self-focusing threshold, isotropic positive refractive index changes are induced. These are usually denoted as type I and appears black in the PCM picture as indicated in Fig. 5.1. The threshold of visible modification was measured at pulse energy E_{th}=60 nJ for NA_{eff}=0.3 objective and E_{th}=40 nJ for NA_{eff}=0.4 objective; however, it is worth to note that few millions, $N \sim 10^6$, of pulses should interact with the glass to observe these modifications at lowest energies, making the above values a multipulse thresholds. In more energetic regimes near the self-focusing threshold (estimated to 200 nJ for the given conditions), as observed in the static traces, a highly scattering region of negative index change (visible as white color in Fig. 5.1) appears, resembling catastrophic optical damage. It accompanies positive index changes bearing a conical form with the apex in the direction of light propagation. Upon longitudinal scan this regime, denoted type II, can be further divided in two

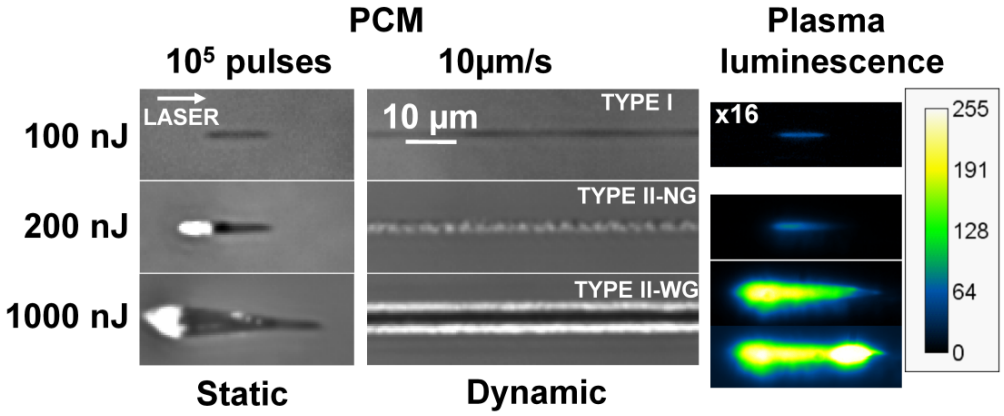

Figure 5.1: The effect of the irradiation dose as seen in PCM pictures of multipulse (N_{eff} $\sim 10^5$) traces in different incident laser power regimes at 100 kHz repetition rate. Moderately tight focusing conditions were used (OB1, NA_{eff}=0.42). Static and dynamic (scanned) regimes are presented. On the right, corresponding plasma images observed during photoinscription with increasing input power are depicted.

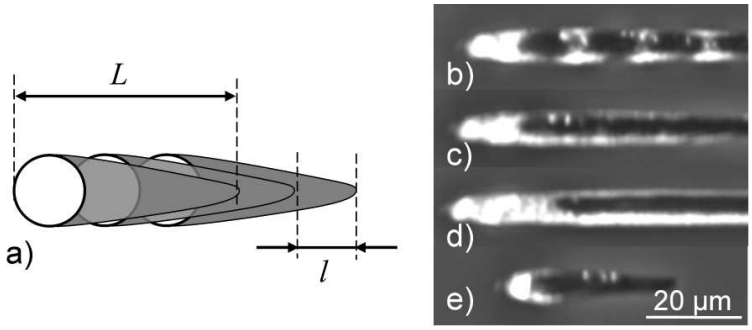

Figure 5.2: Left: a) Schematic mechanism of type II-WG guiding trace writing by the erasure of previous damage. Right: traces produced by focusing of 1.5 μJ 150 fs pulses at 100 kHz with the objective OB2 having NA_{eff}=0.3. Longitudinal traces written by the step-wise translation of the static trace of b) N=20000 pulses with the inter-step translation distance $l = 15\,\mu m$ and c) N=10000 pulses with the inter-step translation distance $l = 7.5\,\mu m$ giving N_{eff}=40000. d) Continuous longitudinal trace written by translation with v=50μm/s giving N_{eff}=40000. e) Static trace produced by N=40000 pulses.

subranges. At moderate fluences, the resulting longitudinal traces show a quasi complete negative refractive index change and do not support guiding. The corresponding traces will be called type II-NG. At high input powers and low scan velocities the central positive index change reappears into the longitudinal traces, leading to structures that support guiding (type II-WG).

5.1.1 Erasure effects in longitudinal traces

The appearance of a guiding core is defined by the chosen geometry of writing and can be explained by an erasure effect. To approach this we make appeal to the specific form of static traces (see Fig. 5.1), that can be put in a dynamic perspective. Since during writing each new pulse arrives before the location of the already induced permanent modification, it could rewrite the damage produced before. This is illustrated on the Fig. 5.2 by a demonstration with static traces produced by high enough number of pulses. In this case positive (black part) and negative (white part) refractive index changes region are already well defined. By the step-wise translation of such static traces towards the laser source by a distance l it could be observed (Fig. 5.2a) that now, the black part of positive index is located on that zone where the white low index part was located before. By acting with subsequent pulses, the white region can be rewritten by the black one. This effect occurs therefore also for establishing a type II-WG traces provided that the energy is sufficiently high and the "erasing strength" of the black region is equally high. This is equally an indication that the transition involves a soft material phase that facilitate erasing and reorganization.

On the Figures 5.2b,c longitudinal traces written by translating the static trace in a step-wise manner is demonstrated. Pulses having 1.5 μJ and 150 fs at 100 kHz were focused by the objective OB1 (NA_{eff}=0.3). The effective number of pulses producing such longitudinal traces can be calculated by the relation $N_{eff}=N \times L/l$, where N is the number of pulses producing the static trace and L was taken as the length of the static trace. In a continuous movement of the translation stage this formula is equivalent to the Eq. 4.4. Taking into account L=30 μm, the effective number of shots is the same everywhere in the traces and equal to N_{eff}=40000. These traces can be compared with the longitudinal traces written with the same number of effective pulses by a continuous translation written at RR=100kHz and v=50 μm/s, indicated in Fig. 5.2d. One can see indeed that the erasure was performed. Moreover, with smaller translational distance a smoother damage can be produced, comparable with continuous translation. The static trace produced by the N=40000 traces is shown on the Fig. 5.2e.

5.1.2 Focusing effects

The focusing strength has a paramount importance in determining the interaction regime, low NA favoring the type I regime traces while high NA leading with increased possibility of type II traces.

The influence of the energy density on the isotropic refractive index writing (type I regime) was confirmed by focusing the laser pulses using objectives with different NAs. With the decrease of NA, traces elongate and become wider, leading to a decrease of energy density. At the same time decreasing the value of effective NA, systematic increase of energetic threshold of type I/II transition was observed. This was analyzed on the static traces produced by N$\sim 10^5$ 130 fs pulses. For NA_{eff}=0.4 the transition threshold value is 0.15 μJ, while it increases up to 1 μJ for NA_{eff}=0.3 and to 5 μJ for NA_{eff}=0.1.

5.1.3 Effect of the pulse duration on the type of modifications

Pulse duration has also an important effect on the produced damage. Various nonlinearities switching on for ultrashort pulses could significantly change the energy density distribution in the focal zone as predicted by the numerical simulation [BBS+07]. Plasma defocusing effects and subsequent intensity clamping affect the energetic threshold of type I/II transition as a function of pulse duration. For OB2 with NA_{eff}=0.3 this dependency is illustrated in Fig. 5.3. A drastic drop of this threshold happens at pulse durations of approximately 150 fs. This appears unusual at the first sight, since a significant energetic drop occurs for changes in pulse duration less then 5 fs. However, one should take into account that the total damage is produced by N$\sim 10^5$ effective number of pulses. So small differences in the energy deposition arising after each pulse could force the development of the damage irreversibly according to one of the two scenarios, resulting either in the appearance of smooth modification or leading to the catastrophic damage.

The longer the pulse is, as carriers are produced later in the pulse, the light defocusing goes down and the energy is more efficiently concentrated, lowering thus type I/II transition threshold. This adds upon a carrier production mechanism that relies more and more on collisional ionization. For pulses longer than few ps, the photoionization cross-section goes down and the modification threshold increases again. However, the modification appears as a catastrophic damage.

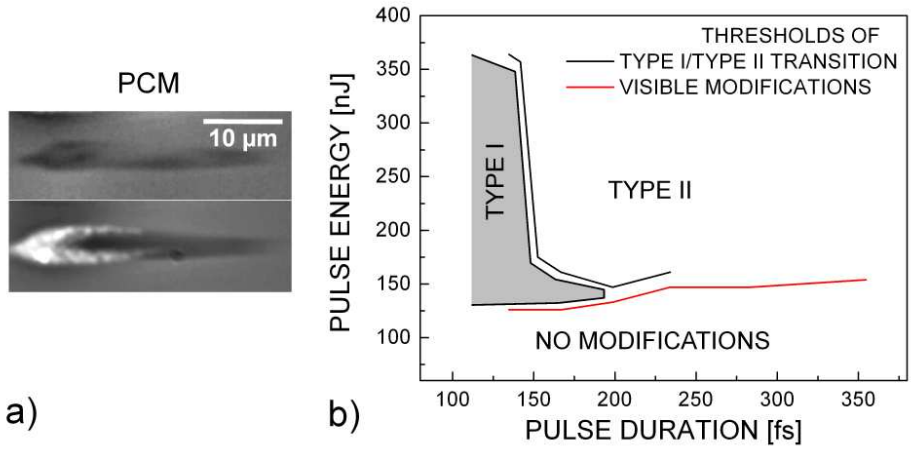

Figure 5.3: a) Static traces of N=50000 1 μJ focused by OB2 objective with NA_{eff}=0.3 for pulse durations of 140 (type I, top) and 150 fs (type II, bottom) b) Dependence of the produced modification threshold as a function of pulse duration for moderately focused laser pulses. Writing window for type I positive smooth refractive index changes (gray filling) is situated between energetic thresholds of visible modification (red line) and type I/II transition (black line) produced by N=50000 pulses in static conditions.

5.2 Form birefringence in type II regime

The present understanding of the material structure corresponding to type II negative refractive index region is based on electron beam scattering, Auger spectroscopy [SKQH03], chemical etching [BSR+06], and thermal conductivity coefficient measurement [BBS+08]. According to these data birefringent regions are composed from layers of different material densities forming regular periodic patterns. The lower density regions could be even hollow. The spacing between layers can vary depending on the writing conditions, but it is important that the minimal value is proportional to the wavelength of the writing laser λ and reaches values on the order of $\Lambda \sim \lambda/2n$, where n is the refractive index of the glass. This periodical layers are denoted as nanogratings, which appears to be the self-organizing structures. As a determinant characteristic, it was noted that nanogratings formation is strongly dependent on the laser field since their period is proportional to the wavelength of the writing beam and the orientation of their planes is perpendicular to the writing polarization. Typical examples are given in Fig. 5.4d,e, where typical cross-sections of type II-WG traces are displayed. No nanogratings,

but voxels are generating when the circular polarization of the writing beam are used (Fig. 5.4f).

However, the mechanism of nanogratings formation and arranging is still unclear. At the moment two models are proposed to explain the observed appearance. In the first one interference between the incident light field and the electric field of the bulk electron plasma wave was proposed, resulting in the periodic modulation of the electron plasma concentration and subsequent structural changes in glass following the electron density pattern [SKQH03]. This requires high electronic densities and temperatures. On the other hand, according to the alternative transient nanoplasmonics model [BSR+06], nanogratings are formed from nanoplasma regions generated due to the inhomogeneous character of the dielectric breakdown. Local field enhancement leads to elongation of nanoplasmas perpendicularly to the polarization of the incident field. The latters could self-arrange according to mode propagation in metal-like patterns following the memory-effect in pulse-by-pulse processing of the glass.

The appearance of such modulated patterns of refractive index results in form birefringence. A model description is presented in Fig. 5.4c. According the classical view [BW05], the region of birefringence could be imagined as a negative uniaxial crystal with its ordinary and extraordinary refractive indices. The polarization of the ordinary wave has a direction perpendicular to its optical axis, i.e. parallel to the nanogratings orientation. The extraordinary wave has the polarization oriented perpendicular to the nanoplanes. Refractive indices for different polarizations are then given by the following formulas:

$$n_{||}^2 = f_1 n_1^2 + f_2 n_2^2, \tag{5.1}$$

$$n_{\perp}^2 = \frac{n_1^2 n_2^2}{f_1 n_2^2 + f_2 n_1^2}, \tag{5.2}$$

where $f_i = l_i/\Lambda$ are the volume pars of each nanoplanes and n_i are their refractive indices. For reasonable values of refractive index changes in the hollows layers [SKQH03] $n_1 - n_0 = -2$ to -4×10^{-1} and denser layers $n_2 - n_0 = 2$ to 5×10^{-2} and assuming that the volume part is about $f_1 = 0.1$ of the full volume, the retardation between the ordinary and extraordinary waves was determined to be $\delta n = n_{||} - n_{\perp} \sim 5\times10^{-3}$. The exact birefringence rate could be varied, since spacing between nanogratings is changing as a function of the number of acting pulses and their temporal envelope variation, indicating a certain tunability; however, $n_{||} \geq n_{\perp}$ for any arrangements of nanolayers. Such birefringence could be easily detected in a cross-polarization microscopy (CPM) setup.

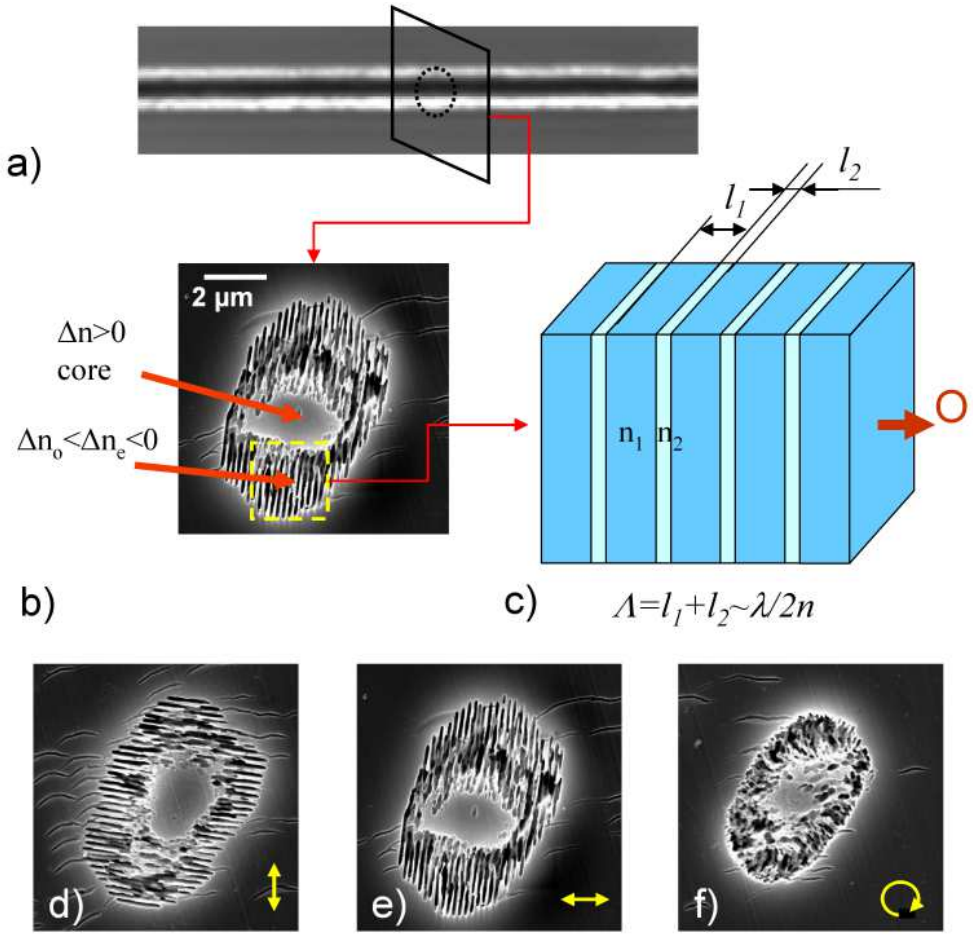

Figure 5.4: a) PCM picture of the typical type II-WG longitudinal trace and b) nanogratings revealed after cross-sections etching of written type II-WG longitudinal traces. c) The regular arrangement could be schematically presented as a structure leading to a form birefringence, that is a uniaxial crystal with its optical axis O. Nanostructured patterns for d) linearly vertical, e) linearly horizontal and f) circularly polarized writing beam.

5.3 Developing of form birefringence

As the effect of pulse accumulation is critical to nanograting formation due to the underlying positive feedback involved in the growth, the sequential effect of increasing the pulse number is analyzed below. In the present work we have studied the appearance of the birefringence regions arising under different focusing conditions. Two main cases could be emphasized in type II

regime: tight focusing, when birefringence arise almost abruptly and looser focusing, where birefringence regions form slowly from the initially isotropic type I traces (Fig. 5.5).

5.3.1 Moderate to tight focusing. Early stages.

Fig. 5.5 shows static traces induced with a variable number of pulses at a constant energy of 1 μJ. A single pulse produces a conical region of dominant positive but weak index increase around and ahead the geometrical focus toward the apex, and a confined region of negative index change before the focus. In these OB1 focusing conditions, the nonlinear propagation affects the energy redistribution via self-focusing and filamentation. At this specific energy, the self-focusing effect results in local microexplosion in the bulk that is already visible after first pulse arrival as the onset of a void-like form (white dot in the inset of Fig. 5.5a) before focus [GM97, MBR+09].

Further information can be gathered by monitoring the preferential regions of energy distribution. Here we will present the formalism described briefly in Section 3.2 and in details in Ref. [BBS+07], which analyzes the nonlinear pulse propagation in transparent materials and studies in a time- and space-resolved manner the excitation footprints. The approach takes into consideration the key features of pulse propagation such as self-focusing, phase modulation, and defocusing on carrier plasmas. The laser pulse parameters involved in the simulation are: 170 fs pulse duration (and the corresponding spectral bandwidth), 1 μJ pulse energy, and a theoretical waist at the focus of 0.9 μm. By comparing the single pulse simulation results with the experimental single pulse effects, several observations can be drawn.

Firstly, the void formation is due to a maximization of the energy exposure by self focusing. A maximal value of 2.6 J/cm^2 was calculated at the peak located before the geometrical focus at z = 75 μm. Apart of being continuously fed by the incoming light, the exposure in this region seems also prolonged due to the associated moving focus effect, accompanied all along by additional quantities of energy scattered away by the emerging plasma. The deposited energy is sufficient to achieve the temperatures in the vicinity of the softening point and to trigger thermal expansion in this restricted zone. The subsequent rarefaction leads to a negative density change.

Increasing the number of pulses leads to a replication and subsequent drift of the voids along the trace, before stabilizing the structure in the trace head position at higher accumulation rate. Though a spherical aberration was proposed as a reason for the intensity modulation [SWH+08], in the present experimental conditions, at the depth of 200 μm, this influence is minimal. During this process, before achieving the saturation level, we note also the

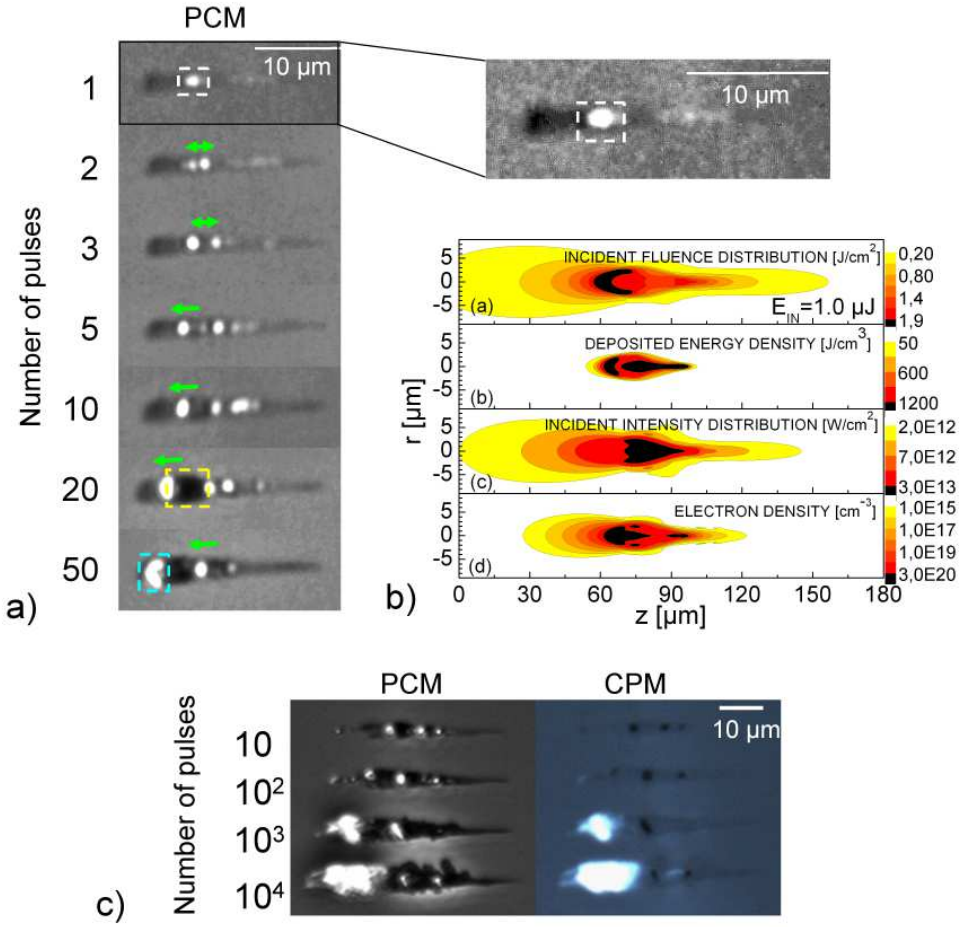

Figure 5.5: a) Early stages of developing of the nanogratings at tight focusing conditions (NA_{eff}=0.4). These are the void migration (shown by green arrows) and restructuring of voids (the example shows the splitting of the initial void after second pulse), forming lower refractive index zone in the head of the trace (blue square). b) Simulations of single pulse nonlinear energy transport are presented in [BBS+07]. c) Comparison between PCM and CPM images of static traces observed after few hundreds of acting pulses for tight focusing.

appearance and disappearance of the voids which indicate the possibility to erase laser-induced structures by subsequent irradiation. This indicates the presence of a soft low viscosity material phase around the voids. Additionally, in their vicinities or in between (see region marked as white square Fig. 5.5a), regions of compacted material with higher positive index contrast are noticed.

It is conceivable that, though triggered by a filamentary propagation, in the high N regime additional effects contribute to the positive index contrast. That makes the marked region be an interesting object for spectroscopic investigation of a pressure-thermal interplay in material modification. This will be discussed in subsequent chapters.

With a significant number of pulses per site, birefringent structures form where the initial void serves apparently as a seed event, developing in a region previously affected by weak fluence exposures. This difference between the void-like and birefringence regions can be easily detected using cross-polarizer microscopy (CPM) as seen on the Fig. 5.5c. It is seen that clear birefringent properties appear in the low refractive index change zones visible as white region only after few hundreds of acting pulses. The zones visible as white dots in the PCM (zone in white square on the Fig. 5.5c) is a result of the scattering or smaller refractive index changes supporting the suggestion that these are voids. Their early agglomeration in the zone in the head of the trace (blue square on the Fig. 5.5c) developing for less than one hundred of acting pulses still does not possess birefringent properties, which develops after.

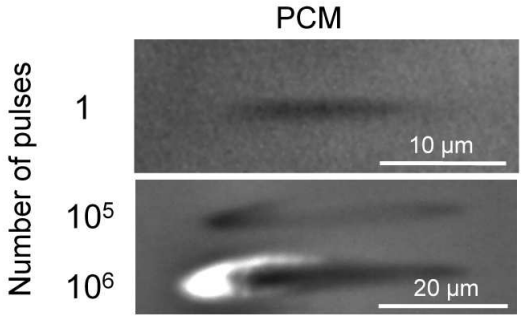

Figure 5.6: Appearance of birefringence under loose focusing conditions (NA_{eff}=0.3)

5.3.2 Loose focusing. Type I/II transition.

The previous subsection indicated that voids generated in tight focusing conditions can act as nuclei for the formation of the birefringence regions. A different behavior is to be noted for loose focusing in type I regime of writing. Loose focusing of femtosecond laser pulses has many details in common with a filament-type of interaction with the media resulting in saturation of intensity in the region of interaction. The intensity at its peak is clamped at a

level below 10^{13} W/cm^2 and electron concentration at a level below 10^{20} cm^{-3} in the plasma filament, resulting in smooth refractive index changes. An example of single trace irradiation generated by a loose focused pulses with the energy of 1 μJ and pulse duration of 130 fs with OB2 (NA$_{eff}$=0.3) is displayed in Fig. 5.6 on the top. Such smooth modification subsists for further pulses arrival up to a certain dose. However, when a critical number of pulses was surpasses, the situation changes. The type II traces could be obtained after the action of a high number of pulses as indicated in Fig. 5.6 on the bottom. This has similarities with tight focusing, since birefringence region agglomerates mainly in the region oriented towards the incoming radiation. However, this has its own signature as well. Significant part of the birefringence agglomerates at the periphery of the beam, where the laser field is weaker.

We propose that in this case, the type II regime for nanogratings formation on a initial seed centers that are not necessarily color centers but nano-rugosity resulting, for example, from stress accumulation. Cracks formation is the natural mechanism of release of the local stress, if this exceeds the strength of the glass. This could happen after the arriving of incoming pulses when high stress is already accumulated, or even because of the fluctuations in the beam quality. An important note should be made. Cracking of the glass happens not in the region of high energy, where material is softer and stress release could efficiently occur after the arrival of each pulse, but on the periphery of the trace, explaining specific form of birefringence appearing in type I/II transition mechanism. Being the nuclei for nanoplasma generation cracks are transforming to the nanogratings according scenario similar for the tight focusing regime. Though usually subcritical densities are reported upon waveguide photoinscription, it is conceivable that, due to the formation of additional seed centers in this particular region, the electronic density increases upon multipulse exposure. This way, significant energy can be locally deposited in nano-domains, leading to local phase transitions and material redistribution via viscoelastic flow.

5.3.3 Secondary light emission

A primary source of information related to the processes occurring at the interaction region is light emission. Blue luminescence visible by the eye is always observed during laser writing procedure. Except of the typical luminescence of plasma, coherent second (SH, SHG) and third harmonics (TH, THG) of femtosecond radiation were detected. These types of luminescence are discussed below.

5.3.4 Luminescence during writing

The origin of the observed luminescence arises from the relaxation of excited electrons generating during photoionization processes. Transitions between free electrons (free-free intraband transition) and transitions between conduction band and defect states or valence band could be optically active, so luminescence appears. Spectral emission at 475 nm and weak band at 650 nm for type I [RCS+07, PT11] as well as wide band centered at 550 nm for type II [RCS+07, SSM11] were reported in the literature during writing. The presence of such luminescence indicate that material changes start developing inside the glass. A similar effect was observed in the present work, since plasma luminescence and the visible material modifications occur at the same threshold pulse energy E_{th}=80 nJ for NA_{eff}=0.3 objective and E_{th}=60 nJ for NA_{eff}=0.4 objective. However, it is worth to note that if the luminescence of the same intensity is visible from the very beginning of interaction, few millions, $N \sim 10^6$, of pulses should interact with the glass to observe these modifications at lowest energies.

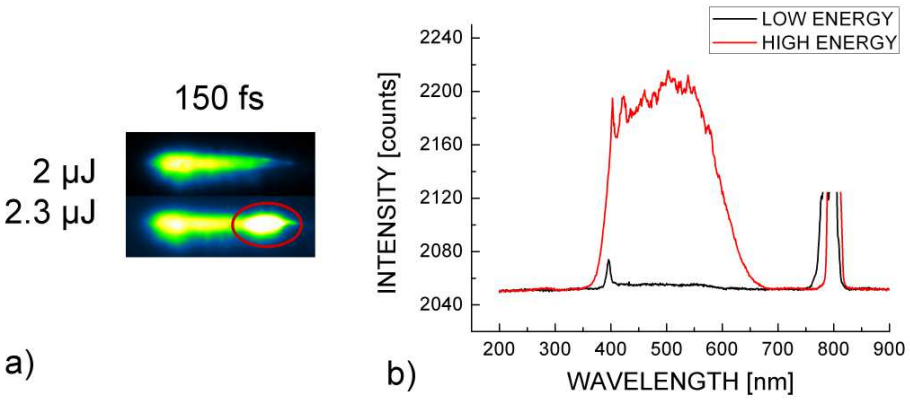

Figure 5.7: a) Plasma emission pictures at two slightly different energies: ~2 μJ laser pulses were focused by NA_{eff}=0.3 objective. b) Recorded spectra of the light emission have wide spectral distribution between 400 and 650 nm. The drop in the signal at 650 nm arises because of the cut-off of the IR reflecting mirror being used as filter for scattering femtosecond radiation (still present at 800 nm). The 400 nm peak is the second harmonic of the femtosecond radiation.

Plasma luminescence was collected in the direction collinear with the beam propagation after the focusing point. No polarization properties of the observed luminescence were detected. For a given polarization of the writing

beam, the signal of luminescence is equal for parallel and perpendicular (to the writing polarization) position of the analyzer.

A summary of spatial shape changes of this weak emission accompanying the photoinscription process is displayed in Fig. 5.1 on the right. For the case of a type I trace the luminescence region has a symmetric axial spatial distribution. Then, with increasing energy, it starts to show an asymmetric distribution upshifted towards the laser beam incoming direction, following the changes happening with static traces. It is also accompanied by scattered light. Finally for highly energetic regime (type II-WG), plasma emission is significantly increased and further non-uniformities and secondary emission regions develop with the increase of the energy dose (Fig. 5.1 bottom left).

The secondary emission spot has a much higher intensity than usual plasma. The measured spectra given in Fig. 5.7 show a continuous wide distribution between 400 and 700 nm. Investigation of the effect of the pulse duration on the emission of the second spot indicates that the luminescence is more intense for the pulses in the interval from few hundreds femtoseconds.

5.4 Coherent emission

In addition to the incoherent plasma luminescence, the nonlinearity of interaction and the symmetry change generated by plasma gradients and permanent refractive index changes create the conditions for coherent light generation in terms of harmonics of the fundamental writing wavelength. In this case generated harmonic propagates collinearly with the pulse, and can be detected after the focal point. Before its collection with the portable spectrometer, separation of the harmonic from the IR radiation was performed. Spectral filtering was done using a blue filter in the case of SHG, and spatial filtering was performed using a fused silica prism in the case of THG (fundamental wavelength can be stopped by a screen).

5.4.1 Second harmonic generation

Spectral evidences of SHG is presented in Fig. 5.8a. The onset of a second harmonic peak in the spectra is generally accompanied by plasma luminescence and a permanent modification, having the same energetic threshold. As shown on the Fig. 5.8b its intensity increases as the number of acting pulses goes up; however, the intensity of plasma luminescence keeps constant. The character of the increase of the SHG signal as a function of number acting pulses and the energy is the same as the one observed for refractive index changes (see Fig. 5.11 later); the yield monotonously increases until reaching

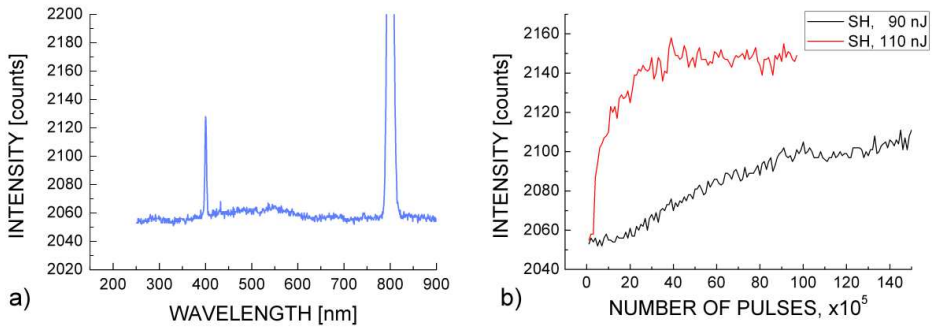

Figure 5.8: a) Spectrum of SH and b) its intensity dynamics as a function of accumulated laser pulses in static irradiation conditions typical to type I regime. 90 nJ and 110 nJ pulses were focused by the NA_{eff}=0.3 objective.

a saturation level. The rate of this increase is faster for higher energies. That is the reason why we assume that with increasing of density or refractive index changes in the region of plasma generation, the symmetry of amorphous media is broken and SHG becomes increasingly possible. One should note that the signal of SH has a drop in intensity when the transition between type I and type II is happening (not shown). This could be is explained by higher scattering on the generated material inhomogeneities.

The polarization properties of SH signal were equally studied. The signal has maximum for a position of the analyzer parallel to the writing polarization and it is almost equal to zero if analyzer is placed perpendicularly. This means that the polarization of SH is the same as the writing beam that usually happens in harmonics generation on the metal interfaces [BCJL68]. Thus, the mechanism of SHG on the free electrons seems to be dominant in this case.

5.4.2 Third harmonic generation

A peak of the third harmonic is also appearing along the visible luminescence (Fig. 5.9a). It shows a dependence on the number of acting pulses, but its behavior is different than that one observed for SHG. This behavior is displayed in Fig. 5.9b for 120 nJ pulses focused by the NA_{eff}=0.3 objective. Several regions could be identified. In the type I writing regime characterized by a low number of incident pulses, the intensity of TH is quite low. In this regime the TH intensity reaches a maximum and then it slowly decreases followed by a sudden reincrease. We will refer to this new regime as a transition

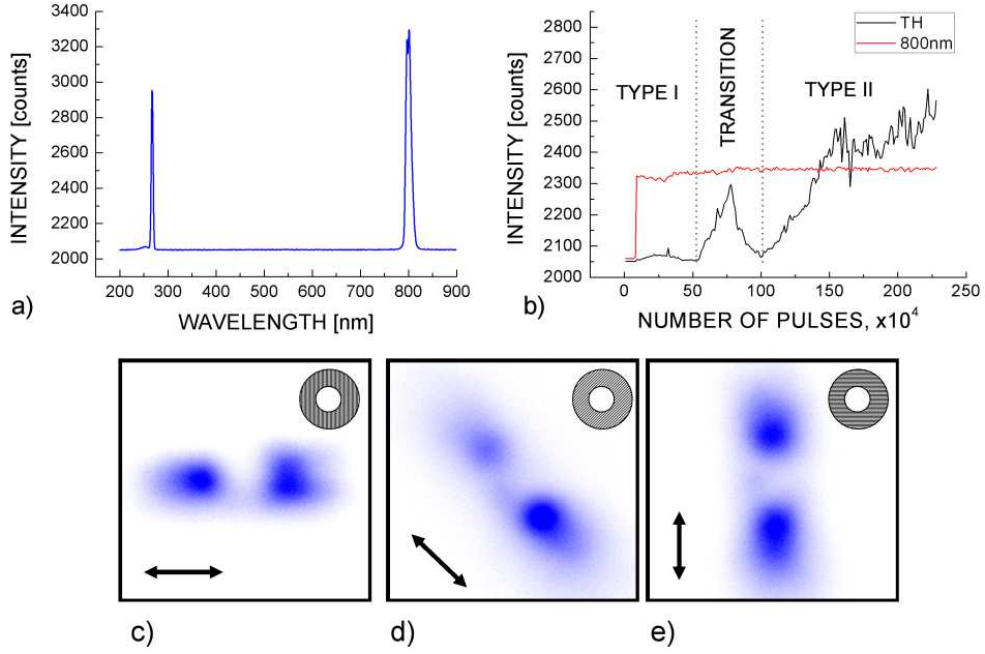

Figure 5.9: a) The spectrum indicating the fundamental and the third harmonic waves. b) Dynamics of TH intensity as a function of accumulated laser pulses in static experiment. 120 nJ pulses were focused by NA_{eff}=0.3 objective. On the bottom, anisotropic scattering of the generated third harmonic radiation for c) horizontal, d) linearly polarized at 45°, and d) vertically polarized writing laser.

regime, where static traces posses strong negative refractive index changes and the intensity of TH is one order of magnitude higher with respect to type I case. However, this transition regime is unstable. The intensity of TH drops again, until type II regime of writing occurs. This is characterized by high and permanent yield of TH signal.

The increase of the TH signal for the type II regime by an order of magnitude if compared with type I is not an usual effect. The responsible mechanism of such increase is THG on the interface [Tsa95], where it is easy to fulfill phase-matching condition $\Delta k = k_\omega - k_{3\omega} = 0$. Negative refractive index changes regions appears due to the presence of hollow single voids, agglomerations of voids or nanocracks, taking the role of such interfaces leading to efficient THG.

Thereby THG could be used as a simple tool for monitoring the cracking of bulk glass and nanogratings formation. Moreover, periodical self-

assembling of the nanoplanes results in the diffraction of the generated TH. To quantify the diffraction process, the diffracted patterns were projected on the white paper screen and the detected blue fluorescence of the paper was imaged by the CCD camera placed after the screen. The patterns consist of the two symmetrical spot arising on the both sides of the nondiffracted 800 nm radiation. The examples are given in Figures 5.9(c,d,e).

The angle of diffraction was measured to be ∼58° in air, that correspond to the diffraction of 267 nm light on the grating with a period of ∼300 nm. We recall that the orientation of the nanogratings is developing in the direction perpendicular to the polarization of the writing beam [SKQH03]. Figures 5.9(c,d,e) illustrate how the diffraction patterns are rotating with rotation of the writing polarization (shown by arrow).

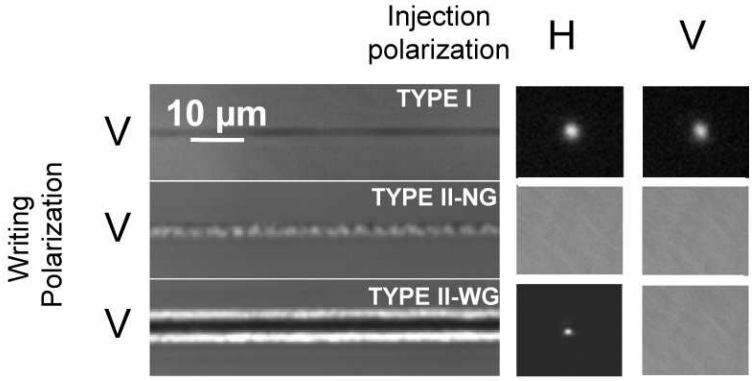

Figure 5.10: Polarization dependent optical guiding in various types of longitudinal traces written by linearly polarized (vertical) 800 nm femtosecond laser radiation. Images in the left frame show side-view PCM pictures of the photoinscribed type I, type II-NG and type II-WG longitudinal traces written with a linear polarization indicated on the left side. The right frame shows near-field modes for injected IR (800 nm) radiation for several polarizations of injection indicated at the top.

5.5 Fabrication of polarization sensitive components

The above discussion has put into evidence the appearance of different regimes of silica modification, each carrying specific properties. These were divided in type I and type II features mainly based on PCM appearance and the onset

of the nanopatterns. However, additional differences can be observed in their guiding properties as well. This will be discussed below. Figure 5.10 depicts examples of type I and type II (guiding and non-guiding traces) laser-induced longitudinal traces for different polarization orientations together with near-field modes of guided HeNe light.

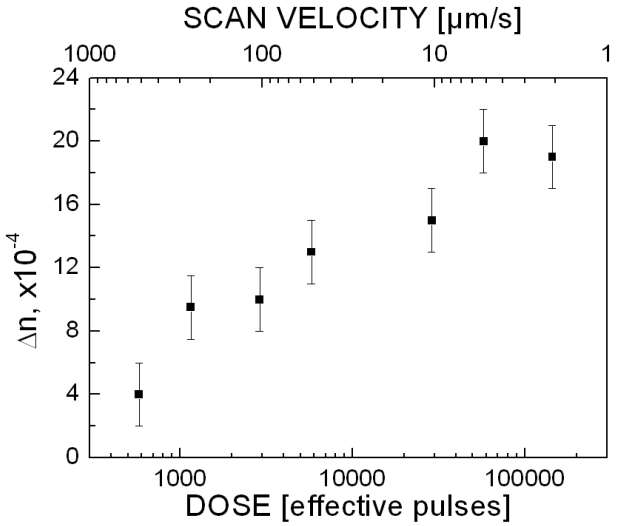

Figure 5.11: Refractive index changes induced for type I waveguides written with different velocities of the translation stage. Waveguides were fabricated with 1 μJ laser pulses following at the repetition rate of 10 kHz, focused by a NA_{eff}=0.3 objective.

5.5.1 Type I waveguides.

Femtosecond induced type I traces (depicted in Fig. 5.10 on the top) show normally a smooth type of modification as noticeable in the PCM traces, with weak positive index changes in the range of 10^{-3}–10^{-4}. The traces were written by 1 μJ pulses focused into the sample by the NA_{eff}=0.3 objective at different translation speeds at 10 kHz laser repetition rate. The tracks were subsequently injected with polarized 800 nm light. No noticeable polarization sensitivity in light transport along the traces was observed, since both vertical (V) and horizontal (H) orthogonal polarizations are equally guided (see Fig. 5.10). The near field modes at the output of the traces could be analyzed then by projection via an imaging microscope setup on the CCD camera.

The minimal mode diameter propagating in the waveguides corresponding to traces written at a translation speed of 1 μm/s is measured to be 11 μm. This is higher than the diameter of the waveguides cross-section, measured to be less than 5 μm. The maximal refractive index changes corresponding to this trace is equal to 2×10^{-3}. This value was limited by the dose of 10^5 pulses since at lower translation speeds a transition to the type II occurs. The dependence of the induced refractive index changes as a function of translation stage velocity is shown in Fig. 5.11. Refractive index continuously increases as a function of accumulation dose.

Comparing near field intensities distribution for longitudinal traces with different lengths, we estimated the losses of these waveguides at less than 1 dB/cm.

5.5.2 Type II waveguides.

We have seen before that the type II regime could be divided in two groups: type II-WG, where the trace has guiding properties (with a positive Δn core and negative index cladding), and type II-NG, where guiding is not possible (Δn <0). To illustrate the process, type II-WG traces were written by 1.95 μJ and 140 fs laser pulses focused by the NA_{eff}=0.3 objective at a translation speed of 10 μm/s at 100 kHz repetition rate. The traces show as expected a central axial high contrast positive RIC, bordered by narrow rougher edges of negative index change or scattering zones. Upon injection with 800 nm light we have observed a notable behavior. Type II traces indicate light guiding properties only when the injected light has the electric vector perpendicular to the initial writing beam vector; a different polarization being scattered away. This indicates the lower losses for an electric field propagating parallel to the orientation of nanoplanes, that can be explained by the scattering properties of the nanoplanes. The near field mode is strongly confined. It has diameter 5.8 μm that is twice smaller if compare with the propagating mode of type I waveguides. That could be explained by higher refractive index changes induced at higher energetic regimes, as well by stronger mode confinement due to the presence of a surrounding negative RIC zone in the form of a birefringent cladding.

Transmission losses for the propagating polarization were estimated as well. For guiding polarization waveguides writing with shortest pulses the losses were estimated on the order of 20 dB/cm.

To optimize the parameters of produced type II traces, different writing velocities and pulse durations were applied. Figure 5.12 shows the dependence of the intensity of the transmitted mode as a function of the sample translation velocity. It can be seen that the transmission monotonously de-

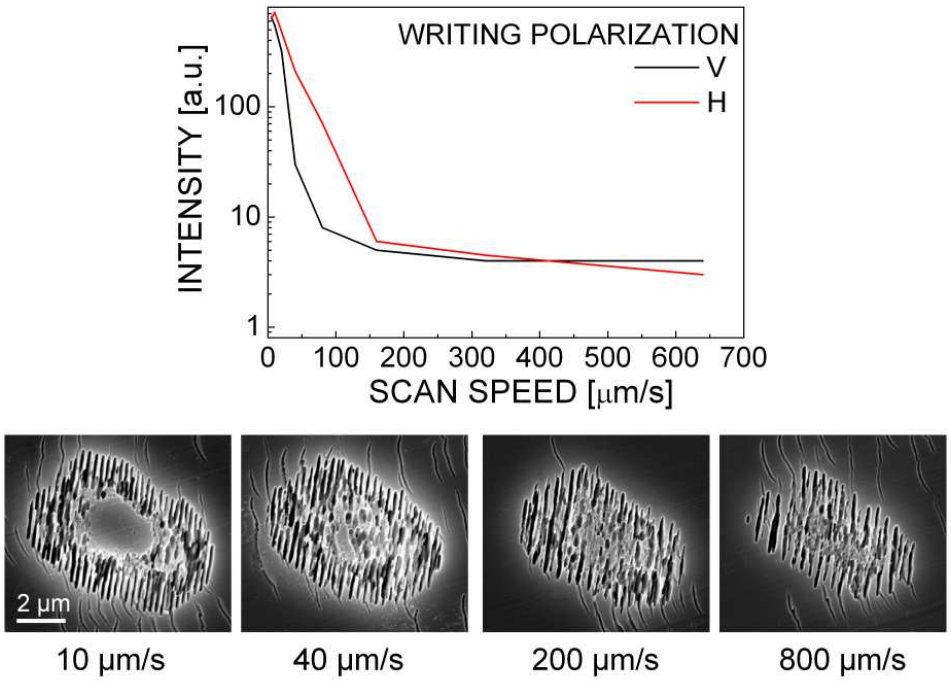

Figure 5.12: SEM images of transverse type II cross-sections of the longitudinal traces indicating the morphological differences and the polarization effects for light transport in the strong type II regimes at 285 fs incident pulse duration. The effect of the writing speed is also indicated, leading to a velocity dependent amount of nanostructured domains in the trace and WG to NG transitions

creases as velocity increases. SEM picture of nanogratings reveals the origin of this behavior. At low velocity a solid core of positive RIC is presented, that allows the mode propagation. However, with increasing translation velocity the guiding core gradually disappears. Guided mode then scatters away. The existence of such a core has been already discussed in the previous sections. The probability of such erasure is higher for low velocities of the sample translation, since higher number of overlapping pulses are acting in the process.

The optical losses were evaluated as a function of the pulse duration. The results are presented in Fig. 5.13. Type II waveguides shows the highest transmission if written with ∼500 fs laser pulses. In this case the losses in the waveguide for the guided polarization drop from the 20 dB/cm in case of 140 fs pulses to the value ∼7 dB/cm. This is consistent with the

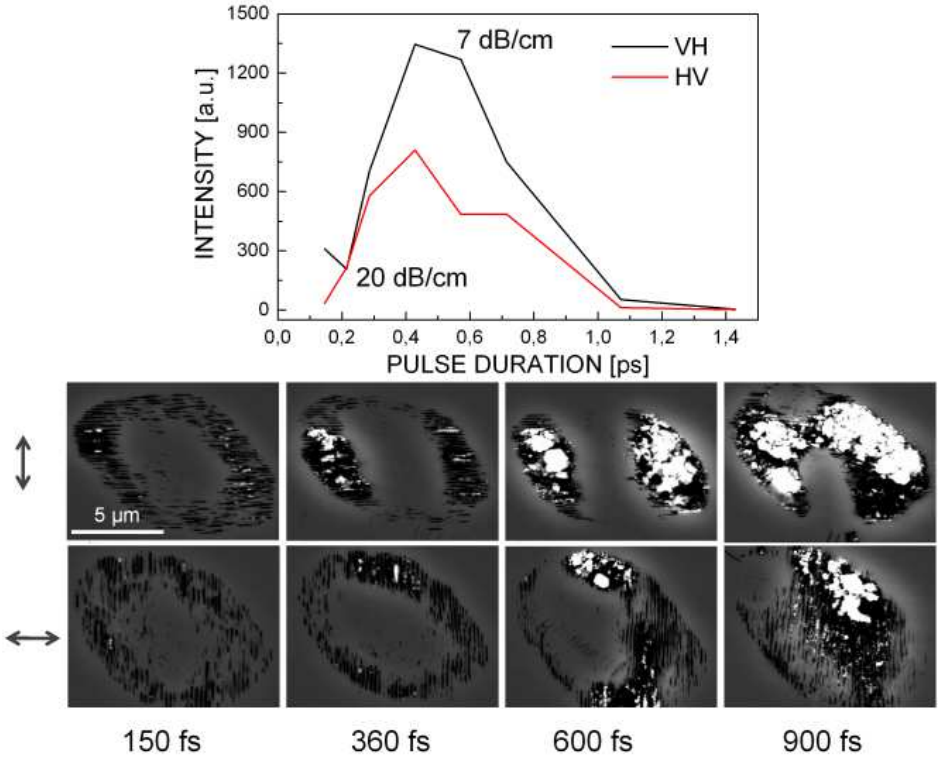

Figure 5.13: Loss optimization in type II-WG by varying the writing pulse duration. The scan velocity is kept constant at 10 μm/s and the input power is 2 μJ. Note the change in the nanostructure fill factor and the increasing asymmetry in the transverse profile. The visible white substance is the Ce powder attached to the structures during the polishing process.

behavior of luminescence during writing. We recall that strong luminescence, connected with strong material reorganization, from the region of positive refractive index changes (see bright spot in Fig. 5.7) was equally detected for longer pulses. This means that using ~500 fs laser pulses erasure is going more efficiently and smooth cores of positive RIC can be produced, favoring the lower losses. SEM pictures of cross-sections of waveguides written with different pulse duration presented in Fig. 5.13 illustrate this idea. Once pulse duration becomes larger, the core of the waveguides becomes more clear. However, the situation reverses after 600 fs, when nanogratings starts to dominate at the cross-section.

5.6 Fabrication of hybrid optical devices

The presence of the nanopatterned region and its intrinsic birefringence suggests the possibility of achieving additional optical functions related to polarization. The TE, TM components can be independently controlled by a phase delay or polarization dependent scattering in order to achieve good efficiency, and low loss type I waveguides could be combined with polarization control type II traces. Operating by the type I and type II traces as a base block elements, more complex optical elements could be fabricated [CMM+09, MCH+10]. Several examples are given below.

5.6.1 Polarization optical router

A conceptual view of a polarization optical router written by femtosecond polarized light is presented in Fig. 5.14. The router is assembled as a hybrid structure consisting of type I and type II waveguides. The writing polarizations are marked on the left. The outer type II waveguides are written with 1.95 μJ laser pulses at the speed of 20 μm/s and with orthogonal polarizations, and the central type I waveguide is written with pulse energy of 0.45 μJ at the speed of 200 μm/s. The length of waveguides is 9.3 mm and the separation is 15 μm. These writing conditions and the length of the waveguides were chosen to allow the efficient leakage of the linearly polarized light injected into the central type I waveguides to the adjacent type II waveguides. Mode transition is going via an evanescent coupling mechanism, thus, further propagation in type II waveguides is possible only if its polarization allows. As the two type II waveguides were written with either vertical or horizontal polarization, the light will penetrate and further propagate in the lateral waveguides according to its polarization. For the cases of horizontal or vertical linearly polarized injected light guiding mode exists in the top or bottom waveguides (see Fig. 5.14).

5.6.2 Phase retardation devices

The combination of type I and type II-WG traces can be used to fabricate polarized or polarization maintaining waveguides, showing equally the potential to induce controlled phase retardation with low losses. An example of this is given in Fig. 5.15 which indicates the possibility of rotating the polarization. The scheme represents single waveguides possessing a region with defined birefringent properties due to the presence of type II part. The type I waveguide being written using 1 μJ polarized laser radiation at 100 μm/s, and type II similarly at 10 μm/s. The pulse duration is 140 fs for both writing

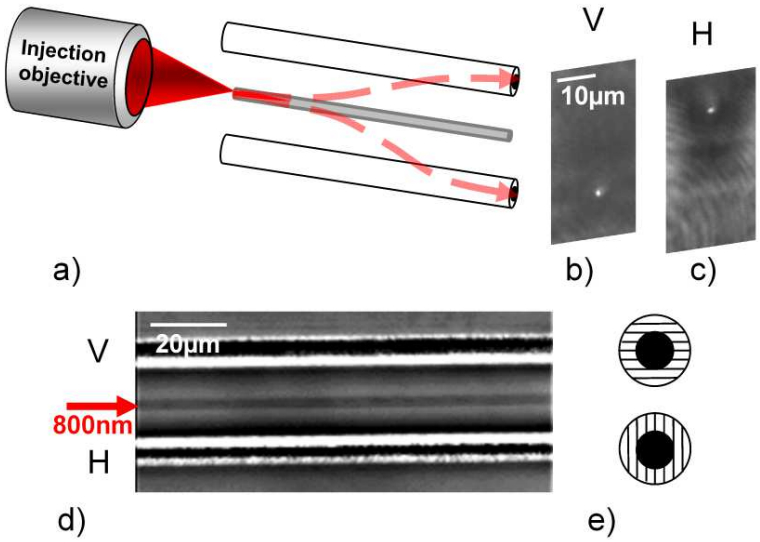

Figure 5.14: a) Schematic view of a polarization optical router written by femtosecond polarized light in fused silica. b) and c) Near field modes as a function of vertical (V) or horizontal (H) polarization of injected light. d) PCM top-view picture showing a hybrid structure consisting of type I and type II waveguides. e) The latters are written with particular orientation of the nanogratings

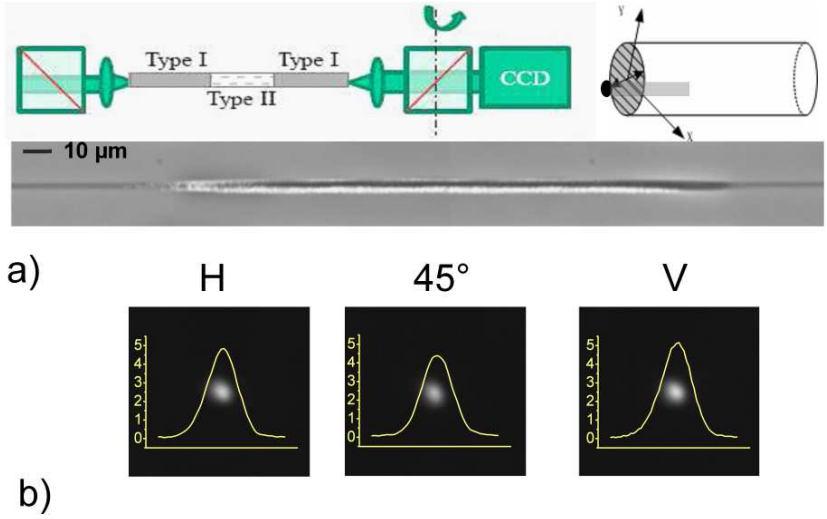

Figure 5.15: Demonstration of a waveguide QWP consisting of mixed type I and birefringent type II-WG traces. a) Scheme of device and its PCM picture. b) Near-field mode of the parallel, 45° polarized and perpendicular polarized output components of the initially linearly polarized 633 nm laser light.

Table 5.1: Qualitative table of writing regimes.

	Type I	Type II (NG)	Type II (WG)
Energy	low, 100 nJ	high, ∼200 nJ	high, ∼ μJ
NA	low, <0.3	high, >0.4	high, >0.4
Pulse duration	<140 fs		500 fs
Number of pulses	$<10^5$	>100 [1)] or $\sim 10^6$ [2)]	$\sim 10^4$ [1)]

[1)] for high-NA objectives
[2)] for low-NA objectives

conditions. The length l of the type II structure determines the phase shift between TE and TM waves according to the ratio $\delta\varphi = \delta n \times l/\lambda$. A length of 170 μm was found to introduce a $\pi/2$ shift. For the injected light with an input linear polarization at 45° with respect to the orientation of the nanogratings, this structure performs a quarter-wave plate (QWP) function. Despite the different propagation efficiencies along the fast and slow axes corresponding to the birefringent cladding, we do not expect severe selective attenuations for the lengths involved, ensuring an efficient transmission of light.

5.7 Conclusions

In conclusion we have demonstrated that the energy deposition largely determines the structural transitions leading to refractive index changes and optical anisotropies. Two main regimes were identified with results being summarized in the Table 5.1.

Type I longitudinal traces are characterized by low density of energy deposition achieved by using objectives with NA<0.3 or using short pulse durations, τ_p<140 fs. Refractive index changes could be controlled by the number of effective pulses interacting with the glass.

High energy doses and prolonged exposure (type II regime) lead to the self-arrangement of the material in nanolayers. This regime could be further divided into non-guiding or guiding traces. The guiding in type II-WG traces is ensured by the presence of a positive refractive index core surrounded by a negative refractive index change (birefringent) cladding. The presence of the core is defined by the ability to erase the birefringent region by the isotropic positive refractive index part in the filamentary tail upon the sample translation. With higher energy or higher number of incident pulses (equivalent

to a lower velocity of the sample translation) the complete erasure becomes more probable. It is most effective for pulse duration of several hundreds of femtoseconds.

We assume that the birefringent regions are developing from the nucleation centers by the cumulative action of few hundreds pulses. Void forming in moderate to tight focusing regime (NA>0.4), and cracks/cavities appearing after local stress release or other density inhomogeneities in loose focusing conditions(NA<0.3) could lead to these nucleation centers. Birefringence properties could be further controlled by varying the pulse duration and accumulation dose.

The presence of birefringent regions affects the polarization properties of embedded longitudinal traces that can be used in optical device microfabrication. Polarization sensitive waveguides, phase retarders and optical router were demonstrated.

Chapter 6

Photoluminescence spectroscopy

Luminescence was often reported in laser damaged fused silica and considered as an effective way to characterize the glass structure in the modified regions. As it was discussed in Chapter 5, various focusing conditions result in a different character of propagation of femtosecond pulses, influencing the energy deposition in the glass network; thus, we expect the generation of different types of defects there. We remind here that as a result of the action of two competitive phenomena, focusing of laser pulses and defocusing by the generated plasma, two major types of damage could be produced. This will induce either void-like structure at tight focusing or type I smooth isotropic modification at loose focusing as a result of filamentation. Moreover, the repetitive character of interaction of femtosecond laser pulses with materials gives a rise to incubation and accumulative effects. These play an additional role, inducing an increase of the refractive index changes as a function of number of incoming pulses or lead to appearing of type II birefringent traces. So it is natural to expect the generation of different defects not only under different focusing conditions but also in different accumulative regimes.

In this chapter we will attempt to fill these gaps by studying type I, type II and void-like damages separately, paying attention to focusing conditions and using different light excitation sources to carefully assign emission bands to structural defects. The objective is to identify particular electronic and structural modifications related to the observed index change appearances.

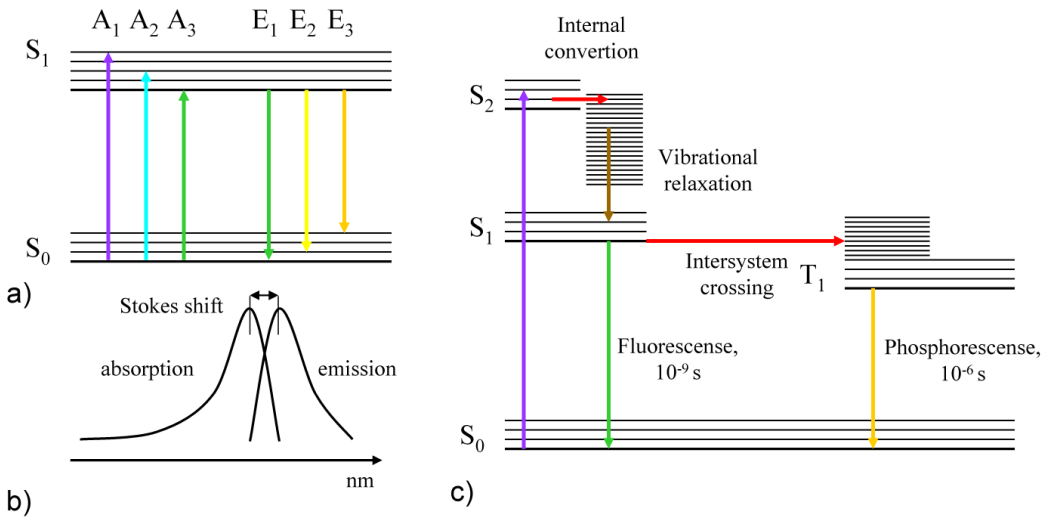

Figure 6.1: Photoluminescence fundamentals. a) Jablonski diagram presenting possible transitions between the ground and excited states of a point defect and b) the absorption and emission spectra of such system showing Stokes shift. c) Transitions between the ground state S_0 and excited states S_1, S_2 and T_1 of a point defect explaining various steps in fluorescence and phosphorescence.

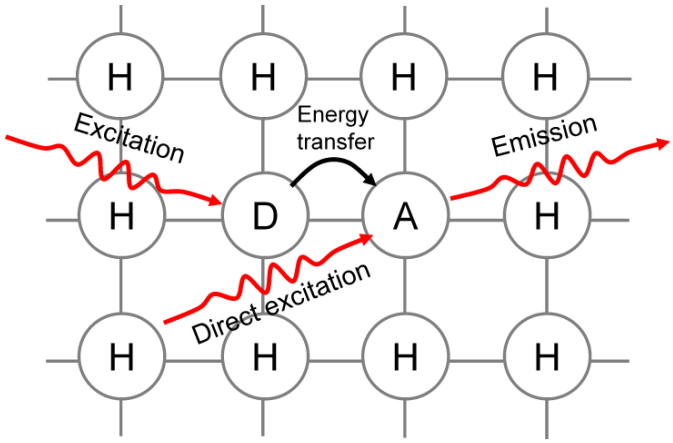

Figure 6.2: Schematic representation of the role of energy donor defect (D) in the luminescence process in relationship to an energy acceptor defect (A) and the host lattice (H).

6.1 Optical spectroscopy of defects in laser-modified silica

Photoluminescence is the general term describing the process of emission of light which is stimulated by previous light absorption. This can be described as an excitation event to a higher energy state and then a return to a lower energy state accompanied by the emission of a photon. The process is qualitatively displayed in Fig. 6.1a involving two levels S_0 and S_1. Usually emission happens at shorter wavelengths, so a gap exists between the maxima of absorption and emission spectra defining the Stokes shift. This is explained by the fact that after absorption electrons vibrationally relax to the lowest energy state of S_1. The excess of energy defined by the vibrational band width is transmitted to lattice vibration and characterizes the Stokes shift value. This is represented in Figures 6.1(a,b) where absorption quanta A_i always have higher energies than the emitted ones E_j.

Jablonsky diagram is a good way to describe the electron-phonon coupling and optical transitions in molecules or point defects in solids. Once excited, several de-excitation ways are possible with respect to the states indicated in Fig. 6.1c. Vibrational relaxation which is the transition to the lowest vibrational state of the same electron level, or internal conversion, a transition between electron orbital states (such as S_2 to S_1) are the most probable. Internal conversion and vibrational relaxation takes typically picoseconds to complete and bring the molecule back to the lowest energy level of S_1. A further process of radiative decay from an excited state to the ground state is called *fluorescence* and it takes approximately nanoseconds. Another pathway of energy loss occurs after intersystem crossing by means of a forbidden transition to the triplet state. Overlapping of the triplet state vibrational energy levels with the lowest energy level in S_1 favors intersystem crossing followed by internal conversion to the lowest energy of T_1. The further transition to the ground state may occur with or without photon emission. If this transition is accompanied by photon emission, this process is called *phosphorescence*. The time scale of intersystem crossing and consequent phosphorescence is on the order of 10^{-8} to 10^{-3} s, one of the slowest forms of relaxation.

Another scenario of a phosphorescence process occurs in inorganic solids, which is schematically represented in Fig. 6.2. The defect generated in the host lattice (H) creates a center which can be excited to luminescence, when it absorbs excitation energy and converts it into visible radiation. This can happen either via its direct (or resonant) excitation, or it may occur that the defect center does not have a significant absorption for the available excita-

tion energy. In such a case it may be possible to use an *"energy donor defect"* (D), which absorbs the excitation energy and then transfers this energy to the *"energy acceptor defect"* (A), which can then emit its characteristic luminescence [DeL80].

6.2 Apparatus for measuring photoluminescence spectra

The photoluminescence spectra of laser irradiated samples were recorded with a Horiba Jobin Yvon confocal Raman microspectrometer ARAMIS. Three laser sources were used for excitation, which offer four excitation wavelengths: light from a HeNe laser at 633 nm (1.96 eV), from an Argon ion laser (Ar^+) at 488 nm (2.54 eV), and from a HeCd laser at 442 (2.81 eV) and 325 nms (3.82 eV). These wavelengths usually cover the excitation bands of NBOHC and ODC centers.

The principle of collection is the following. Being focused into the bulk by the objective, the excitation induces scattering of light, which was collected by the same objective in a backscattering configuration. Spatial resolution was defined by the choice of the objectives. For visible wavelengths an Olympus MPLN 50× NA=0.75 objective was used. This allows a spatial resolution of approximately 1 μm with a working distance of 0.3 mm, making it suitable for collecting signal in the bulk. An LMU 40× NA=0.5 objective was used for the UV excitation light with a spatial resolution of approximately 1.5 μm. Depth (axial) resolution is defined by the choice of the confocal diaphragm; diameters of 50 μm define depth resolution of 3 μm for the 50× objective and a slightly higher value for the 40x UV objective. The choice of a confocal diaphragm was made in order to ensure a high signal but with the ability to preserve the observation of local changes in the bulk. The employment of a grating with 150 grooves per mm defines a spectral resolutions of 3 cm^{-1}.

Defect bleaching, that is loss of the ability to fluoresce, observed in the produced damages, limits the abilities of measuring stable defects. The bleaching can happen either spontaneously with time at room temperatures or upon incident light due to photon-induced chemical damage and modification of electronic structure of defects. This is called photobleaching. The photobleaching observed during excitation with Ar^+ and HeCd laser was an important factor of decreasing PL defect signal. Therefore, usually low energies of the laser were used. Additionally, bleaching is critical in order to capture satisfactory images. To diminish the role of an artifact of bleaching with time, the spectra were recorded in the same day of laser irradiation.

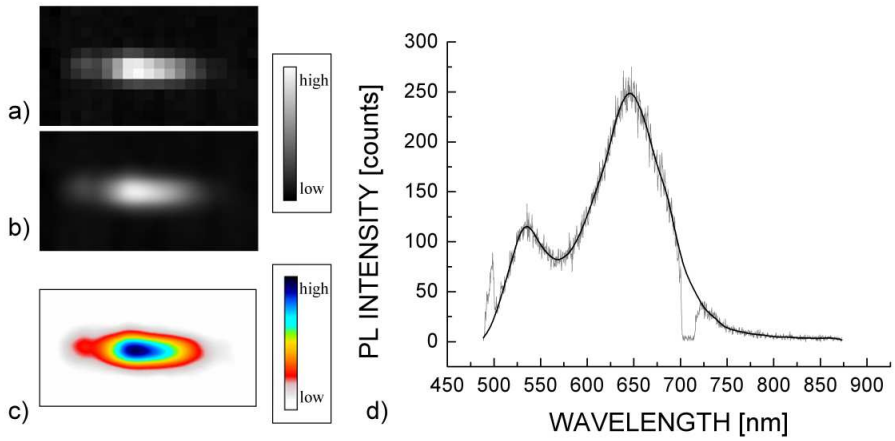

Figure 6.3: Example of data treatment indicating the smoothing procedure applied to a), b) c) spectroscopic 2D maps of laser-induced modifications and d) spectra. a) Initially pixelized 8-bit gray-scale image, b) the same map after Mitchell filter application, c) false colors emphasizing regions of equivalent intensity. d) Sample spectrum before and after the application of smoothing procedure.

6.3 Post-processing of PL spectra

For qualitative assignment of different regions of laser affected zones to their specific defect patterns, it is important to have simultaneous spectral and spatial information. With this purpose, 2D PL maps were taken point-by-point by scanning the area in the vicinity of the modified regions. A mean intensity of the each PL band can, thus, be taken and assigned to every point. This allows to plot spectral maps separately for each PL band. Since the size of the damage is comparable to the resolution of the microscope, the maps become discrete, making interpretation difficult. For better visual reading the maps were smoothed with Mitchell filter afterwards and information displayed in false colors. An example is given in Fig. 6.3a.

One should note that all spectral maps have been normalized individually to obtain maximal contrast between unmodified background and the useful signal from modified zone. The sample geometry and trace depth affect the total signal, therefore, only qualitative comparison of the PL spectral patterns can be made between different traces.

The spectra themselves were equally processed. Firstly, spikes from cosmic rays and different artifacts, such as the cut-off due to used notch filter and present in spectra under Ar^+ laser excitation, were removed. Applying

a low bandpass filter in the Fourier transform space, which transmits 10 % of the frequencies, the noise was practically removed and only slowly varying signal envelopes remain, which are modulated by the components of noise with low frequencies. This modulation was removed by a cubic regression fitting. The resulting spectrum perfectly matches the measured spectra in most cases, where signal to noise ratio is rather high. A comparison of the spectrum produced by such a smoothing procedure and the original one is presented in Fig. 6.3b. In those cases where S/N ratio is very low because of the weak signal, spectra are presented without changes.

6.4 Results. Single shot interaction

6.4.1 Moderate energy

As we have seen in Chapter 5, usually, single shot traces produced in rather tight focusing regime consist of different regions of index modulation. PCM allows to identify these as black part of positive index modification and white regions, which can be assigned to voids. As indicated before, the voids were associated with a mechanical rarefaction effect at the self-focusing point, the black part being the result of filamentation. Different regimes of energy absorption and relaxation which produce such dramatically opposite damage types may generate different defect centers as well. These hypotheses were studied by spectroscopy means and the results are displayed in Fig. 6.4.

Single shot damage was produced by 0.5 μJ pulses focused by the OB1 (NA_{eff}=0.4) objective. These energies and focusing characteristics are sufficient conditions to produce in the same trace modulated positive and negative refractive index changes. The typical investigated region is presented at the top of Fig. 6.4 (PCM image). The damage zone was studied by three excitation sources and characteristic PL bands were monitored. These are bands centered at 650 and 545 nm. Let us first discuss the correlation between PCM images and spectral maps for different excitations.

Only the band centered at 650 nm is present under HeNe excitation. This PL band corresponds to the relaxation of non-bridging oxygen hole centers. HeNe excitation at 633 nm directly excite NBOHC via the 2.0 eV absorption band, which relaxes emitting light at 650 nm (1.9 eV). The plotted map of NBOHC PL band intensity (measured as the peak of the 650 nm emission) shows a uniform distribution of these centers in the black region of the trace (denoted as B). In the part corresponding to the white region intensity of PL signal lowers significantly.

Under Ar^+ laser excitation at 488 nm, the luminescence band centered

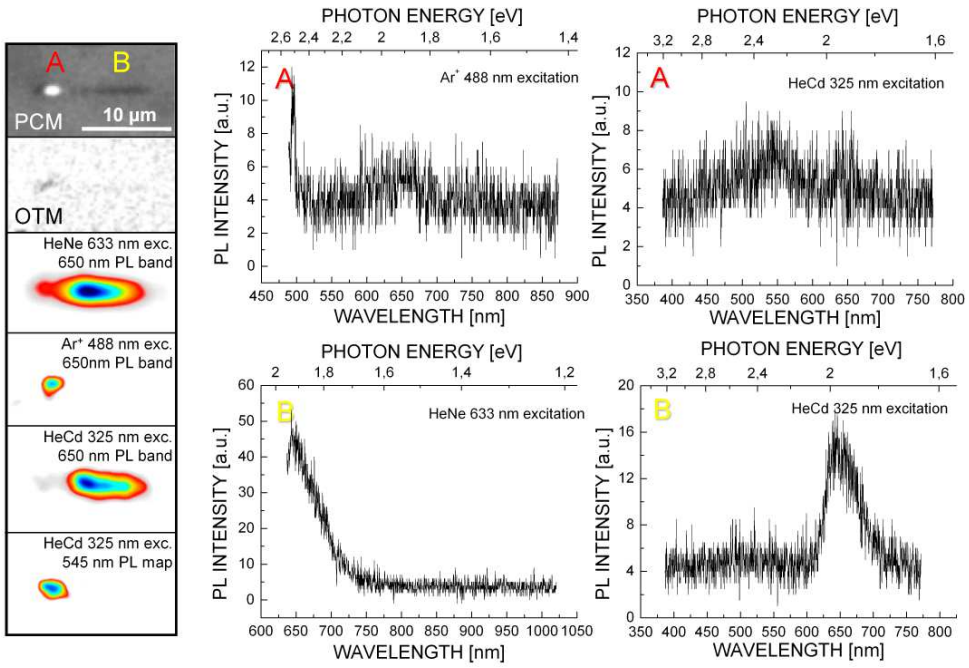

Figure 6.4: PL information measured in different regions of single shot damage, produced by E=0.5 μJ pulses focused by the NA_{eff}=0.4 objective. PCM and OTM at the right show the produced damage and below luminescence maps of the 650 and 545 nm bands excited by different sources of light are depicted. On the right, spectra collected in the void region (denoted as A) and positive index variation (denoted as B) are presented. Spectra were recorded right after writing. For excitation, light with 633, 488 and 325 nm wavelength was used.

at 650 nm was also found. However, the PL is very weak and happens only in the white region (denoted as A). That is luminescence of NBOHC, but the excitation mechanism of these defects is unclear, because there is no absorption band of NBOHC which corresponds to 488 nm. That involves the contribution of another absorption band that subsequently redistributes energy to NBOHC. Detailed discussion of possible excitation mechanism will be given further.

Under HeCd excitation at 325 nm the main band which is present is the luminescence at 650 nm. It was detected almost everywhere except of the region of the void where the PL signal is lower, as it was observed in the case of HeNe excitation. This band appears after NBOHC excitation via the absorption at 4.8 eV band and subsequent radiative relaxation. This absorp-

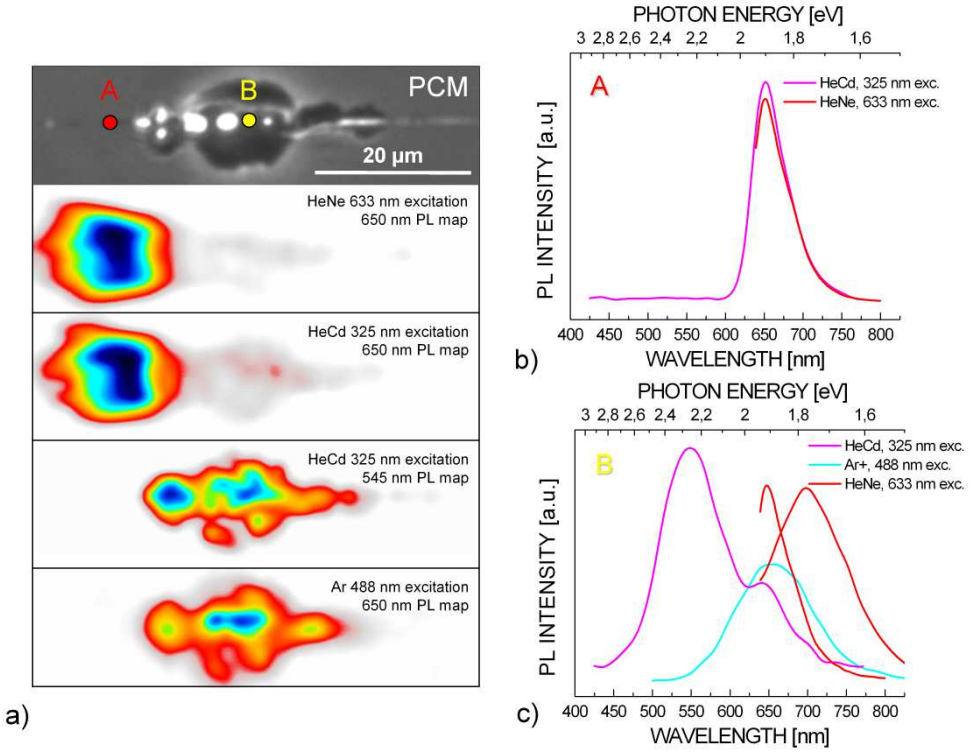

Figure 6.5: PL spectra measured in different regions of a high energy single shot damage, produced by E=30 μJ pulse with the duration of 150 fs focused by NA_{eff}=0.4 objective. a) PCM image of the produced damage and its 2D spectral maps for 633, 488 and 325 nm excitation. b) and c) PL spectra collected at the regions marked (A) and (B) on the PCM image respectively. (A) corresponds to the region of maximum of NBOHC signal, where there are no significant refractive index changes. (B) corresponds to the region of high refractive index changes. Spectra taken under 325 nm (magenta line), 488 nm (cyan line) and 633nm (red line) excitation.

tion band is rather wide (FWHM=1eV), that is enough to excite some part of the centers via the side wing of the NBOHC absorption band. Another type of luminescence takes place in the void region, where a weak band centered at 545 nm was found. This one could be assigned to the luminescence of E'_{δ} centers.

6.4.2 High energies case

An increase in absorbed energy involves additional mechanisms of relaxation of more "violent" character, such as thermoelastoplastic processes leading to energy release via pressure or shock wave generation. This should involve the appearance of a characteristic pattern of defect centers and network reorganization, particular for the high energy regime. Keeping the focusing objective the same, one can rise up the pulse energy, increasing also the deposited energy density. Drastic changes happens with the permanent damage. These changes become apparent on the PCM and photoluminescence maps of single shot produced by focusing 30 μJ pulses with the NA_{eff}=0.4 objective as illustrated in Fig. 6.5.

Let us first discuss the spatially resolved luminescence characteristics corresponding to the different locations on the trace. The 650 nm PL at HeNe excitation shows a strong signal before the localized permanent damage. This is the region denoted as A in Fig. 6.5. The PL signal at the same wavelength which follows the shape of the permanent damage is present as well, but its intensity is lower by an order of magnitude. In most of the regions of permanent damage PL occurs at 650 nm; however, sometimes the wavelength is red shifted to ∼700 nm, as indicated in Fig 6.5c. This wavelength shift could happen due to environmental changes in the void regions. A weak 650 nm PL was equally observed under Ar^+ laser excitation in the regions of permanent relative index changes. The shape of permanent modification and the shape of luminescent regions coincides. This indicates the presence of an intermediate state in this region as NBOHC cannot be efficiently excited at 488 nm. No shifts in the PL 650 nm band as in case of HeNe excitation were observed. PL under HeCd UV excitation confirms the observation explained above: shape of the 545 nm PL map coincides with the permanent damage, and strong PL signal centered at 650 nm was observed in the region where there are no refractive index changes.

6.5 Accumulation effects

6.5.1 Low number of pulses

We have seen that the single pulse trace at energies above P_{cr} show two characteristic features; a void-like region and a high index region in the filamentation zone. This initial modification develops as further pulses arrive at the same place. These changes could be explained by accumulation and incubation effects as the electronic, structural, mechanical, and optical properties changes with each pulse (see the discussion in Chapter 5). We focus here par-

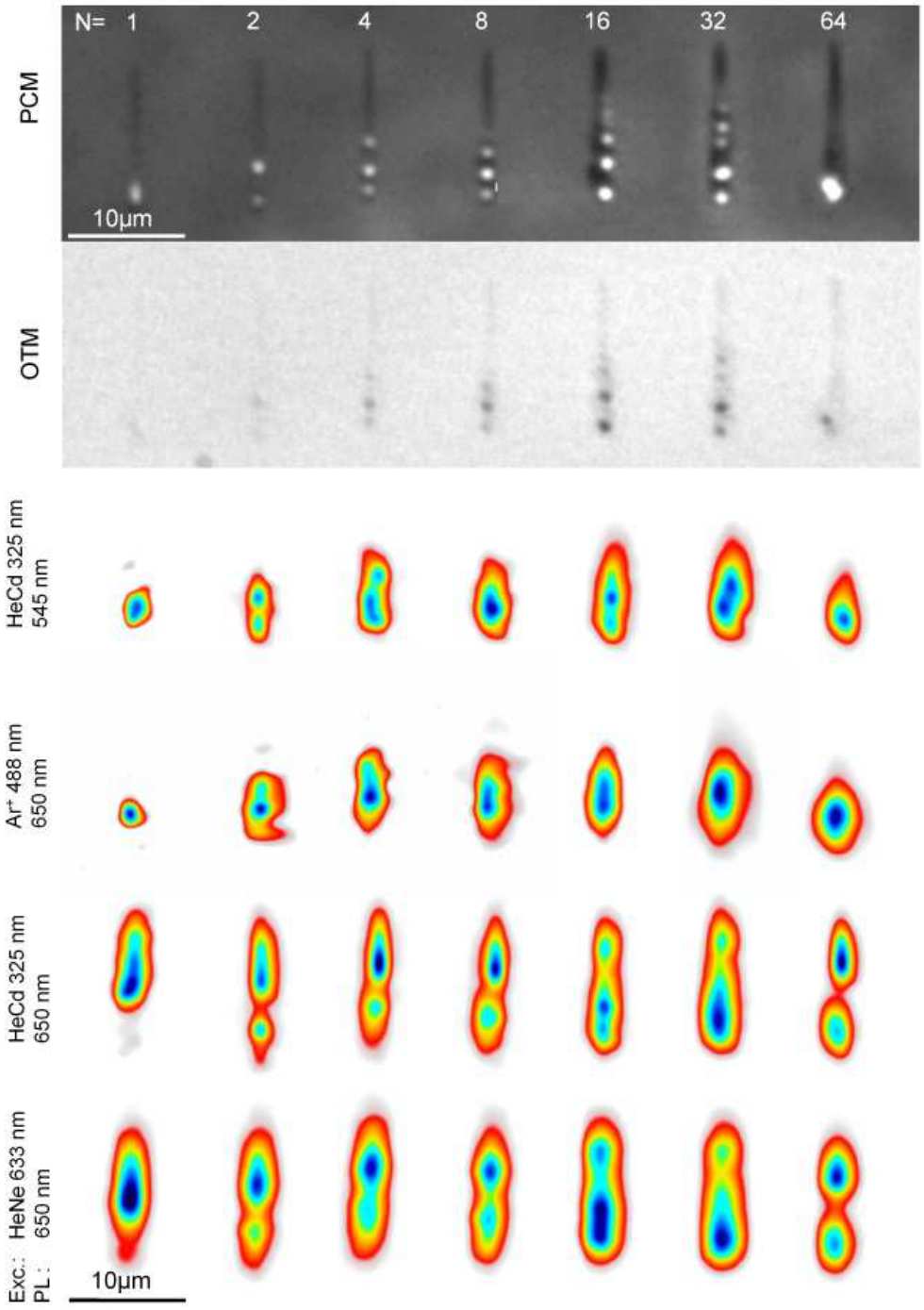

Figure 6.6: On the top, PCM and OTM images of written traces produced by N=1, 2, 4, 8, 16, 32 and 64 number of pulses with an energy of E=0.5 μJ focused by NA_{eff}=0.4 objective. On the bottom, 2D spectral maps of different PL bands observed under 633, 488 and 325 nm excitations. Normalization was performed individually for each map to obtain its maximal contrast.

ticularly on the behavior of electronic changes. For the investigation of the accumulation dynamics of defects formation, an array of traces produced by 1–64 subsequent shots was prepared in the same irradiation conditions as the single shot damage reported previously in the moderate energy case. Typical spectral maps and recorded spectra are presented in Figures 6.6 and 6.7.

The PL investigation follows the same procedures as reported previously observing the spectral patterns under visible and UV excitations. Again, all spectra show luminescence at 650 nm during 633 and 488 nm excitation and two bands at 650 and 545 nm during 325 nm excitation. Notably, the patterns of 650 nm luminescence maps under 633 and 325 nm excitation are similar for all traces, that allows us to conclude that in both cases NBOHCs are excited directly. That means that these maps show a real distribution of NBOH centers across the damage. Moreover, the patterns for 650 nm luminescence under Ar^+ laser excitation and for 545 nm under 325 nm excitation also very similar. This could mean that excitation of NBOHCs with Ar^+ laser could be produced not directly but with the participation of E'_δ centers, or with defect which are closely associated with them.

The results also show a clear accumulation effect in E'_δ centers formation in the region of the void since the intensity of the 545 nm PL band (and equally 650 nm luminescence band under Ar^+ laser excitation) constantly increases on traces produced by a higher number of pulses.

Even more morphologically interesting zone appears by slightly increasing the pulse energy. Figure 6.7 shows a 2D spectroscopy maps produced by 20 pulses with an energy of E=1 μJ τ_p=150 fs, focused by NA_{eff}=0.4 objective. The importance of such traces was indicated in Chapter 5, where it has been emphasized, that regions of positive refractive index changes of higher contrast had been appearing confined between voids. On the PCM images it denoted as A; however, the usual region with index changes resembling type I traces are denoted as B. The 650 nm PL band under HeNe excitation, as well as the 650 nm and 545 nm PL bands under HeCd 325 nm excitation indicate the presence of NBOHCs and E'_δ centers respectively. Spectral maps show an inhomogeneous distribution of NBOHC everywhere in the region of modification. The E'_δ centers are distributed locally in the region of the void. The maximum of their PL yield is reached on the interface of the void. The E'_δ centers are also present in the regions of positive refractive index changes with higher contrast (region A) in a certain concentration. In the gray region B the E'_δ centers were not detected.

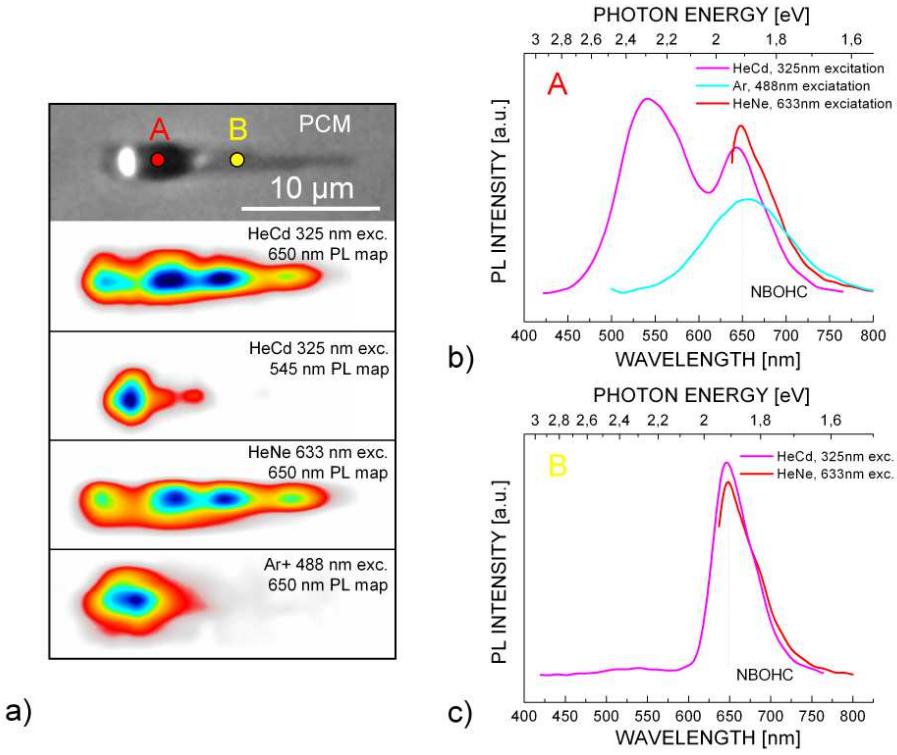

Figure 6.7: a) PCM image of static traces in fused silica irradiated by N=20 pulses with an energy of E=1 μJ focused by the NA$_{eff}$=0.4 objective, and the corresponding 2D spectral maps of different PL bands arising under 633, 488 and 325 nm excitation, notably the 545 nm and 650 nm PL bands. Typical PL spectra: b) spectra collected from the region looking white and dark black (denoted as A) on the PCM image of the trace. c) Spectra collected from the filament-like region looking gray (denoted as B) of the same trace under 633 and 325 nm excitation. PL signal from the 488 nm excitation is negligible and, thus, not shown.

6.5.2 High number of pulses. Type I and type II static traces

Usually engineering and photonic applications of femtosecond lasers in optical material involve repetitive irradiation of glass samples. Thus, a sufficiently high number of pulses is used to change the silica structure and its optical properties. This is determined by the ability to accumulate damage in order to make it possible to induce refractive index changes in the order of 10^{-2} by a high number of pulses arriving in single place. Systems working at repetition rates from kHz to MHz send from 10^3 to 10^6 pulses each second so the structure of the glass network determined by such amount of pulses could be greatly different from that one which is obtained after a relatively low amount of pulses. In addition, relaxation dynamics becomes an important factor for high repetition rates. However, for repetition rates used here (lower than 100 kHz) no visible heat accumulation was observed in fused silica.

Type I and type II static traces produced by the action of 5×10^4 pulses at 100 kHz was written to study effect of accumulation. 1.5 μJ pulses were focused by the NA_{eff}=0.3 objective. The choice of irradiation conditions is supported by the occurrence of type I/II transition in these circumstances induced just by changing pulse duration with the help of the compressor of the RegA 9000 amplifier. Surprisingly, the difference in pulse durations needed to produce either type I or type II traces is lower than 10 fs. It is important also that isotropic and birefringent traces are produced at the same pulse energy. PL spectra and the corresponding spectral maps are displayed in Figures 6.8 and 6.9.

Type I traces show strong luminescence at 650 nm under 325 and 633 nm excitations. The corresponding spectra presented in Fig. 6.8b were normalized to the 650 nm band maximum intensity. Such normalization clearly shows that the right wing of the 650 nm band coincides for all three excitation. Moreover, excitations with 633 and 325 nm reveal asymmetrical form of the spectral line as already reported in the literature [Sku01] for a resonant population of NBOHC defect level. On the contrary, upon Ar^+ laser excitation the 650 nm PL band has a symmetrical form that is an evidence of non-resonant population of this defect state from upper states.

The spectra under HeCd laser excitation are consisting almost from 650 nm luminescence and only a weak signal from the band centered at 545 nm is observed. However, under Ar^+ laser excitation, except of the 650 nm PL band, an intense luminescent band centered at 530 nm is present. The intensity of this band is distributed non uniformly across the trace; the intensity reaches its maximum values in the terminal left and right regions of the trace.

The spectroscopic investigation of type II traces provides completely dif-

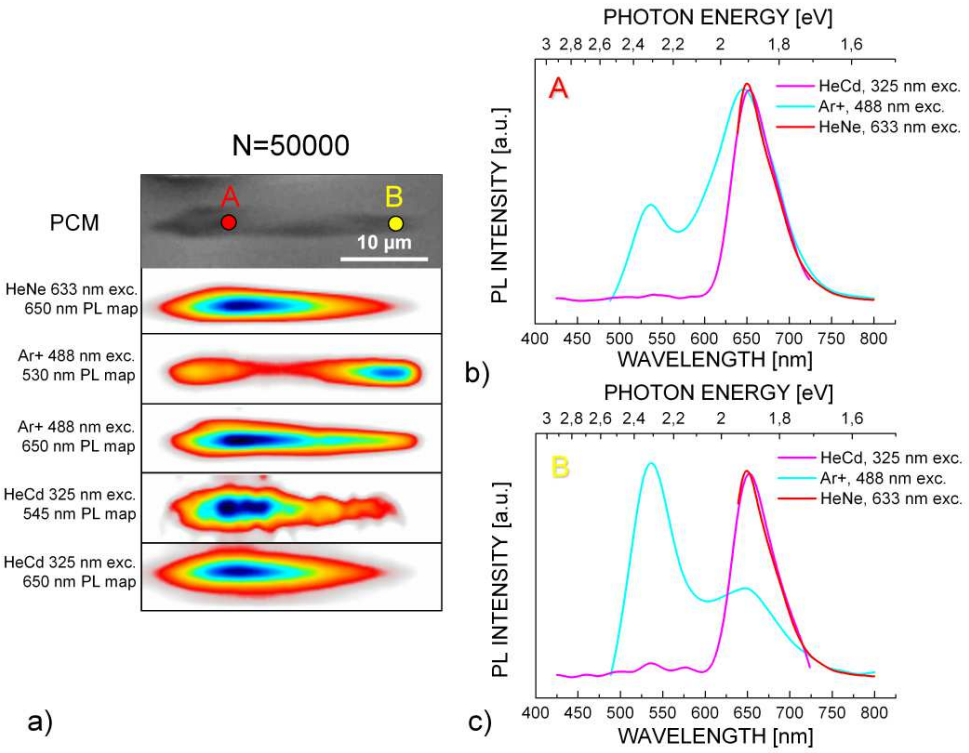

Figure 6.8: PL spectral maps measured for type I static multiple shot damage traces, produced by N=50000, E=1.5 μJ, τ_p=140 fs pulses focused by an NA_{eff}=0.3 objective. a) PCM image of the laser-induced modification and spectral maps of the associated PL bands for 633, 488 and 325 nm excitation, notably 530 and 650 nm bands. b) and c) Arbitrarily normalized PL spectra collected in the regions marked A and B on the PCM image, corresponded to the region of maximum of NBOHC signal and region of filament-like propagation respectively under 633 (red line), 488 (blue line) and 325 nm (magenta line) excitations.

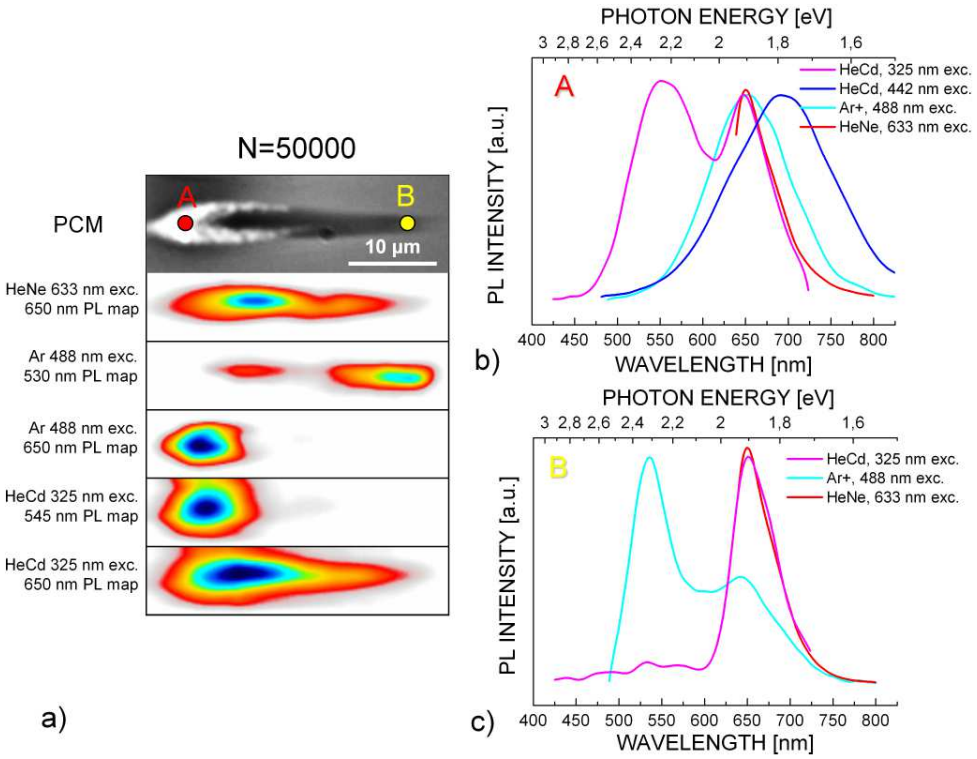

Figure 6.9: PL spectral maps measured for type II static multiple shot damage traces, produced by N=50000, E=1.5 μJ, τ_p=150 fs pulses focused by an NA_{eff}=0.3 objective. a) PCM image of the laser-induced modification and spectral maps of the associated PL bands for 633, 488 and 325 nm excitation, notably 530, 545 and 650 nm bands. b) and c) Arbitrary normalized PL spectra collected in the regions marked A and B on the PCM image, corresponded to the birefringent region and region of filament-like propagation respectively under 633 (red line), 488 (blue line), 442 (dark blue line) and 325 nm (magenta line) excitation sources.

ferent luminescent patterns. The birefringent region looking white in the PCM image shows a high PL signal of the 545 nm band upon UV excitation. A similar behavior and a spatial match was observed for the 650 nm luminescence band under excitation with Ar^+ laser (488 nm, not resonant with NBOHC), where its signal from birefringent region dominates the luminescence with respect to all the other different regions. However, it is not a region of maximum NBOHC generation. The last could be seen monitoring the 650 nm PL band maps resulting from resonant excitation of this defect state (with HeCd 325 nm and HeNe 633 nm wavelengths). This is located towards the right side of the birefringent area. This again indicates that the 650 nm PL band excited by Ar^+ laser involves intermediary (such as ODC) states via secondary down conversion to NBOHC.

The shape of the 650 nm band is disturbed by a certain modulation of its shape in the region of 670–825 nm, leading to broadening of the band. This modulation is placed closely to the cutoff of the notch filter at 700 nm, making the investigation of this region a rather difficult procedure. However, we believe that this complex luminescence could be assigned with the O_2^- interstitial molecules [FSS07]. In a more details this assignment will be considered later.

Particular attention should be deserved to the HeCd 442 nm (2.81 eV) excitation. Under its excitation only band centered at 690 nm (1.80 eV). Its spectral maps of the traces follow the same patterns as the ones detected for the 650 nm luminescence excited with the 488 nm excitation, indicating that the 690 nm luminescence can be equally attributed to the NBOHCs. The latters, however, have another environment causing the shift of the band position. Since Ar^+ and HeCd 442 nm excitations duplicate the information related to NBOHC centers, only the Ar^+ laser 488 nm excitation was used everywhere through the text in this PL study.

In the terminal right end of the type II trace (filament part) we find a region where a PL band centered at 530 nm excited by the 488 nm laser source exists. Comparing to type I trace which was written at the same energy conditions, the shapes and the absolute signal intensities of the 530 nm spectral band coincide.

To summarize, red luminescence corresponding to NBOHCs were detected everywhere in type I traces. In addition, weaker band centered at 530 nm appears at the periphery of the traces. The difference with type II traces is the strong PL signal observed in the birefringence region centered at 545 nm, corresponding to generation of E'_δ centers. By the presence of these defects one could equally explain the appearance of strong luminescence at 650 nm excited by Ar^+ laser at 488 nm. This is observed in the birefringent region, that indicates the presence of NBOHCs there. We note nevertheless that

these ones are not excited directly, so an energy transfer between different defects mechanism should be involved. Additionally, the shape of the 650 nm band excited at 488 nm in the birefringence and void regions of type II traces is disturbed indicating on the possible presence of O_2^- molecules.

6.6 Discussion

6.6.1 Resonant and indirect excitation of NBOHCs

Concerning optical activity of NBOHCs, this is expressed in the 1.9 eV (650 nm) band appearing upon different excitations. The question is are they directly excited or they follow a second order process. In those cases when excitation is going resonantly, such as with HeCd 325 nm and HeNe 633 nm laser sources, the PL band has an asymmetrical shape with FWHM=0.19 eV. On the contrary, if excitation occurs not directly, as for example with Ar^+ laser at 488 nm, it seems that third states, located upper in the forbidden band are playing a role and the NBOHCs serve only as markers revealing the presence of these (otherwise invisible) states. Symmetrical PL band centered at 1.9 eV (650 nm) with FWHM=0.27 eV, observed under 488 nm excitation is an argument in favor of this suggestion: since the population occurs not from the valence band, but from states located above, it is then possible to populate all possible sites of the NBOHC states and not the lowest ones.

As a possible intermediate states certain centers could be proposed. It could be already known centers like a neutral oxygen vacancy ODC(I) or divalent silicon ODC(II) but equally new ones. Considering ODC states, since no particular absorption band of ODC(I) placed near 2.54 eV was reported in the literature, this could be explained by the ODC specific configuration with a higher Si–Si distance [Sku98]. The ODC(II) is another candidate for such a state. It has an absorption band at 3.15 eV, so the excitation can happen along its wing. If these states have very long life-times (i.e., the relaxation from their triplet states can take place in approximately 10 ms) then the more probable transition should be not the luminescent transition to the valence band, but the nonradiative energy transfer to the NBOHC state located below.

6.6.2 NBOHC generation mechanism

It is important to connect the NBOHC generation to the dynamics of laser-generated carrier plasma. An example of free carrier dynamics for high energies femtosecond pulses is shown in Fig. 6.10a. We equally recall in

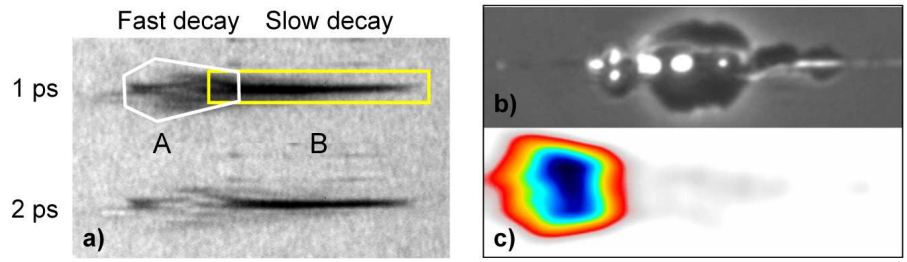

Figure 6.10: a) Time resolved OTM images of fused silica irradiated taken at 1 and 2 ps after irradiation (E=4.3 μJ, 150 fs, NA_{eff}=0.4). The images show strong electron absorption due to the generated free electrons. It allows to divide the zone of electron generation in two parts: A (white hexagon) with fast electron relaxation (<1 ps) and part B (yellow rectangle) with slow electron relaxation (∼100 ps), where permanent refractive index changes are taking place [Mau10]. For 30 μJ, 150 fs pulses b) PCM image of permanent refractive index changes and c) NBOHC generation map show a separation corresponding to the division in zones of fast and slow relaxation.

Fig. 6.10b,c the PCM image and the PL pattern observed for single shot damage traces produced by high energy pulses. Before the area of visible damage the NBOHC signal has a maximum value, however, no visible modification was observed there using the PCM method. This appears to be connected to electron plasma decay in fused silica, since such torch-like patterns were observed for time resolved 2D maps of free electron concentration during femtosecond irradiation of glass [Mau10]. The decay has two characterizing patterns: quite fast decay part (in a time <1 ps) denoted as A in Fig. 6.10a and a long living narrow core denoted as B. The fast dynamics is the usual behavior for fused silica exposed to relatively low fluencies [QGM+99]. In this case the electrons transferred into the conduction band have a fast relaxation dynamics going through trapping and the creation of STE states. The latters could be relaxed with the generation of NBOHC [SG93].

The fact that no permanent index structure appears in the region with NBOHCs (in fast relaxation region) leads us to conclusion that simple bond breaking could not drastically change the refractive index of the glass. Similar conclusion based on the calculations of the influence of defects on the electronic properties and refractive index of fused silica via a Kramers-Kronig mechanisms were obtained before [SB02, ZRG+06], where it has already been discussed that point defect formation does not explain refractive in-

dex changes.

Nevertheless, bond breaking occurred during NBOHC generation could be the primary step for permanent damage imprinting. This could happen in region B where the decrease of transmittance lasts at least one hundred of picoseconds. In the high energetic regime studied here, the hot laser-induced electronic bath alters the overall capacity of the fused silica network to participate in the free carrier relaxation because of a strong structural changes in material [CXW05]. These modifications will be studied later in the chapter concerning Raman spectroscopy.

6.6.3 The origin of the 545 nm PL band

The origins of the PL band centered near 530 nm (2.34 eV) excited at 488 nm by the Ar^+ laser (488 nm) and of the PL band centered near 545 nm (2.27 eV) under HeCd laser excitation at 325 nm remain unclear. The 545 nm luminescence was reported at numerous occasions in femtosecond, picosecond and nanosecond laser irradiated fused silica samples [WJS+99, KD03]. Despite the fact that the assignment of this band to specific defect topology is still uncertain, it could be attributed with a certain likelihood to oxygen-deficiency related centers, particularly to E'_δ-centers. The main argument for this assignment follows from Nishikawa *et al.* results [NWI+96], where the authors observed the PL signal at 545 nm to be proportional to the EPR signal from E'_δ centers. Since the PL band has approximately the same halfwidth $\hbar\Delta\omega$=0.44 eV in all the studies cited above [NWI+96, KD03], this suggests the same origin of the band.

The similar band at approximately 550 nm was equally detected in cathodoluminescence experiments [FBT+02]. This band is particularly intense in Si-implanted fused silica samples, indicating that 545 nm band is definitely related to oxygen deficiency.

Watanabe *et al.* [WJS+99] observed the band centered at 2.21 eV (560 nm) with FWHM=0.21 eV on the surface of femtosecond irradiated fused silica. The damage sites were produced under tight focusing conditions and the luminescence was collected from the region of the microexplosions. Authors assigned the defect state correponding to this PL band to a pair of neutral oxygen vacancy and molecular oxygen, $(V_O; O_2)$; however, they equally propose that this luminescence could be attributed to E'_δ-centers. It is known that the precursor for E'_δ centers is ODC(II) [GF86], which has an absorption band centered at 5 eV. It was shown that the 560 nm luminescence band could be observed by direct excitation via this precursor band. Therefore, we assume that this band can be closely related to ODC centers and to the 545 nm band observed in our experiment.

6.6.4 The origin of the 530 nm PL band

The 530 nm (2.34 eV) PL band appearing under excitation of Ar^+ laser was observed previously in the femtosecond modified fused silica glass [CHRK03, Rei06, RKS+06]. This PL was observed in type I traces, that is consistent with our observation displayed in Fig. 6.8. Except of the equal writing conditions, the similarity of bands was found both on the exact band position, and its width, which was measured to be 0.25 eV at room temperature. In addition, a similar band appears after neutron- [STI96] and gamma-irradiation of fused silica [SN99].

In our study the 530 nm PL band was observed for both "wet" and "dry" silica samples, therefore a connection of this band to H and OH impurities is not probable. In the different studies mentioned above, this band was attributed to E'_δ centers [RKS+06, RCS+07] or other oxygen-deficiency-related centers. We doubt, nevertheless, that this band is due to E'_δ centers, since the halfwidth of the band, its maximum position, and the excitation source do not correspond to the ones declared in the original paper [NWI+96]. Additionally, in the present work, luminescence at 530 nm was observed only in silica exposed to a high number of pulses. This indicates that this point defect is not typical for pristine fused silica, but needs special environments, which are presented in the network of densified silica. These defects could be equally connected to certain specific configurations of ODCs or to oxygen excess centers [SN99]. Having not enough data to precise their origin, we will use the term "laser induced defects" (LID) as notation.

6.6.5 Spatial Si/O ions separation effect

An important fundamental problem which we will take into consideration is the liberation of oxygen with its following migration. This phenomenon leads to a spatial ion separation effect, which was reported previously both in the regions of the voids and in the birefringent regions. For example, Shimotsuma [SKQH03] observed regions of oxygen deficit in the layers of lower refractive index in the nanogratings zones. On the other hand, the presence of molecular oxygen was put forward in the voids region [WJS+99, CLC+11] in tight focusing conditions and finally observed in germanium GeO_2 glass [BdLG+11].

A mechanism for spatial ions separation was firstly proposed in [WJS+99], where it was related to the development of atomic oxygen O according to Eq. 2.2. The intermediate step is the generation of interstitial molecular oxygen O_2, that could happen in strong fields, when the concentration of atomic oxygen formed in reaction of STE relaxation becomes high enough

so that individual atoms can react with each other to form O_2. Molecular oxygen has high enough mobility and low chemical reactivity to leave the region of its generation [WJS+99, CLC+11]. If the temperature in the region of interaction is high enough then the oxygen can diffuse up to tens of nanometers from the region of generation before resolidification of the glass (as shown in Chapter 2).

Thus, the effect of ions separation can be studied by monitoring both the dynamics of ODCs and of molecules of oxygen or other oxygen excess centers.

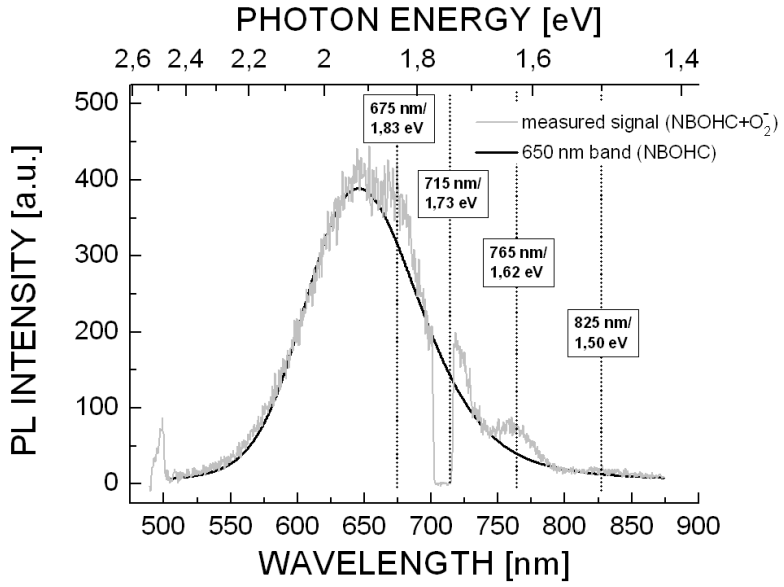

Figure 6.11: Typical PL spectrum measured for type II longitudinal traces reveals complex composition of the 650 nm band upon Ar^+ excitation at 488 nm. It is composed with peak centered at 650 nm and related to luminescence of NBOHCS (black curve) and of a certain modulation in the 675–825 nm spectral region related to multimodal luminescence of O_2^- centers.

We start the study of ion separation from the observation of luminescence signatures of oxygen molecules. We detected the presence of the O_2^- ions in the region of birefringence in the traces written in type II regime and equally in the regions of the voids. The luminescence pattern of O_2^- centers of a complex structure was recorded upon Ar^+ excitation at 488 nm. On the spectra the PL appears as a several weak bands placed at 675 nm (1.83 eV), 715 nm (1.73 eV), 765 nm (1.62 eV), and 825 nm (1.50 eV). Since they are

overlapping with NBOHC band the PL peak at 650 nm becomes wider (with FWHM=0.31 instead of FWHM=0.27 eV of the single NBOHCs).

The almost equidistant placement of these bands with the distance of 0.11 eV indicates the vibrionic structure of the defects and corresponds to the value reported for molecular oxygen in negative-ion state O_2^- [RLK61, BS70]. In addition, the peak positions perfectly match the values of the PL reported for O_2^- ions generated in the oxygen-implanted silica layers [FSS07]. Being bonded to one Si in the glass matrix it can create a peroxy radical O_2^-, which was detected in neutron irradiated oxygen rich silica by EPR means [FGSW79].

Considering oxygen deficiency-related defects, we can extract certain information from the distribution of E_δ' centers. We equally have observed this centers in the regions of the voids and in the birefringence regions in the multiple shot traces. Summarizing these observations with the observation of molecular oxygen in the same regions, we can conclude that the separation of ions indeed takes place there. The separation occurs according to the proposed scenario, leaving charged vacancy $\equiv Si\cdot^{+}Si\equiv$ with the luminescence signatures of E_δ' centers. Thus it supports the idea that these centers are the clusters of only two silicon atoms.

Taking into account these findings, the development of birefringence region can be considered as following. We firstly point out on an interesting dynamics which NBOHCs show in the white region as indicated in Fig. 6.6. After the first shot the NBOHC yield is very low if one compares it with the positive refractive index changes region. On the contrary, the 545 nm band is present. This is in agreement with results of Watanabe [WJS+99] where NBOHCs were not detected in the region of void. We believe that an ion separation effect according to the above proposed scenario occurs here. The ions separation is particularly important in the strong fields. And if, during the first pulse interaction, strong field could be obtained due to self-focusing effect, the void formation opens another possibility to achieve strong fields in the interaction region. Indeed, in the lower refractive index region a local field enhancement occurs. Thus, when the void or another hollow region is formed, further oxygen diffusion in its vicinity becomes favorable as the next pulses arrive. On the other side, those oxygen molecule that moves away from the hollow region could be destructed under the subsequent action of femtosecond laser pulses. Then NBOHC can be formed in the white zone.

We recall that in positive RIC zone the mechanism of generation and accumulation of NBOHCs is different. NBOHCs are formed there after bond breaking when STEs relax. Thus, if after the first pulse NBOHC presents mainly in the positive RIC zone, after the action of 32–64 pulses, the PL signals from these regions are almost equal.

The questions remains on, how the excitation of the 545 nm band occurs, since no intrinsic absorption band was reported for E'_δ centers in the literature. On the contrary, it was reported the existence of numerous absorption bands related to certain oxygen excess centers near 3.8–4.8 eV [NTO+89, Gri91, Sku98], including the absorption band of O_2^- [Rol79] (there is equally a band at 3.8 eV assigned to CL_2 molecules [AKM+91] but we reject any influence of chlorine for two reasons: our irradiated silica samples contain a low content of these impurities; equal spectral patterns were observed in "wet" and "dry" silica samples, characterized by different amount of Cl impurities). Thereby, efficient excitation of the 545 nm band in the region of nanogratings and in the vicinity of void (regions of oxygen migration) could be possible via the 3.8 eV absorption band connected with oxygen-excess centers.

6.6.6 Role of the E'_δ centers in densification

The 545 nm (2.27 eV) band characterizing E'_δ centers was detected in various regions of modification under different irradiation conditions. These may be related to locations in the vicinity of the voids (Fig. 6.4), region of positive refractive index changes for high energy single pulse irradiation (Fig. 6.5), regions of positive refractive index changes induced by a low number of pulses (Fig. 6.7) and type II modification regions (Fig. 6.9). That is why it is hard to point out the profound processes triggering the generation of this defects, since they are produced under various conditions. Nevertheless, the presence of these defects could indicate densification. Theoretical calculations of the structures of these defects shows that they are stable for a Si–O bonding length $r<1.62$ Å [SMM+05]. For higher values of the interbonding length (that means the packing of the material will be lower in this case) E' centers will be more stable species. The latter defect has different spectroscopic signatures and cannot be detected using our excitation wavelengths. However, it presence was confirmed by EPR studies [SG93, DMSH96].

Thereby, the different types of positive refractive index changes (high and low contrast) demonstrated in Fig. 6.7 and induced in the same trace by irradiation of silica with 20 pulses may be interpreted in the following way. They are distinguished not only by their contrast on the PCM images, but also by the corresponding defects distribution present on the spectral maps in Fig. 6.7a. If in the regions of higher contrast denoted as A, a certain presence of E'_δ centers was detected everywhere, in the gray region of lower positive RIC denoted as B, the latter were not detected. One should state again that the presence of these defects only plays a role of indicator, but nothing could be said about the mechanism causing their appearance.

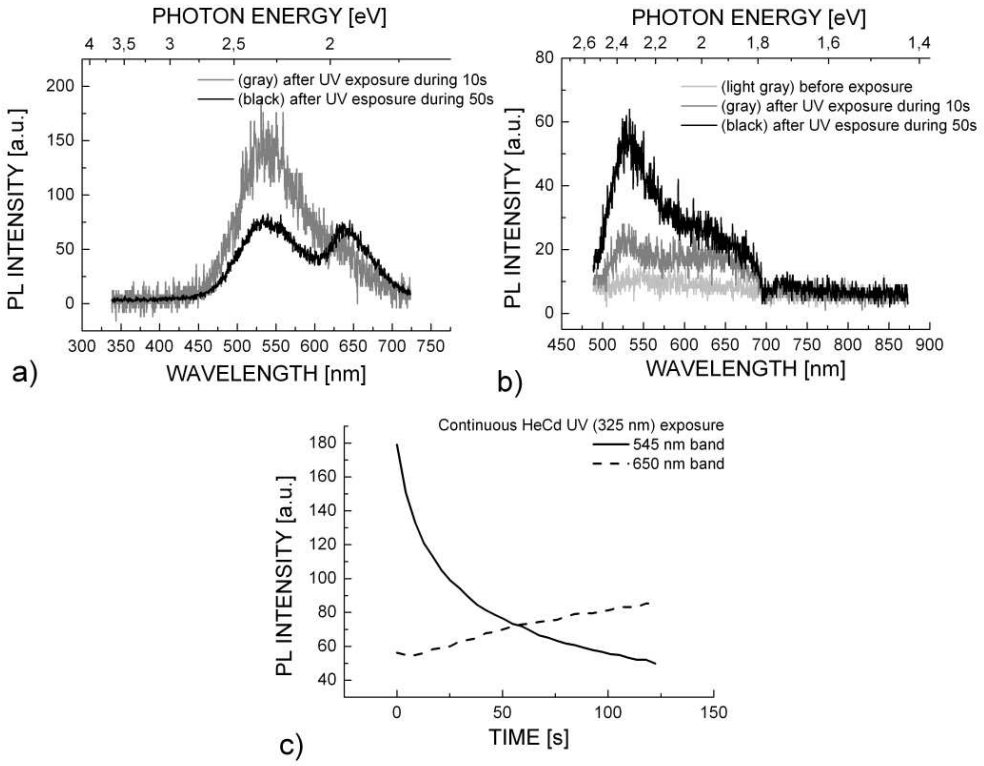

Figure 6.12: UV activation effect observed in laser pre-written type I waveguides. a) After their first disappearance with time the NBOHC defects could be reactivated with HeCd 325nm UV laser. b) Ar^+ excitation spectra shows that simultaneously with NBOHC, the 530 nm band increases. c) NBOHC signal is increasing during UV exposure while the 545 nm band is decreasing.

6.7 Defect evolution and transformation effects

Another phenomenon, which could be used for further structural assignment of unknown observed PL bands to certain defects, is photoluminescence bleaching and further luminescence activation by HeCd UV laser at 325 nm. This was observed in the type I longitudinal traces in scanning regime of writing. Usually right after photoinscribing the traces, strong PL of NBOHC is observed which lasts only several hours. Later the corresponding PL excited with HeNe and Ar^+ laser sources disappears completely. If, nevertheless, we re-excite the same laser-affectde region with HeCd 325 nm UV light, the band

centered at 545 nm (2.3 eV) with FWHM 0.45 eV is observed. We assigne this band to E'_δ centers reported previously.

Under subsequent continuous action of UV light, however, this band is bleaching and the 650 nm PL band become visible again. Additionally the 530 nm (2.34 eV) band excited under Ar^+ laser and the 1.9 eV (650 nm) bands under Ar^+ and HeNe laser excitation appear again. This process is illustrated in Fig. 6.12a. The PL spectra was recorded under HeCd excitation upon the exposure of the same laser with a power of 100 μW during 10 and 50 s. We secondly recheck the region with Ar^+ radiation (488 nm). The corresponding changes in the PL spectra observed upon Ar^+ laser excitation before and after HeCd UV laser exposure with the same power are illustrated in Fig. 6.12b. An increase of the 530 nm band with a certain increase of the 650 nm band is evident.

Several important observations should be mentioned here. After UV activation, the NBOHC signal was observed under both HeCd and HeNe resonance excitation, though it was not observed before under these resonant sources of excitation. Taking into account these facts we assume that the NBOHC was regenerated by photochemical transformations. The second observation is that the 545 nm PL band at HeCd excitation and the 530 nm PL band at Ar^+ excitation show different dynamics. While the first one decreases with UV dose, the second goes up. This confirms our previous suggestion that these two bands are associated with different defects.

One should notice that in dynamic and static type II and static type I traces, no similar defects transformation processes were observed. Defects are simply photobleached upon HeCd UV, Ar^+, and HeNe laser sources exposure (without their further reactivation). Having not enough data to accurately determine this phenomenon, we could only speculate on probable defect transformations. These could be structural changes of silica network or changing of electronic properties of silica.

For structural changes the probable mechanism which could be proposed is the photo-dissociation of some oxygen-excess centers, like interstitial ozone molecules, peroxy linkages or peroxy-radicals. According to Eqs. 2.2, 2.5, 2.6, each reaction can produce NBOHC and interstitial atomic or molecular oxygen. During their diffusion, they could interact with the network or defects, including interaction with oxygen-deficiency type centers according to the reaction:

$$\equiv\text{Si–Si}\equiv + \text{O} \rightarrow \equiv\text{Si–O–Si}\equiv \quad \equiv\text{Si}\cdot + \text{O} \rightarrow \equiv\text{Si–O}\cdot$$

This mechanism explains how oxygen excess centers can be produced with the decrease of ODC at the same time. Further application of this model, however, faces difficulties. Having no information of all defects playing a role

in the interaction it is hard to explain the dynamics of the increase of NBOHC and the decrease of E'_δ centers, since the second one happens much faster. Secondly, the origin of the 530 nm band remains unclear. However, in such proposition it will be most likely connected to some oxygen excess-centers: produced either as a result of initial oxygen-excess centers photo-dissociation or after interstitial oxygen reaction with the network.

The second explanation is based on the electronic changes in the defect structure. One can take into account electron migration involving oxygen-vacancy clusters according to the following reaction:

$$\equiv\text{Si–Si}\equiv \leftrightarrow \equiv\text{Si}\cdot^{+}\text{Si}\equiv + e^{-},$$

Initially, right after the writing, neutral oxygen vacancy and NBOHC are appearing so 530 nm and 650 nm PL can be associated with them. However, it could be more energetically advantageous for the electron to migrate to non-bridging oxygens (NBO), forming negatively charged NBO^{-} and positively charged oxygen vacancy (which is E'_δ):

$$\equiv\text{Si–O}\cdot + e^{-} \rightarrow \equiv\text{Si–O}^{-}.$$

NBO^{-} centers are stable in sodium doped glasses, where they have different spectral properties [Tru86], particularly no absorption at 2.0 eV and the characteristic PL at 650 nm are observed. Photoluminescence at 545 nm appears as the result of generation of a positively charged oxygen vacancy.

Under UV exposure NBO^{-} centers could be destroyed, turning the system to initial configuration so the 530 nm and 650 nm PL bands appears again. Reactions at UV activation could be presented then as follows

$$\equiv\text{Si–O}^{-} + \hbar\omega \rightarrow \equiv\text{Si–O}\cdot + e^{-},$$
$$\equiv\text{Si}\cdot^{+}\text{Si}\equiv + e^{-} \rightarrow \equiv\text{Si–Si}\equiv.$$

The structural model of the defect causing 530 nm luminescence will be neutral oxygen vacancy in this case; however, with specific atomic structure with higher Si–Si distance.

6.8 Conclusions

We have studied various types of defects generated by femtosecond laser pulses inside fused silica in the conditions where local index changes can be positive or negative and even modulated on the nanoscale. Only resonant excitation of each type of defects provides a trustful information about its distribution in the modified region. Using light from HeNe laser with a wavelength of 633 nm, Ar ion laser at 488 nm and HeCd laser with a wavelength of

Table 6.1: Qualitative description of defects observed in different zones of produced modification.

Type of modification	NBOHC	E'_δ	LID
Precursor zone, $\Delta n \sim 0$	Yes		
Single pulse, $\Delta n > 0$	Yes		
Type I (after writing)	Yes	Few	Yes
Type I (bleached)		Yes	
High contrast $\Delta n > 0$	Yes	Yes	
Void, $\Delta n < 0$	Few	Yes	
Birefringence, $\Delta n < 0$	Yes	Yes	

325 nm as such excitation sources, the spatial distribution maps of NBOHCs and ODCs for different traces were plotted. Qualitatively they are presented in the Table 6.1

The maximum of NBOHC signal was observed in the region that had no visible permanent index changes produced under low energy density of incident irradiation. This behavior is explained by fast bond breaking after STE relaxation. Concerning the concentration of breaking bonds, it is several times higher in this region than in the adjacent area of visible permanent modifications. In the region of bond breaking no significant refractive index changes was observed, and the hypotheses of a direct index variation via the changes in electronic properties of defects does not find a support. These region, however, can be considered as a precursor of densification, since the breaking bonds could act as nucleation clusters for structural rearrangements with effect in local densities. This subject will be studied in details in the next chapter.

The 545 nm band was assigned to E'_δ centers. It was observed in the region of void for single shot damage and in the birefringent region for type II multiple shot damages. That confirms the hypotheses that E'_δ center is oxygen vacancy centers formed after bridging oxygen dissociation. Moreover, presence of E'_δ centers was detected in the positive refractive index of higher contrast. That is why these defects could be considered as an additional factor indicating the densification.

The 650 nm band excited at 488 nm in the region of void and in the birefringence region of type II traces revels a complex structure, indicating on a possible presence of O_2^- molecules. Thus the ions separation effect suggested to take place in these region has a strong evidence.

The 530 nm band was observed in type I and in the filamentation part of type II static multiple shot damages; however, the assignment of this band to specific defects remains unclear.

Type I traces show fast natural photobleaching of defects, but this tendency could be inversed by UV exposure of modified regions. The observed results indicate a close connections between E'_δ having luminescence at 545 nm and oxygen deficiency-related centers characterized by the 530 nm PL band.

Chapter 7

Raman spectroscopy

Raman spectroscopy is widely used for investigating the structure of solids and equally in the analysis of liquids and gases [Nak09]. Based on the Raman scattering effect, it allows to measure the vibrational spectra of solids and molecules. That makes this method very powerful in studying the microscopic and molecular structure of solids in the context of the present work. Since vibration modes correspond to certain arrangements of the fused silica structure, the observed changes in the recorded spectra could be directly assigned to specific network rearrangements. This particular fact permits the use of this method for further understanding the effects of femtosecond laser irradiation on the fused silica structure.

7.1 Fundamentals of Raman scattering

Raman scattering is the inelastic scattering of light on molecules (hereafter the term molecule can also represent an atom in the network). The scattered light acquires frequency shifts with respect to the incident light as the luminous energy couples with the energy of the molecule. In this case, one observes on the spectra of the scattered light weak satellite lines placed symmetrically with respect to the incident frequency. The spectral displacement of the satellites does not depend on the incident light wavelength, but depends on the media, since it is determined by its vibrational spectra.

In a first approximation, the energy of electrons in a molecular system can be presented as a sum of electronic, vibrational and rotational energies. Direct transition between corresponding levels could be performed by photon absorption if its energy matches the difference between two levels. For vibrational transitions this is possible only with infrared and far-infrared light (thus, applied in infrared absorption spectroscopy). However, such transi-

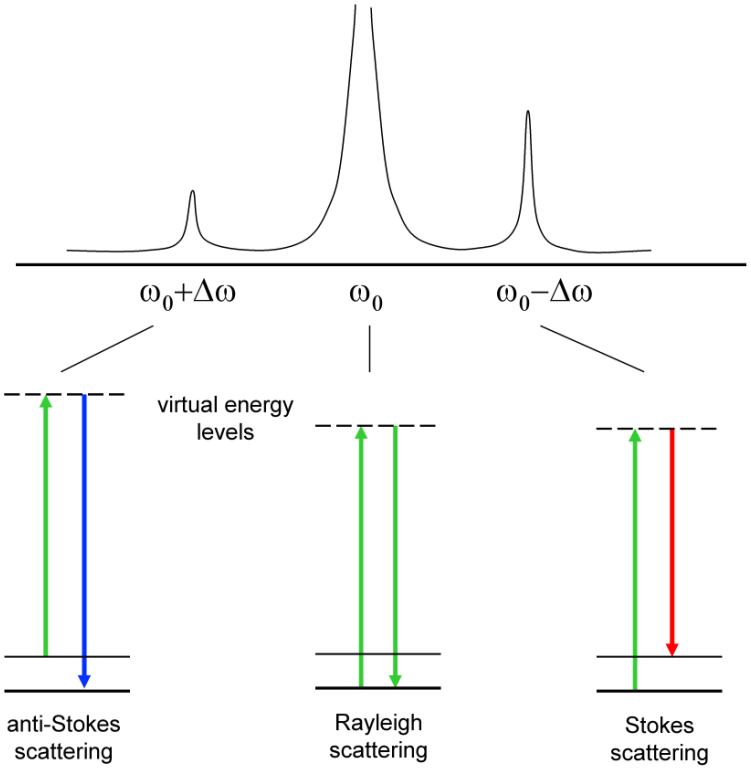

Figure 7.1: Elastic and inelastic scattering of light.

tions could be induced by visible light indirectly. The process is schematically illustrated in Fig. 7.1, showing the elastic and inelastic scattering processes on molecular system. On the electronic levels diagram one can suggest that the transition occurs through a virtual level and involves the annihilation of the incident photon with the creation of the second, emitting, one. In this case, if the initial energy of a molecule was E_i and it was transferred to $E_f = E_i + \hbar\Delta\omega$, then the frequency of scattered light should change to the value $\omega - \Delta\omega$ to fulfill energy conservation laws. The transition of the molecule to lower energy is also possible, however the corresponding line will be less intense, because of the lower population of higher vibrational levels. Red-shifted satellite lines are called Stokes components, and blue-shifted – anti-Stokes components. Light scattered at the same frequency corresponds to elastic Rayleigh scattering.

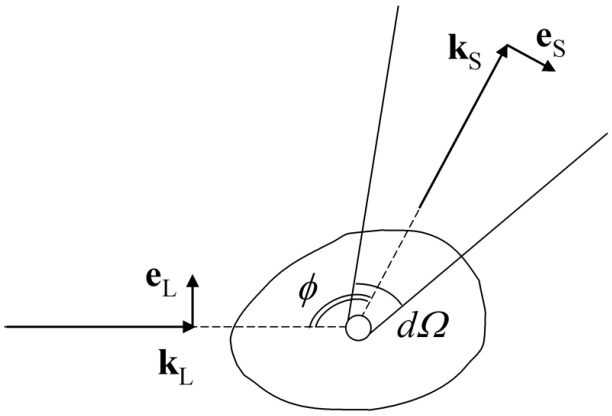

Figure 7.2: Schematic representation of light scattering.

7.2 Classical approach of Raman scattering

Raman scattering can be considered using a classical approach [CG83, Car82, Lin87]. Incident radiation induces scattering light emitting in certain direction as displayed in Fig. 7.2. The radiation energy emitted per time unit by an electric dipole $\mathbf{p}$ vibrating at frequency ω_v in this direction is given by formula [LL75]:

$$\frac{dI_S}{d\Omega} = \frac{\omega_v^4}{32\pi\varepsilon_0 c^3} \left|\mathbf{e}_S \cdot \mathbf{p}\right|^2, \tag{7.1}$$

where $d\Omega$ is the element of solid angle, c the speed of light in the medium and $\mathbf{e}_S$ the unit vector representing the polarization of the scattered light in the direction of observation. As it was discussed before, the optical properties of solids could be defined by the tensor of electronic polarizabilities α of the ions, composing the medium. The scattering signal is defined by the induced electric dipole moment:

$$\mathbf{p} = \alpha \cdot E\mathbf{e}_L, \tag{7.2}$$

where $E = E_0 \cos(\omega_0 t)$ is the electric field of the incident monochromatic wave and $\mathbf{e}_L$ represents the polarization of the incident light.

Differential scattering cross-section $d\sigma/d\Omega$ is obtained dividing the Eq. 7.1 by the energy incident per unit area and time unit $I_L = c\varepsilon_0 E_0^2/2$. After inserting 7.2 into 7.1, we obtain:

$$\frac{d\sigma}{d\Omega} = \frac{\omega_0^4}{(4\pi\varepsilon_0)^2 c^4} \left|\mathbf{e}_S \cdot \alpha \cdot \mathbf{e}_L\right|^2. \tag{7.3}$$

Note that, under the influence of adjacent electrons and nuclei, electronic shells will be disturbed. This makes α to be depended on the coordinates of

the atoms. As long as ω_0 is far from any resonances, α can be expanded in a Taylor series as a function of normal coordinates q_n of the nuclei displacements. Considering only first term of the series which represents one-phonon processes, the formula reads as

$$\alpha(q) = \alpha(0) + \sum_{n=1}^{Q} \left.\frac{\partial \alpha}{\partial q_n}\right|_{q_n=0} q_n, \tag{7.4}$$

where partial derivatives are taken at the equilibrium point $q_n = 0$, Q is the number of normal vibrational modes for N nuclei. Assuming that the atomic displacements are small, vibrations will be going according to the harmonic law:

$$q_n(t) = q_{n0} \cos(\omega_n t). \tag{7.5}$$

Inserting equations 7.4 and 7.5 into 7.2 give the following relation for the dipole moment:

$$\mathbf{p} = \alpha_0 \cdot \mathbf{e}_L E_0 \cos(\omega_0 t) + \frac{1}{2} E_0 \sum_{n=1}^{Q} \frac{\partial \alpha}{\partial q_n} \cdot \mathbf{e}_L q_n \left[\cos(\omega_0 + \omega_n)t + \cos(\omega_0 - \omega_n)t\right]. \tag{7.6}$$

The first term of this relation is responsible for elastic scattering (that is scattering with no wavelength shift), which is also called Rayleigh scattering. If the media is isotropic, then polarizability could be presented as a scalar $\bar{\alpha}$. For differential cross-sections of elastic scattering from Eqs. 7.3 and 7.6 we will obtain

$$\frac{d\sigma}{d\Omega} = \frac{\omega_0^4 \bar{\alpha}_0^2}{(4\pi\varepsilon_0)^2 c^4} \left|\mathbf{e}_S \cdot \mathbf{e}_L\right|^2. \tag{7.7}$$

Introducing the angle ϕ between the direction of incidence and the direction of observation, the previous equation takes the following form:

$$\frac{d\sigma}{d\Omega} = \frac{\omega_0^4 \bar{\alpha}_0^2}{2(4\pi\varepsilon_0)^2 c^4} \left(1 + \cos^2\phi\right). \tag{7.8}$$

The second term of Eq. 7.6 shows the generation of light with the sum and the difference frequencies of the induced light and normal vibrations. These represent the anti-Stokes ($\omega_0 + \omega_n$) and Stokes ($\omega_0 - \omega_n$) components of Raman scattering. Corresponding cross-sections for Stokes and anti-Stokes Raman lines should be proportional to $\langle q_n^2 \rangle$ [Car82] which is the thermal average of the displacement of all phonons. To separate each component one should take into account the contribution of the corresponding transitions to the total vibrational energy of the n_{th} vibrational state. This is determined by

Bose-Einstein distribution. Finally, one can find the following expressions for the Stokes and anti-Stokes components:

$$\frac{d\sigma_s}{d\Omega} = \frac{\hbar(\omega_0 - \omega_n)^4}{2(4\pi\varepsilon_0)^2\omega_n c^4}[n(\omega_n, T) + 1] \left| \mathbf{e}_S \cdot \frac{\partial\alpha}{\partial q_n} \cdot \mathbf{e}_L \right|^2 \text{ Stokes}, \tag{7.9}$$

$$\frac{d\sigma_a}{d\Omega} = \frac{\hbar(\omega_0 + \omega_n)^4}{2(4\pi\varepsilon_0)^2\omega_n c^4} n(\omega_n, T) \left| \mathbf{e}_S \cdot \frac{\partial\alpha}{\partial q_n} \cdot \mathbf{e}_L \right|^2 \text{ anti-Stokes}, \tag{7.10}$$

where $n(\omega_n, T) = [\exp(\hbar\omega_n/kT) - 1]^{-1}$ is the Bose-Einstein statistical factor.

To observe the n_{th} vibrational mode in the Raman scattering the given cross-sections should be non zero, so the following relations should be fulfilled:

$$\frac{\partial\alpha_{ij}}{\partial q_n} \neq 0 \tag{7.11}$$

Thus, the vibration is non Raman active unless electronic polarizability changes as the nuclei are displaced. In crystals, in addition to the Eq. 7.11, more strict momentum selection rules take place; however, in gases, liquids, and amorphous materials these rules are broken because of the lack of the translational symmetry.

It should be noted that the obtained formulas characterize only individual scattering centers. To obtain scattering cross-sections from a medium, a volume integration of the contributing single scattering centers should be performed, taking into account inhomogeneities existing in the media (for example, due to thermal fluctuations). This procedure can be found in [Lin87]. The dependencies of the scattering cross-sections on the polarizability of the material, the frequency of the incident light and the angular distribution of scattering light, nevertheless, are the same as in Eqs. 7.8, 7.10.

7.3 Interpretation of Raman spectra

The phonon density of states, that is the number of vibrational states per interval of energy, is crucial in determining the vibrations in solid state physics. It is determined by the structure and the chemical composition of the material. The use of phonon density of state in Raman spectroscopy is principally important, as the Raman signal depends proportionally on this quantity. For light scattering, the measured signal is proportional to the Fourier components of the space-time perturbation of the dielectric tensor $\varepsilon(\mathbf{r}, t)$. Shucker & Gammon [SG70] and then Galeener & Sen [GS78] presented calculations of the dielectric correlation function in glasses leading to first-order Raman

scattering cross-section calculated in terms of phonon's density of states. The Stokes component is given by the relation:

$$I(\omega) = C(\omega)\frac{(\omega_0 - \omega)^4}{\omega}[n(\omega, T) + 1]g(\omega), \tag{7.12}$$

where $C(\omega)$ is the Raman coupling coefficient depending on the polarizations of the incident and scattered photons. It can be seen that the measured scattered signal depends also on parameters which could changes from experiment to experiment, such as the temperature of the sample or the wavelength of the laser. That is why one can use the reduced Raman spectrum given by:

$$I_{red}(\omega) = \frac{I(\omega)\omega}{(\omega_0 - \omega)^4[n(\omega, T) + 1]} \sim C(\omega)g(\omega). \tag{7.13}$$

As seen from these formulas, both Raman and reduced Raman spectra depend on the Raman coupling coefficient and the phonon density of state function. $C(\omega)$ has a complex behavior with respect to ω and could vary with the changes in the structure of the glass. Nevertheless, observed Raman spectra are defined to a greater extent by $g(\omega)$ which can be calculated. Thus the Raman bands can be assigned to specific vibration of the fused silica network. An brief overview of certain proposed models defining $g(\omega)$ function is given below.

7.3.1 Assignment of observed Raman bands

Most of the Raman studies in fused silica consider band assignments which are generally described either in terms of normal vibrations of bridging SiO_2 units (represented in Fig. 7.3a) or of SiO_4 tetrahedra. In silica melts and multicomponent glasses where the concentration of non-bridging oxygen is usually high, one considers the movements of tetrahedral SiO_4 groups in various states of polymerization (Q_n units, SiO_4 tetrahedra with n bridging oxygens). In the case of polymerized silica networks, generally, near-neighbor central-force model (NN-CF) [ST77] is considered, which allows to predict the positions of the main bands [Gal79]. The main statements of this model are given below.

Sen & Thorpe [ST77] assumed that the vibrations of the silica network can be described using SiO_2 units with only one force constant k defined by the Si–O bond. The following normal vibrational frequencies for such a system were deduced:

$$\omega_1^2 = \frac{k}{m}(1 + \cos\theta), \omega_2^2 = \frac{k}{m}(1 - \cos\theta), \tag{7.14}$$

$$\omega_3^2 = \omega_1^2 + \frac{4k}{3M}, \omega_4^2 = \omega_2^2 + \frac{4k}{3M}, \tag{7.15}$$

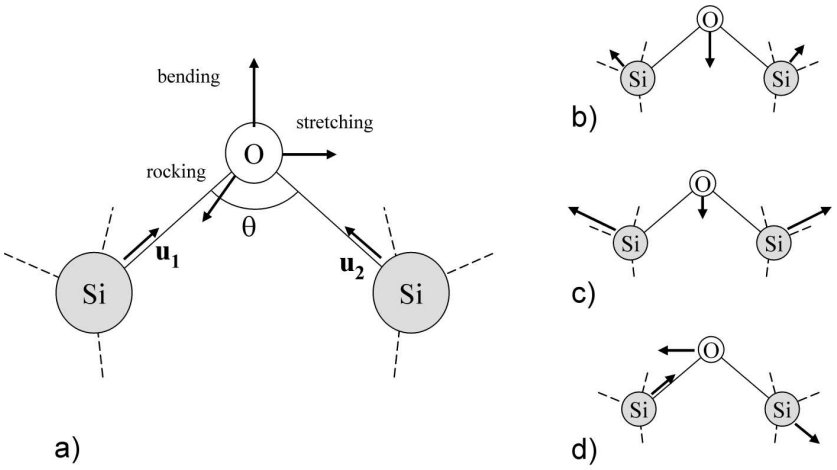

Figure 7.3: a) The SiO_2 unit, considered for normal vibrations characterization in fused silica and its b) bending, c) "cage", and d) stretching motion of SiO_2 units corresponding to vibrations at 440, 800 and 1064/1200 cm^{-1}.

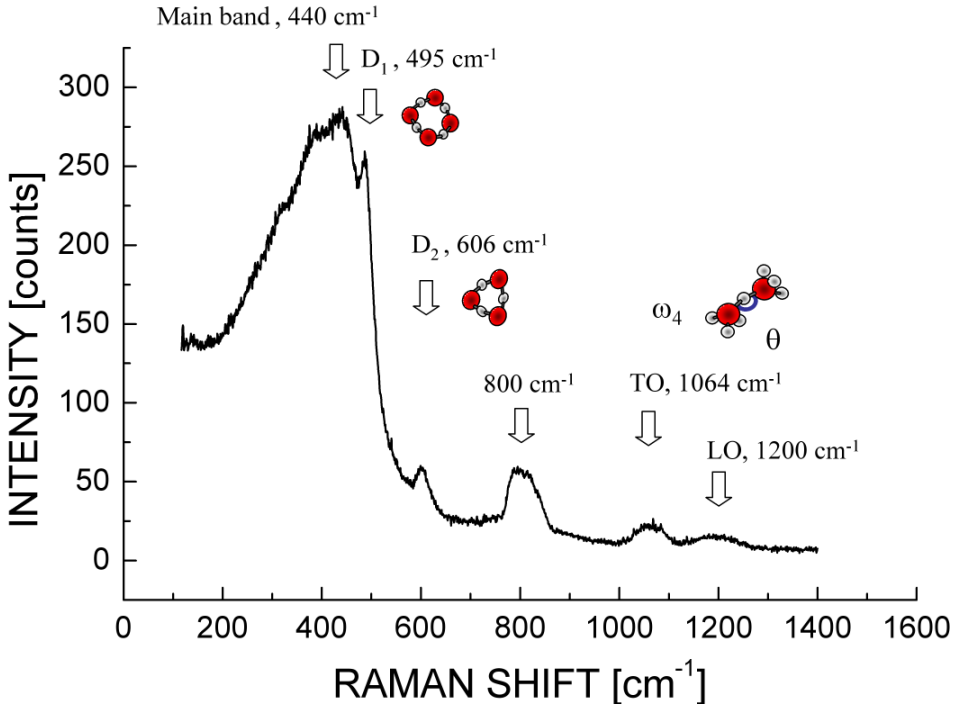

Figure 7.4: Raman spectrum of the pristine fused silica glass.

where m is the mass of oxygen and M is the mass of silicon. The equations given above show the positions of the vibrational bands as a function of interbonding angle, since nearest-neighbor force increases with the growth of θ. Differentiating left and right parts of Eqs. 7.15 leads to

$$\Delta\omega_i = \pm\frac{k}{2m}\frac{\sin\theta\Delta\theta}{\omega_i}, \tag{7.16}$$

which expresses the shifts of the vibrational bands as a function of the changes in the interbonding angle, $\Delta\theta$.

The NN-CF model, however, can be applied only if the coupling among adjacent tetrahedra is sufficient (otherwise the representation of SiO_4 tetrahedra vibrations should be used). This happens when interbonding angle increases and overpasses the angle $\cos^{-1}(-2m/3M)$. For fused silica, the value of the critical angle equals to $\sim$112° which is lower the mean angle 144°, so this model should accurately describe vibrations of the network.

A typical Raman spectrum presented in Fig. 7.4 shows the main vibrations deduced from Eqs. 7.15, as well as several other bands. Totally, one can mark 7 bands with the following assignment.

At **50 cm^{-1}** the so-called boson peak is placed. This is one of the universal features of disordered glasses typically ascribed to an excess density of vibrational states. The utilized experimental setup does not allow to record the low-frequency part of the spectrum, so we will not account for its significance in the following.

440 cm^{-1}. The dominant band is corresponding to vibrations with frequency ω_1 which is attributed to the bending motion of SiO_2 represented in Fig. 7.3b. Note that only atomic vibrations in n-membered rings with n higher than 5 contribute to this band.

495 and 606 cm^{-1} bands relate to "breathing" movement of the oxygen atoms in 4- and 3-membered rings, respectively. Several factors indicate the validity of this assignment: the presence of a peak closely placed to the value of 500 cm^{-1} in the Raman spectra of silica polymorphs consisting of 4-membered rings [SMN81, KH94]; simulation of vibrational modes of rings in silica and silanol ring molecules, as well molecular dynamics simulations [GG83a, PC98, LM03].

800 cm^{-1}. This band was attributed to the bending of the Si–O–Si bridge, but with a great displacements of Si atoms, represented in Fig. 7.3c) [LJ77]. This assignment is equally supported by the observation of significant shifts of the 800 cm^{-1} band in $^{30}SiO_2$ glass [GG83a].

Finally, the doublet at **1064 and 1200 cm^{-1}** was attributed to Si–O stretching motion (displayed in Fig. 7.3) and corresponds to the ω_4 frequency.

Acting Coulomb forces split this motion to longitudinal and transversal optical modes (LO–TO splitting) [GL76, LSH83].

In addition to these intrinsic vibrations, bands associated to impurities or intrinsic defects in the fused silica network can also be detected. If in silica network a large quantity of non-bridging oxygens is present, then significant changes could be observed in the 900–1200 cm^{-1} frequency range. This region is classically assigned to the Si–O symmetric stretching vibrations of the Q_n species. The strong bands centered at 1100–1050 cm^{-1}, 1000-950 cm^{-1}, 900 cm^{-1} and 850 cm^{-1} have been attributed to silicate tetrahedra with one, two, three and four non-bridging oxygens respectively [McM84].

In addition, one can observe vibrations of oxygen O_2 species. These are centered at 1555 cm^{-1} for intrinsic molecular oxygen O_2 [Nak09] or stretching vibration of O–O bond in peroxy linkages, calculated to be at 1480 cm^{-1} [CCB00].

In "wet" silica glass, modes correlating to the OH groups were equally reported. These imply a stretching vibration of silanol groups Si–OH, appearing as an asymmetric band near 3500 cm^{-1} and a weak band of stretching O–H vibration centered at 967 cm^{-1} [MR86].

7.3.2 Normalization procedure

To extract further practical information from the Raman spectra quantitative information about Raman cross-sections of the specific vibrations is often needed. However, changes of the glass density in the different zones of investigation (which are for many cases unknown), roughness of the surface, or the presence of scattering elements on the pathway of the light strongly affect the intensity of the measured Raman spectra. That is why quantitative measurements could be performed only after spectra normalization.

Absolute data on the number of oscillators could be extracted from the Raman and the reduced Raman spectra according to Eqs. 7.12 and 7.13. The most correct procedure of normalization in this case will be to take as a reference the area under the reduced spectrum in the whole spectral region. This assumes that the Raman coupling coefficient does not change drastically, so the area under the whole spectrum reflects the whole amount of vibrational states which should stay constant. However, in our case this procedure cannot be applied. The employed notch filter cuts a substantial part of the main band, so the total area under the spectrum cannot be calculated. Therefore, $g(\omega)$ cannot be extracted using calculation of the reduced spectra.

On the other hand, one could use relative data. In this case, the area under the peak of interest (usually the D_1 and D_2 peaks) is normalized with

respect of the spectral feature, characterizing the value which should be constant for all samples. Several spectral bands were considered as such normalization factor. The first one is the area of the $800\,\mathrm{cm}^{-1}$ band reflecting the number of Si atoms per unit of volume. An alternative way is to choose the intensity of the main band which is equally reported in the literature as the empirical normalization factor. Both approaches have strengths and weaknesses, and we will discuss them below.

Normalization to the $800\,\mathrm{cm}^{-1}$ band can be a good option when spectra are smooth enough, so the given band is well identified. For some cases, where the signal to noise ratio is poor, the calculation of the area under $800\,\mathrm{cm}^{-1}$ band bears a substantial error which is propagated into the whole spectra after normalization. This error can increase even more, since most of the spectral bands corresponding to the modified fused silica glass change their forms. This makes the spectrum normalization procedure quite difficult if to use only one feature as reference. We have compared results obtained using normalizations to the $800\,\mathrm{cm}^{-1}$ and the $440\,\mathrm{cm}^{-1}$ bands. They shows approximately similar results, but normalization to the main band gives less error when the spectra have substantial noise. That is why normalization of the spectra on the $440\,\mathrm{cm}^{-1}$ band was chosen. On the other hand, it was found that the shape of main band and its intensity changes. Using the proposed normalization method information about its intensity may be missed. Variation of the changes in the main band could, thus, be monitored by the measurements of its width.

To obtain D_1 and D_2 areas, subtraction of the background, which is approximated as a cubic polynom in the vicinity of the bands, was done. After the subtraction of the background, the numerical integration of the areas under the bands was performed. This procedure diminishes the number of fitting parameters making the final data more reliable. The as-extracted D_1 or D_2 peak areas divided by a normalization factor taken for the pristine and modified samples are therefore able to show changes in the amount of 3- or 4- membered rings in modified regions.

7.4 Spectroscopy of densified glass sample

Fused silica can be treated by different means to show an increasing density. Among these we recall the preparation of fused silica with higher fictive temperatures [GG83b, LP02], application of high hydrostatic pressure causing reversible [Wal81] and irreversible changes [HMBM86], densification by shock waves [ORS+99], UV exposure [Awa04], neutron [Bat74] and α-particles bombardment [Exa84]. We recall here the importance that local

Table 7.1: Changes in the Raman spectra of fused silica, densified with different means.

Treatment	ω_1	ω_4 (TO)	$I_{\omega_1}/\Delta_{\omega_1}$	I_{D_1}	I_{D_2}
Higher T_F [GG83b, LP02]	$\rightarrow$	$\leftarrow$	-/$\downarrow$	$\uparrow$	$\uparrow$
Cooling under pressure [BGL+08]	$\rightarrow$	$\leftarrow$	$\uparrow/\downarrow$	$\uparrow$	$\uparrow$
Reversible hydrostatic pressure [Wal81]	$\rightarrow$	$\leftarrow$	$\downarrow/\downarrow$	no eff.	$\downarrow$
Irreversible hydrostatic pressure [HMBM86]	$\rightarrow$	$\leftarrow$	-/$\downarrow$	$\downarrow$	$\downarrow$
Shock-waves [ORS+99]	$\rightarrow$	$\leftarrow$	-	no eff.	$\uparrow$
α-Particles [Exa84]	-	$\leftarrow$	$\downarrow$	no eff.	no eff.
Neutrons [Bat74]	$\rightarrow$	$\leftarrow$	-	no eff.	$\uparrow$

Notations: "$\rightarrow$" – shift to higher frequencies, "$\leftarrow$" – shift to lower frequencies, "$\uparrow$" – increase of intensity, "$\downarrow$" – decrease of intensity or narrowing.

density changes may have effect on the refractive index and the optical properties. A summary of the changes observed in fused silica by Raman spectroscopy (changes in intensity I, position ω and bandwidth Δ of certain bands) is given in Table 7.1. This makes possible to formulate the following trends of densification.

The general behavior of densified silica spectra is the shift of the main band (ω_1) to higher frequencies, accompanied by a shift of LO–TO doublet to lower frequencies. As predicted by Eqs. 7.15, this happens together with a decrease of the interbonding angle θ. Structural studies of the different polymorphs under ambient conditions given in Table 2.1, as well as data on pressure and temperature treated silica glass [DP94] confirm the dependence of the density of fused silica on the mean interbonding angle, indicating that the decrease of angle θ is the main of the densification paths.

The width of the main band Δ_{ω_1} depending on the tilt angle distribution δ [WH86] is also an important parameter characterizing the silica samples. The decrease of the width of the main band which is equivalent to a narrowing of the tilt angles distribution was usually reported for static pressure treated silica samples [BGL+08, Wal81, HMBM86]. This narrowing of the distribution of tilt angles arises from reducing the degree of freedom of the tetrahedra which usually happens in compacted silica samples.

The D_1 and D_2 peaks are the characteristic spectral features which were also considered for damage characterization; however, their use requires attention. For example, no effect or decreasing of its area were reported for cases when static reversible compression is applied. In this case, only the reorientation of the SiO_4 tetrahedra without bond breaking is happening. However, in shock wave compression or neutrons densification, D_2 increases. The common point of these processes is bond breaking and defect formation. The induced phase transitions occur fast and resolidification goes faster than required to reach the equilibrium, consequently mainly the D_2 peak increases. For the processes where energy deposition is relatively slow as in a case of thermal heating, the system has a sufficient time to reach a new equilibrium and then both peaks increase [GG83b, BGL+08]. Therefore, the D_2 (and D_1) peak increase as a sign of densification could be used only in particular cases, and considered also as a marker of inelastic densification (that is occurring with a bond breaking).

7.4.1 Densification with femtosecond laser pulses

The use of femtosecond laser pulses for inducing structural modifications in glasses has equally triggered activity in the field of Raman characterization. Fused silica [DMSH96, SB02, CTRK01, Rei06, PSS08, BBS+08, STS+11], other oxide and multicomponent glasses [Lit09, FWT+11] and chalcogenide glasses [ZRR+04] were investigated to this extent, focusing on spectral features associated to structural modifications.

Studies on fused silica samples confirm the general behavior of the spectral features of a densified network. They show systematic changes of the network structure which are expressed in D_1 [CTRK01] and D_2 band increase [DMSH96, CTRK01, SB02, BBS+08, PSS08], shifts of main peak to the higher frequencies, and shift of ω_4 (TO) to the lower frequencies [DMSH96, SB02, BBS+08, PSS08]. However some factors seem unclear such as shift and narrowing of main band [Lit09] and D_1 band behavior [PSS08]. In addition no studies concerning structure of type II traces with an accent on the difference with type I ones were performed. We therefore concentrate here on a space-resolved study on modulated refractive index structures and associated Raman characteristics in type I and type II/void traces.

7.5 Layered and inhomogeneous media

In many cases the discussion of Raman spectra becomes difficult because of sample inhomogeneities. Such samples should deserve particular consid-

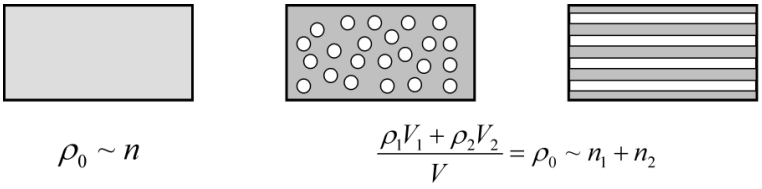

Figure 7.5: Homogeneous and different types of inhomogeneous samples having the same density considered in the present study.

eration in Raman measurements especially for laser driven modifications. The major reason comes from the small size of the investigated damaged area (which is in many cases inhomogeneous) in the conditions where the spatial resolution of the micro-Raman microscope often can not reach sufficient resolution values. In this case, the presence of pristine silica in the focal region of objective affects the spectrum of the modified region. For the same reason the studying of the regions of nanogratings also needs particular attention, since they are formed by an alternance of the layers having widths of tens to hundreds of nanometers with different densities and structural features.alternance of the layers having widths of tens to hundreds of nanometers with different densities and structural features.

To study this effect let us compare the signal from a homogeneous sample and from one having the same average density, but composed only from two phases of higher and lower densities. In this case, the Raman response will be calculated as sum of the contributions of each phase. Assuming that the laser field is uniform in the whole volume, the form and the spatial redistribution of inhomogeneities are not really important. The main significance comes from the total number of oscillators of each phase in the focal region of the probing laser and their spectral response. Therefore, this consideration may be applied for a structure where inhomogeneities are redistributed randomly in the volume and equally for a layered structure as illustrated in Fig. 7.5.

Let us also assume that the reference sample is composed from $2n$ oscillators. The two-layered medium is generated by a redistribution of oscillators in such a way that each layer has a different amount of oscillators: $n_1 = n+\delta n$ and $n_2 = n - \delta n$. Since the volume of the system in our assumption does not change, the overall density of this medium is equal to the original one. For simplicity, let us suppose that the medium has a refractive index close to unity, so no changes in electric field are observed near the interfaces. The Raman response of such a structure can thus be calculated as the sum of the

contributions of each layer, given by the following relations:

$$I_1(\omega) \sim n_1\sigma_1(\omega)|E_1|^2, \tag{7.17}$$
$$I_2(\omega) \sim n_2\sigma_2(\omega)|E_2|^2, \tag{7.18}$$

where $\sigma_1(\omega)$ and $\sigma_2(\omega)$ are the Raman cross-sections of the oscillators composing the high- and the low-density layers respectively. Moreover, since the field of the incident light is homogeneous in the whole volume $E_1 = E_2 = E_0$, the intensity of the scattered light from such a structure will be given by:

$$\begin{gathered} I(\omega) = I_1(\omega) + I_2(\omega) \sim (n_1\sigma_1(\omega) + n_2\sigma_2(\omega))|E_0|^2 \sim \\ \sim n[\sigma_1(\omega) + \sigma_2(\omega)] + \delta n[\sigma_1(\omega) - \sigma_2(\omega)]. \end{gathered} \tag{7.19}$$

This is different from that one measured from the original sample

$$I_0(\omega) \sim 2n\sigma(\omega) \tag{7.20}$$

Let us now consider some particular cases:

- Vibrational spectra of the different media are equal, so only density changes can play a role. In this case we have

  $$\sigma_1(\omega) = \sigma_2(\omega) = \sigma(\omega), \tag{7.21}$$

  and Eq. 7.19 transforms to 7.20. This means, that if fluctuations of density do not cause spectral form change in local regions, then no changes in the resulting spectra will be observed.

- One observes changes in line intensities. In this case there is no need to treat all spectrum, and only the consideration of the line of interest is sufficient. Let us consider the D_2 line. In our hypothesis changes are caused by the increase of concentrations of 3-membered rings in denser regions while no changes in ring statistic was observed in lower density region. Introducing the spectral response of this line as $G(\omega)$, the last condition can be written as:

  $$\sigma_1(\omega) = (1 + \delta A)G(\omega); \sigma_2(\omega) = \sigma(\omega) = G(\omega), \tag{7.22}$$

  where δA is the increase in peak intensity in the denser region. The form of the line remains the same. In this case the detected intensity changes will be equivalent to:

  $$\delta I = I(\omega) - I_0(\omega) \sim \delta n \delta A G(\omega). \tag{7.23}$$

If changes in density were caused by the redistribution of denser elements from one region to the other,

$$\sigma_1(\omega) = (1 + \delta A)G(\omega); \sigma_2(\omega) = (1 - \delta A)G(\omega), \tag{7.24}$$

then the observed changes in measured Raman signal will be higher,

$$\delta I = I(\omega) - I_0(\omega) \sim 2\delta n \delta A G(\omega). \tag{7.25}$$

- Changes in line position can happen. Usually only small changes in line positions are observed, where the shift in the line position is lower than its width. Such changes will cause only broadening of the lines in the measured spectrum.

- Finally, if the lower density medium is hollow, as happens when investigating a voids or cracks, this equivalent to the case when all oscillator migrates to the denser region and no oscillators remain there:

$$\delta n = n. \tag{7.26}$$

In this case measured signal will be

$$I(\omega) = I_1(\omega) \sim 2n\sigma_1(\omega). \tag{7.27}$$

The arguments explained above can be equally applied to the case where the spatial resolution is limited for the fine investigation of small features of modified regions. In this case, according Eqs. 7.18 the useful Raman signal coming from modified regions $I_2(\omega)$ will be averaged with pristine silica $I_1(\omega)$. The ratio $I_2/I_1 \sim n_2/n_1$, therefore, will characterize the useful yield of the scattered signal. The volume occupied by the region of interest is characterized by the number of oscillators n_2, which is smaller than number of oscillators in the probed volume of adjacent media n_1. Consequently the ratios n_2/n_1 and I_2/I_1 tends to a zero when $n_2 << n_1$, indicating that the useful signal will be totally screened by the adjacent media. For this reason, it is very important to adjust or increase the spatial resolution in the investigation of small features of modified regions so only they would fit in the focal region. Special preparation of traces that reduces the scattering from undesired regions or pristine glass is required in this case.

Considering hollow and void-like regions, I_2/I_1 tends to zero according to Eqs. 7.26 and 7.27. In this case the scattering signal from the denser phase in the vicinity of the voids will equally suppress the signal from the lower density phase. On the other hand, probing two-phases structures composed of the regions of different densities should sufficiently change the form

of spectral bands. The resulting Raman scattering signal is a contribution of the scattering light from different phases having slightly different spectral response, usually in the band positions. This should result in a certain broadening of the bands. The effect is expected to be most dramatical for the main band and the ω_4 doublet which show sufficient changes in their peak positions for glasses of different densities. According to the above arguments, broadening will be sufficient unless the fraction corresponding to one of the layers is small.

7.6 Experimental setup

The Raman spectra were collected with the same micro-Raman spectrometer ARAMIS presented in the previous chapter. Two principal wavelengths were used for excitation: light from Ar^+ laser at 488 nm and from a HeCd laser at 442 nm. These usually give a high efficiency of the scattering signal and low luminescence background. The Olympus MPLN 50× NA=0.8 objective was used, both for excitation and for collection of the scattered light in backscattering configuration. The focusing conditions allow a spatial resolution of approximately 1 μm. Depth resolution (axial) is defined by the choice of the confocal diaphragm; diameters of 50 μm and 100 μm define depth resolutions of 3 μm and 5 μm. The increase of resolution greatly reduces the amount of collected light and significantly affects the accumulation time. Thus, a choice of diaphragm should ensure a high signal but with the ability of observation of local changes in the bulk. The 50 μm aperture diaphragm fulfills these requirements; however, to obtain spectra with reasonable S/N ratio, the accumulation time was in the order of 1 minute per each point. For those cases where alternative diameter was chosen in order to reduce the accumulation time, a note will be additionally placed.

Choice of grating with 1800 grooves per mm defines a spectral resolutions of 1 cm^{-1}.

The subsequent study is structured in the following way. Firstly, we explore the structure of isotropic type I traces produced by multiple pulses. Then we will focus on the study of anisotropic structures characteristic to type II regime and we will compare results to establish the differences between these two regimes. Finally, early stages of the photoinscription (single and few pulses) will be investigated to obtain insights in the mechanisms of the gradual development of damage.

7.7 Type I regime

For the type I regime a series of investigations was performed on the isotropic waveguides. Traces were written with different energies per pulses and several translation velocities. Different velocities will define the dose of the exposed area in terms of the effective acting pulses, defined according to the relation 4.4. On the other hand, the translation velocity was varied in the limits favorable to the type I regime. The parameters of the writing procedure were chosen equivalent to that ones reported in the Section 4.7.1. Pulses with energies of 1 and 2 μJ and pulse duration τ_p=130 fs were focused by the objective OB2 with NA_{eff}=0.3 at a repetition rate of 10 kHz.

Raman investigations were performed by cutting the sample across the waveguides and investigating their cross sections. By focusing the excitation radiation of the HeCd laser source with a wavelength of 442 nm on the surface of the sample using a 50x objective with NA=0.8, a spatial resolution of less than a micron was obtained. With such resolution one can always pick up the center of modification which is the region of maximum structural changes.

One can notice numerous changes which happen with the Raman spectra of the modified region with respect to the pristine glass; these are depicted in Fig. 7.6. Most of the bands change their form and exhibit little or significant shifts. The highest shifts were measured for the main band (440 cm^{-1}), which moves to higher frequencies, and for the high-frequency doublet (1064 and 1200 cm^{-1}), which moves to lower frequencies.

Great changes were observed in the D_2 peak which represents the concentration of 3-membered rings. Its area was found to increase approximately 6 times for the highest refractive index changes region in comparison to the pristine silica, as shown in Fig. 7.7. The D_2 peak also exhibits a shift of approximately $\sim$10 cm^{-1} to higher frequencies. On the contrary only little increase in the area (25 %) but sufficient broadening ($\sim$10 cm^{-1}) and upshift $\sim$16 cm^{-1} were found for the D_1 peak. These observations appear not to support fictive temperature model according to which the D_1 peak should show a greater increase (85 % for the given 6 times D_2 increase according to [GG83b], that is in agreement with previous studies [PSS08]).

Another characteristic spectral feature is the band shift caused by the changes of the interbonding angles. The dependence of main band and ω_4 LO–TO doublet positions as a function of the accumulated energy dose were plotted in Fig. 7.8. In the same figure we can observe that the shift of the main band to higher frequencies is accompanied by a narrowing of this band. This could be considered as another sign of densification.

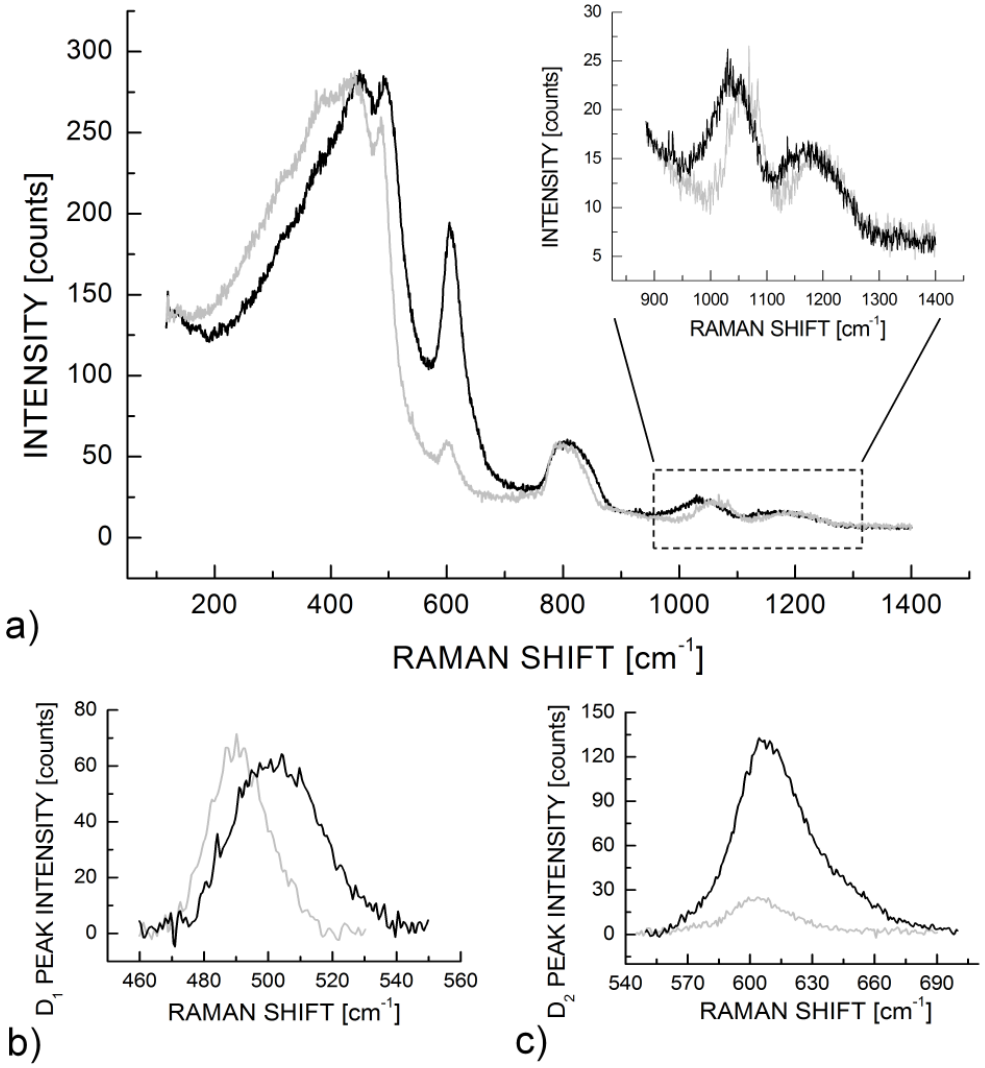

Figure 7.6: a) Raman spectra of the pristine (gray curve) and the modified by N_{eff}=100000 pulses (black curve) fused silica sample in type I regime. The inset shows changes that take place in the high-frequency region such as shifts in ω_4 LO–TO bands. Subtracted b) D_1 and c) D_2 areas show up-shift and broadening of the D_1 peak and up-shift and a six times increase of the D_2 peak.

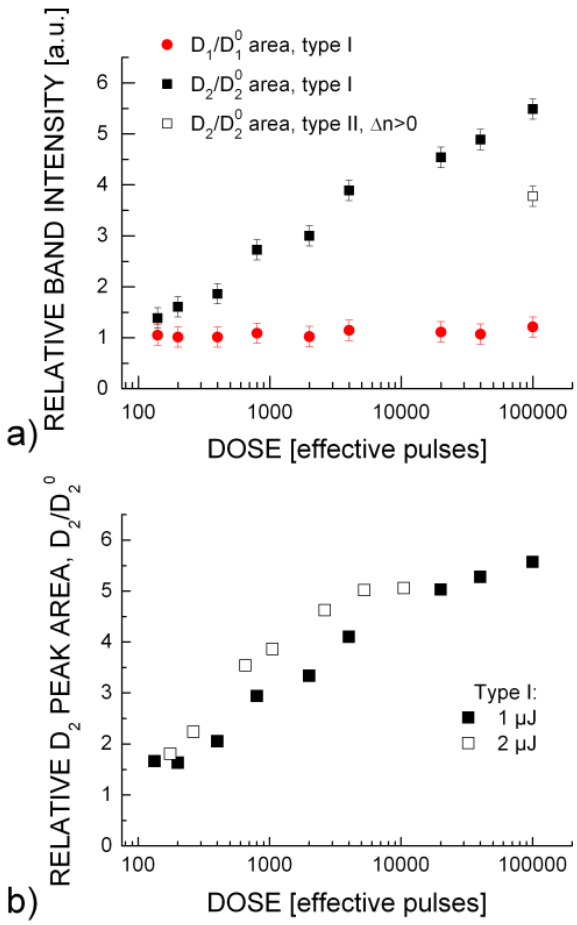

Figure 7.7: a) Measured D_1 and D_2 areas as a function of the irradiation dose for type I damage produced by 1 μJ pulses. For comparison D_1 area of positive index change region in the core of type II-WG traces produced by 3.2 μJ pulses is indicated by the empty square region. b) Comparison of D_2 peak areas for 1 μJ pulses (filled squares) and 2 μJ pulses (empty squares) showing saturation occurring after some accumulation threshold. The analyzed traces were produced using 140 fs pulses focused with the NA_{eff}=0.3 objective at the repetition rate of 10 KHz.

7.7.1 Densification scenarios

As discussed in Chapter 2, the decrease of the mean interbonding angle θ in the silica network leads to the increase of its density. As shown in [GG83b], the angle θ could be accurately calculated with the Eqs. 7.15 and 7.16. Using

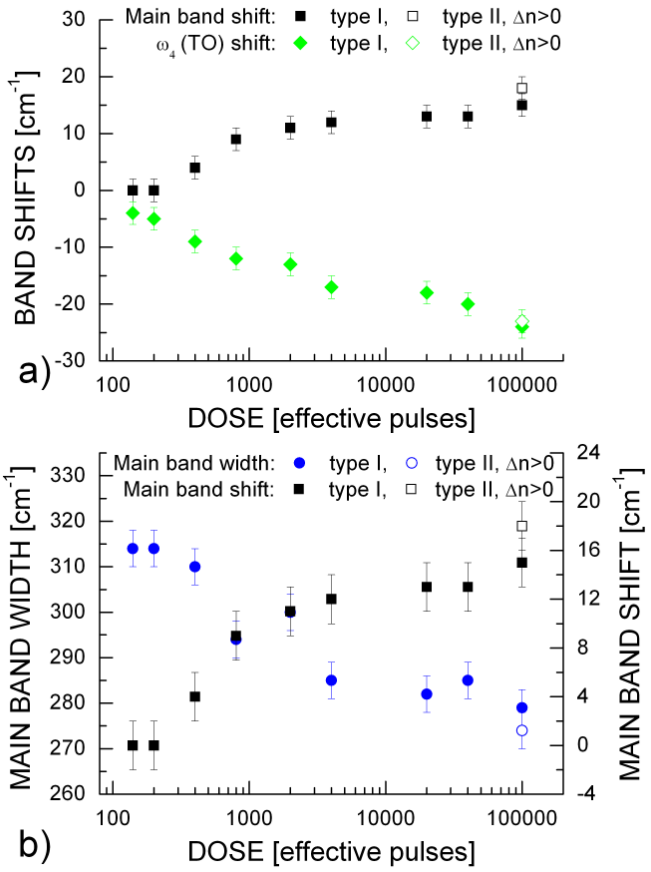

Figure 7.8: Measured a) ω_4 (TO) shift, and b) main band shift and width changes as a function of the accumulation dose for type I and type II-WG traces. Type I traces were produced with 1 μJ 140 fs pulses focused with the NA$_{eff}$=0.3 objective at the repetition rate of 10 KHz. Type II longitudinal traces were produced with 3.2 μJ and only positive index changes region in the core was considered.

this approach, the maximum angle changes were estimated at $\Delta\theta = 4.6°$.

For further estimation of density changes we develop an approach based on the angle reduction in the network of crystalline quartz. The average ring size and the mean angles θ are approximately the same for fused silica and quartz. For this reason, the well defined and studied network of quartz could be a good model. Using the data from the [Kih90] concerning structural

changes during α–β phase transitions of quartz, the ratio

$$\Delta\theta = (-0.30 \pm 0.02) d\rho/\rho \tag{7.28}$$

between changes of the interbonding angle and the silica density was obtained. This ratio is valid near the angles of $\sim$145° and reflects only density changes caused by 6-membered rings. Using this method in accordance to Eqs. 7.16 and 7.28 a maximum densification rate of $d\rho/\rho$=2.4 % corresponding to $\Delta\theta = 4.6°$ was obtained.

It is worth noting that the proposed mechanism used in the evaluation of density could not give exact densification rates. The error could arise from the suggestion that only the contribution of 6-membered rings is accounted for densification; however, the presence of small 3- and 4-membered rings, as well as loose 7- and 8-membered rings could sufficiently influence volume changes. The use of this approach, however, can be appropriate when the density change occurs after elastic deformation of the silica network, for example after static pressure compaction or in the stressed regions.

Another approach to calculate the densification rate basing on ω_4 peak position shift was proposed in [PSS08]. The authors claim that the variation of the refractive index and the absolute value of the ω_4 peak shift for fused silica increase linearly with density, and this correlation does not depend on the reason of densification. We assume, however, that there is a certain variation of Raman bands shifts which are defined by the mechanisms of densification such as thermal mechanism based on the fictive temperature model, pressure compaction, or defect-induced densification.

Considering these discrepancies in the estimated densification rates, it seems useful to compare our evaluated results with that ones produced by independent methods. In our case this can be associated with refractive index changes extracted from far and near field measurements of the modes propagating in the written waveguides. In Chapter 5 we have evaluated the highest refractive index changes at Δn=0.002 for 633 nm transported light. Below we will give an estimation of refractive index changes and densification rates which could be achieved by different glass treatments.

- Thermodynamical approach based on fictive temperature model predicts an increase of density of fused silica up to value of T_f=1550 °C. For a maximum densification rate of $d\rho/\rho$=0.2 % [Bru70, She04] the change of the ω_4 (TO) band is equal to 11 cm^{-1} [GG83b]. Assuming that such dependency could be extrapolated for higher densities, the maximum densification rate $d\rho/\rho$=0.45 % can be achieved for $\Delta\omega$=24 cm^{-1}. According to Eq. 2.13, refractive index change of Δn=0.0019 corresponds to this densification rate, which coincides with the measured value.

- Studies of neutron irradiation of silica can give an evaluation for the non-thermal mechanism of densification. For density changes of $\delta\rho/\rho = 2.4\,\%$ [Pri58], the corresponding shift of ω_4 shift band was reported to be of $26\,\mathrm{cm}^{-1}$ [Bat74] with a corresponding refractive index changes in the order of Δn=0.007 [Pri58]. Using these data one can estimate a defect-induced compaction rate of 2.3 % and RIC in the order of Δn=0.006.

- Phenomenological evaluation of compaction induced only by reduction of the angles in the 6-membered rings (Eq. 7.28) gives a densification rate of $d\rho/\rho$=2.4 % and corresponding refractive index changes of Δn=0.007 (according to Eq. 2.13 and assuming that this is elastic densification), which are higher than the evaluated ones.

- Finally, the approach proposed in [PSS08] directly addresses the refractive index changes induced by various mechanisms to the ω_4 shift. Using the ratio $dn/d\omega_4$=-0.002 from the above paper, even more overestimated refractive index changes Δn=0.048 can be obtained.

The comparison of the results of the above proposed models gives the following findings. Results on the neutron-irradiated silica and the angle reduction phenomenological approach offer similar predictions of the densification rate based on the measured ω_4 shift; however, both these approaches give an overestimated (three times) value of RIC. On the other hand, the use of the thermodynamical model predicts the value of the measured refractive index changes, but these results are produced after the extrapolation of the fictive temperature model beyond the limits of its applicability. This fact indicates that the thermal mechanism does not work alone and pressure compaction and defect-assisted densification could equally take place in structural modifications. This subject will be discussed later. Nevertheless, for estimating density changes occurring in type I waveguides, the ratio given by thermodynamical model could be applied as being the nearest to optimal:

$$\frac{d\rho}{d\omega_4} = 4.2 \times 10^{-4}\, cm^{-2} g \tag{7.29}$$

7.7.2 Type I/II transition and crack formation

The effect of a higher energy was equally investigated using the traces produced by 2 μJ pulses. Generally, high energy pulses are more efficient for waveguide writing, as they induce higher index changes. The study of a

higher energetic regime is also important to the extent of irreversible transitions from smooth isotropic type I modification to type II, considered as catastrophic material damage. The results displayed in Fig. 7.7b show that for type I densification rate estimated in the terms of D_2 peak area rises sufficiently faster for the $2\,\mu$J pulses. However, after the dose of approximately 10^4 pulses, the changes of the D_2 area becomes almost equivalent to the maximal one produced with $1\,\mu$J pulses in type I regime, indicating that the saturation of the damage occurs. In addition, PCM pictures of traces produced with a higher accumulated dose shows that at a certain moment type I to type II regime transition happens. In these conditions the regimes become unstable and non-guiding low index traces are often produced. For $1\,\mu$J pulses, the type I to type II transitions occur at a dose higher than 10^5 acting pulses for NA_{eff}=0.3, τ_p=140 fs.

It was suggested in the literature that 3-membered rings are stressed units in the silica network, so an increase in their concentration leads to higher fragility of the glass [Awa04]. One can propose that, at the saturation level, the glass becomes fragile enough to form cracks. Being the centers of local field enhancement, regions of cracks are favored for efficient nanoplasma generation and their transformations to nanosheets according to the nanoplasmonics model of nanogratings formation [BSR+06].

We propose another mechanism of cracks formation in type I/II regimes transition. This originates from the tensile stress which arises after silica resolidification [BBS+08]. This assumption allow us to imagine the laser affected zone as a solid cylinder, which shrinks due to a localized increase of material density and induces a stress pattern that appears at the periphery of the traces and out of the laser affected zone. Since stress occurs at the resolidification stage its relaxation is difficult, that could eventually lead to cracks formation. This will happen if the value of the stress will exceed the tensile strength of fused silica. Assuming that change of density profile is stepwise, the stress is given by relation:

$$\sigma = \delta\rho/\rho K \tag{7.30}$$

where K is the bulk modulus (K=37 GPa). According to this equation a tensile strength σ_{max}=50 MPa for fused silica is achieved for a densification rate 0.14%, that is sufficintly lower than the rate predicted by Eq. 7.29 for the traces written at doses corresponding to type I/II transition. Gradual density changes in the modified region should give lower value induced stress, however we assume that cracking is still highly probable.

7.8 Type II regime

As it was shown in the previous subsection, Raman spectra vary as a function of the number of pulses and the energetic and focusing conditions. That makes a direct comparison of spectra of homogeneous type I and type II traces difficult. Even produced by the same energy of the pulses, they have different distributions of laser intensity in the focal region because of different character of nonlinear propagation of the pulses. Nevertheless, certain densification trends could be extracted from the qualitative comparison of the spectra recorded in the different region. The results of the corresponding comparisons between type I and type II birefringent or type I and type II positive RIC zones is indicated below.

7.8.1 Nanogratings region

The main difficulty in the birefringent region, as it was stated above, that the laser intensity distribution in the traces produced by multiple pulse radiation could be changed, increasing in the vicinity of inhomogeneities of the material in the birefringent region [BSR+06]. However, we found that a comparison of D_2 band as a function of ω_4 (TO) for different regions should show fundamental spectroscopic differences. Performing the observation of the spectral features of the birefringent regions of type II traces in both cross-section and side-view geometries, the following observations were made:

- The overall intensity of birefringent regions is always lower. This could happen because of the lower densities in the probed region but also due to light scattering on the local inhomogeneities. This is in agreement with PCM observations, since the birefringence regions appear as average lower refractive index zones, and support the theory of lower density layers (or possibly hollow cracks) constituting these structures.

- In the regions of birefringence, despite its overall negative refractive index changes, significant variations in the D_2 peak and the ω_4 (TO) band shift were observed, similar to the type I case. This is not unusual, because, according formulas 7.23, 7.25 and 7.27, for a sandwich-like structure consisting of denser and hollow layers, the normalized spectra will repeat the spectra of denser layers.

- For samples having the same D_2 normalized band area, type II birefringent regions show an ω_4 (TO) shift of approximately $3\,\mathrm{cm}^{-1}$, lower than for the type I traces. Such behavior could be explained by the effect of an interface. Since tetrahedral units have a higher degree of

freedom at the interface this favors their reorientation while conserving the interbonding angle close to its equilibrium value. The last is close to the average interbonding angle in pristine silica [NG80] and has higher value than in the denser material, that eventually leads to minimal angle changes.

7.8.2 Positive refractive index core

In addition, we performed the investigation of the type II regions in the zones responsible for the smooth and positive refractive index changes. The most convenient way was to study its characteristic on cross-section of the type II guiding traces in the central region of the core. The traces were performed in conditions corresponding to the observation of strong luminescence in the tail of the traces, where the erasure of the nanograting zone was the most efficient and the core of the waveguides is well presented. In our case the 3.2 μJ pulses were focused with the OB2 NA_{eff} at 150 fs with the dose of approximately 10^5 pulses. The corresponding traces were cut and polished before the measurement, similarly as in the type I case. We can therefore compare these modifications with that one produced in type I traces, however the latter produced at lower pulses energies. The results is shown in Figs. 7.7 and 7.8.

We found that type II isotropic regions undergo lower increase of D_2 band, similar changes of the ω_4 (TO) band and sufficient changes in the main band: its shift to higher frequencies is higher and the band is narrower than the corresponding one written in type I regime at the maximum densification rate. The variations in the Raman bands show that intertetrahedra angle θ changes are of the same order or even higher comparing with isotropic type I region. The narrower main band indicates that the overall densification of the glass is even higher in type II regime.

On the other hand, the behavior of th D_2 band indicates on the different character of the densification if one compares with the type I traces. The smaller increase of D_2 is more characteristic to thermal mechanism of densification. That could mean that at high pulse energies, indeed, the conditions are sufficient for the softening or melting of the material.

7.9 Early stages of photoinscription

The few pulse traces produced in type II irradiation regime allow to study the precursor stages which lead to further changes in the material structures leading to the formation of birefringence regions. For this case, traces

considered in the sections 6.4.1, 6.4.2 and 6.5.1 of Chapter 6 were equally investigated using Raman microscopy. We similarly will consider two energetic regimes. Focusing at moderate energies allows to concentrate the attention on hollow regions. However, using high energetic pulses unusual types of modification caused by the extreme character of interaction, like off-axis regions of densification, will be investigated.

Static traces investigated in this section were produced by focusing with the objective OB1 (NA_{eff}=0.42) either single pulse or N=20 pulses, each with energy of 1 μJ and 150 fs pulse duration. These parameters allow to produce damage sizes convenient for the investigation of the material structure both in the vicinity of void-like region and in the filamentary zone. Since the spatial resolution of the Raman microscopy setup is lower than the transverse size of single static shots, traces were grouped in arrays consisting of 4 static traces with a spacing of 2 μm between each other. Such organization allows to reduce influence of the surrounding media on the measured useful Raman signal. The maps displaying the overall spectral intensity, normalized D_2 area, and ω_4 (TO) shifts are presented in Fig. 7.9. The following observations can be made.

Structural modifications were already observed just after the first pulse. The D_2 band increases both in the black and white parts of the traces, as well as the main band ω_4 shifts, similar to densified silica.

The minimum of the overall spectral signal coincides with the regions looking white on PCM pictures. Since a lower spectral signal could be interpreted as a result of probing regions with a lower amount of oscillators (lower density), this fact allows to identify these regions as voids.

The map of normalized D_2 area follows the shape of the area of the structural modification with a maximum coinciding with the region of the void and its close vicinity. Since the axial spatial resolution was higher than the size of the void, the signal coming from the close vicinity of the void was also collected so mainly the contribution of the compacted region around the void is present on the spectra. At the same time the highest D_2 peak area was observed in the vicinity of the void. Since the conditions of interaction with the light were the strongest in that point, this could lead to silica expansion or evaporation, leading to the void formation and to the consequent densification in its vicinity as a result of internal pressure. By the relative increase of the D_2 band in the vicinity of void, the rate of densification was estimated at 0.1 % according to the thermodynamical densification mechanism using ω_4 shift (following Eq. 7.29) and D_2 increase.

For the multiple pulses trace, the maximum densification was estimated at 0.15 % in the dark black region situated between two voids (region denoted as A in Fig. 7.9b). This indicates that major material changes happen after the

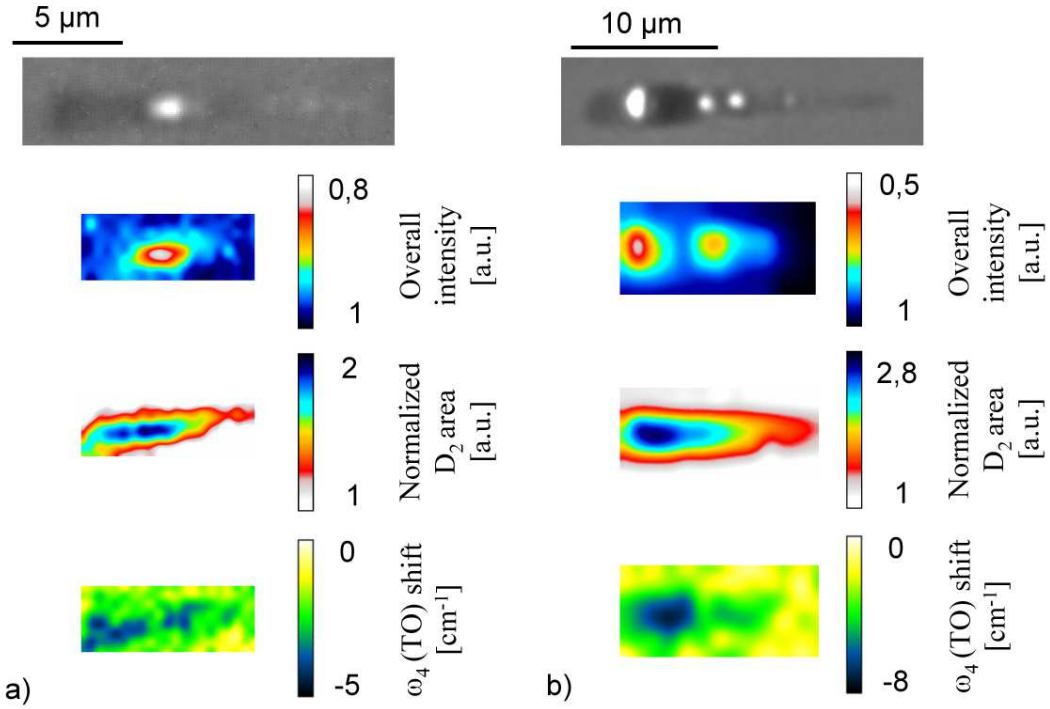

Figure 7.9: PCM images and Raman cartography maps of overall spectral intensity, normalized D_2 area, and ω_4 (TO) shifts for traces produced by a) single and b) N=20 laser pulses with an energy of 1 μJ and 150 fs pulse duration each, focused by an objective with NA_{eff}=0.4.

first pulse arrival; however, the accumulation effect leading to nanostructuring is important only at long irradiation series. No fundamental differences in Raman spectral signatures characterizing positive refractive index changes zones with different contrast (regions denoted as A nd B) were detected.

Comparing spectral signatures of the regions in the vicinity of the voids, the shift of the ω_4 (TO) is higher in the zone of positive refractive index changes. In the region of the void, despite a higher D_2 normalized area, smaller shifts were measured both for the single and the 20 pulses traces. Summarizing these observations and comparing them with the similar behavior observed in the birefringent regions, one could conclude that this is equally related to the presence of interfaces.

7.9.1 High energy case

We have studied before low to moderate energetic regimes characteristics for writing optical functions. Peculiar features appear when a high energy pulses are used. To study this interaction regime traces were photoinscripted with 30 μJ single pulses and pulse duration of 150 fs focused by the NA$_{eff}$=0.4 objective. We recall from Chapter 6 that the distinctive features clearly observed on these traces are: 1) a region of NBOHC formation without visible PCM mark, 2) compacted off-axis regions. Considering that these traces have higher cross-sectional size, a diameter 100 μm of confocal diaphragm was chosen to record Raman spectra. The corresponding maps of D_2 normalized area and ω_4 (TO) shifts are presented in Fig. 7.10 for different damage regions. Corroborating these results with the PL maps displayed in Fig. 6.5, several regions demanding attention could be further analyzed.

We first explored the region denoted as 1 in Fig. 7.10, preceding the visible permanent modification zone, where no refractive index changes were detected using PCM but PL reveals a high amount of NBOHCs. Raman spectra show no signs of densification here. Equally, no changes in the high-frequency regions, responsible for Q_i tetrahedral unit vibrations were detected. Such behavior indicates that only relatively small amount of breaking bonds across the whole network is present. However, such rupture could be a precursor for densification. If the concentration of the created non-bridging oxygens is high enough, a new network can be formed corresponding to the denser silica as predicted by [DD96, ZAF+06]. Thus, bond breaking could have an important role in the non-thermal mechanisms of network reorganization.

Secondly, the increase of D_2 band was observed mainly on the axis of the beam (region denoted as 2 in Fig. 6.5). Since this region is the region of stronger energy absorption, densification could be caused by thermal reorganization of the network and subsequent fast quenching. Such temperature elevation should produce pressure wave, which could be a cause of the off-axis region of densification (regions 3), where no significant D_2 band increase with ω_4 (TO) shift was detected. This resembles of a "cold" compaction without formation of 3-membered rings.

7.9.2 Cumulative effect of densification

Results displayed in Figs. 7.7, 7.8, 7.9 clearly show the cumulative character of densification as a function of the accumulated dose both for type I and type II regimes of writing. Furthermore, observations concerning regions preceding positive index zones (depicted in Fig. 7.10) allow us to put forward the suggestion that, in certain conditions, densification occurs after bond

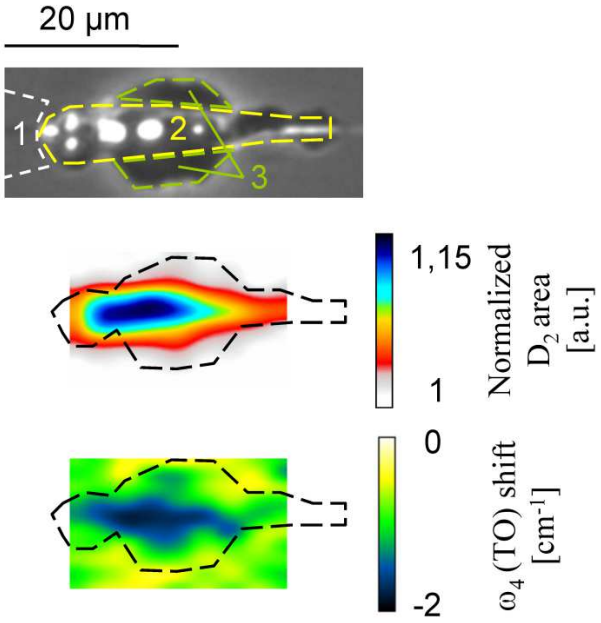

Figure 7.10: PCM images and Raman cartography maps of the overall spectral intensity, normalized D_2 area and ω_4 (TO) shifts for traces produced by a single laser pulse with an energy of 30 μJ focused by an objective with NA_{eff}=0.4 and pulse duration of 150 fs. Several regions are marked: 1) bond breaking without densification, 2) on-axis thermal-assisted densification and 3) off-axis pressure densified regions. The shape of the region of visible changes detected with PCM is plotted by using contour lines. *Note:* pictures show underestimated values of relative variations in the spectral features since the signal is averaged with the neighboring unmodified fused silica material.

breaking under relatively low temperatures. This defect-assisted mechanism of densification, can take place in type I regime of writing. In addition, thermodynamical model meet some difficulties in explanation of such accumulation effects. According to it, a melt phase should be achieved before each cooling cycles that involves loosing of the information about material state each time before melting. There are several more arguments against an involvement of a standard thermal model as explained in Sections 2.2.2 and 3.3.1.

However, the several phenomena point out to the existence of a melting phase in the region of interaction in, given by the morphology of damage during surface ablation or the ability of erasing the cracks by further pulses

in the bulk [THS08]. Energetic conditions correspond to type II regime of interaction in these cases. The few experiments that attempted to measure the temperature in the region of interaction obtain values of temperature equals to 1500 K in the bulk [STS+11] and 3000 K at the surface in the region of microexplosions [LMG02]. That is enough not only for material melting but also for it vaporization, considering the regime of microexplosion.

The most reliable suggestion, therefore, will be that two extreme effects are taking place depending on the energetic conditions. It could be defect-assisted densification characterizing type I and filamentation regime for conditions where a low number of electrons is generated in CB (and consequently low temperatures of the lattice can be achieved; see discussion in Section 3.3) at low energy densities. For high energies or for longer pulse durations where sufficient concentrations of electrons and consequently lattice temperatures can be achieved, thermodynamical and mechanical models of densification including melting may work.

Nevertheless, we do not reject the possibility of explaining the accumulation of damage with the presence of the melt. Here we propose several views of the accumulation phenomenon based on a thermal model.

- Melting is going not homogeneously in the whole laser affected zone but locally, which could be the result of the "forest-fire" type of multiphoton ionization [GLS+04], perhaps with the help of defects. As a result of such inhomogeneous melting, the measured Raman spectra will be calculated as weighted Raman spectra of modified regions and of the regions less exposed by ionization. While the next pulses arrive, the volume of non-modified regions is reducing, that leads to the increase in the contribution of the signal from the modified regions until its saturation.

- Defects generated by preceding pulses increase the ionization cross-sections and, as consequence, the absorbed energy and local temperatures in the region of interaction increase. Then different densities could be produced either from the different temperature level or with a diverse cooling rate.

- Finally, melting is going homogeneously, however the equilibrium structure of the melt has not been achieved during each melting cycle. This situation is schematically depicted in Fig. 7.11 showing different cycles through non-equilibrium region. Indeed, the fictive temperature model demands that the melt reaches its structural equilibrium before starting the cooling procedure. In Chapter 3 the time needed for

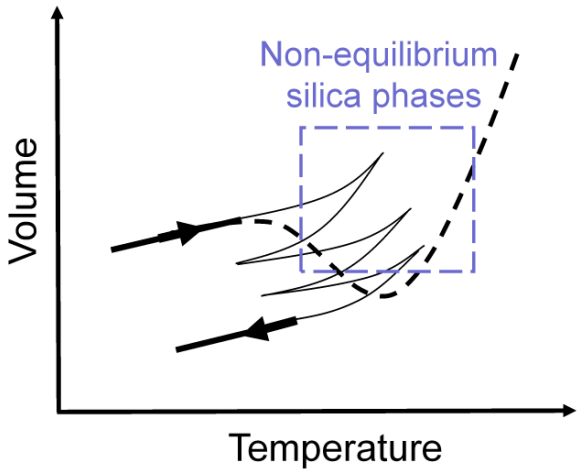

Figure 7.11: Schematic volume-temperature diagrams describing the effect of densification accumulation in fused silica under ultrafast phase transitions in repetitive cycles of heating and cooling.

silica to achieve its equilibrium was estimated at 10 μs near the softening point of silica. With the growth of the silica temperature, this time decreases, but not severely (to the order of 0.1 μs for T=2500 K). At the same time theoretical estimations [STS+11] supported by experimental results [EZN+08] show that at characteristic times of 1 μs the silica network is already cold, so the structure which was actually frozen in corresponds to non-equilibrium silica. The structural equilibrium becomes closer to achieve as next pulses arrive, that finally leads to saturation of densification.

7.10 Conclusions

Complex Raman analyses of the modified fused silica matrix allow to conclude that the decrease of interbonding angles, the narrowing of dihedral intertetrahedra angle distribution, and the increase of the amount of three-membered rings are the main factors contributing to the densification mechanisms, since they were observed in all densified samples. The spectra of modified fused silica may depend on the irradiation conditions. Thus, we highlight several regions with different spectral patterns:

- Bonds breaking due to STE relaxation was found firstly in the region where no refractive index changes happens. This could be precursor for

non-thermal mechanism of densification. Even if the temperature could not reach values close to the softening point, bond breaking happens and densification can occur due to defects relaxations.

- Type I regime of writing corresponding to smooth positive refractive index changes is characterized by the increase of three-fold rings and the decrease of the interbonding angle. Both these parameters vary as a function of pulse energy, and accumulated dose (number of the pulses acting during modification).

- Positive refractive index changes zone of type II traces responsible for guiding in the longitudinal traces has similar densification trends as type I traces; however, the increase in three-fold rings is lower, that could indicate on the melting occurring in these regions.

- Regions of lower density, observed in type II regime of interaction in the birefringent regions for multiple pulse damage and in the void-like regions observed at the primary stages, characterized by smaller changes of interbonding angle if compare with densified type I regions having the same increase of three membered rings.

- For extreme energetic conditions, densified regions outside the axis of the beam was identified. These regions are characterized by decrease of interbonding angles with no significant changes in three-fold rings.

This indicates that simple theories such as fictive temperature model can not be fully applied for characterization of modified silica network. In fact femtosecond laser densification of fused silica is an interplay of thermal scenarios, defect-assisted densification and compaction by pressure waves involving non-equilibrium structures of the fused silica network.

Chapter 8

Processing of BK7 glass

The interest of 3D laser processing relies equally on its applicability to different classes of glass. If typical fused silica due to its densification characteristics and its relaxation behavior shows a large processing window for positive index changes, other types of glasses are more difficult to process. We will focus here on a glass material still based on a silicate structure but with a fundamentally different behavior under femtosecond laser irradiation, the Schott borosilicate crown BK7 glass. The potential use of femtosecond laser pulses for structuring bulk BK7 glass with the aim of inducing refractive index changes and subsequent fabrication of optical devices was previously demonstrated in [HM98, SB02, BSC+05, MBM+08, Lit09].

BK7 glass is widely used as a low cost technical optical glass for applications in the visible region. The chemical composition of BK7 as specified by Schott in percentage by weight is the following: silica (70), boron oxide (11.5), sodium oxide (9.5), potassium oxide (7.5), barium oxide (1), titanium oxide, calcium oxide and impurities in small quantities. This leads to some peculiarities in the electronic structures, lower softening temperature and, notably, a high expansion coefficient (approximately 10 times higher than for fused silica). The present studies were carried out on the N-BK7 glass samples, where index "N" indicates that this type of glass is free of arsenic and lead, that makes N-BK7 glass transparent up to 280 nm in the UV spectral range.

In the present chapter we performed different laser-assisted modifications of BK7 glass resulting in either positive or negative refractive index changes. Equally, we have carried the corresponding PL and Raman studies and compare them with the previously reported observations in fused silica. Some general guide lines for processing glasses are indicated.

8.1 Borosilicate crown (BK7) glass structure

Let us consider the influence of the network modifiers such as boron and metal alkali atoms on the silica network. The alkali metal atoms dramatically change the silica network, since they lead to bond breaking of the polymerized silica structure according to the following reaction:

$$\equiv \text{Si–O–Si} \equiv + \text{R}_2\text{O} \rightarrow 2 \equiv \text{Si–O:R}. \tag{8.1}$$

where R denotes the alkali metals Na or K.

Additionally, the presence of alkali metals influences the boron network. Normally, boron has a valence of three in B_2O_3 glass, whose network consists of BO_3 units. However, the addition of alkali modifiers in borate and borosilicate glasses leads to a change of its normal valence. This transforms, taking the valence of four, and, in consequence, BO_4 tetrahedral units appear in the network. In silicate crystals these tetrahedral units could be incorporated in the silicate networks forming some sort of 4-membered rings consisting of one or two atoms of boron [MGN09]. These are danburite units, $R_2B_2Si_2O_8$, consisting of two boron atoms in the ring and reedmergnerite units, $RBSi_3O_8$, that have only one atom of boron.

A considerable amount of results about the structure of borosilicate glasses has been obtained with nuclear magnetic resonance (NMR) technique [YB78, DBX83, WS98]. According to these results the model of reedmergnerite and danburite units composing borosilicate network was put forward. It was shown that in glasses with a molar ratio between alkali, boron and silica close to that one in BK7, significant mixing of silica and boron subnetwork happens [WS98]. Thus, we should speak about Si–O–B units partially composing the glassy network. However, a characterization procedure which uses only these units has some difficulties. For example, not all the boron atoms can change their valence. It is known that the borosilicate glasses undergo phase separation between boron and silica networks resulting in inhomogeneities with the size of the order of hundred angstroms. According to Konijnendijk [Kon75, KS75] efficient incorporation of boron atoms into the silica network needs high pressures. The presence of non-incorporated boron species was equally found using NMR technique [WS98]. Therefore we do not see any reasons against the presence of boron not incorporated in silica, in the form of piroborates units $B_2O_5^{4-}$ or in the form of metaborate boron rings $B_3O_6^{3-}$.

8.2 Ultrafast laser processing of BK7

As in the case of fused silica, the use of different focusing condition produces various types of damage. Similarly to the fused silica case we will separate the resulting traces traces according to the focusing conditions and the optical properties of the generated structures in two groups: type I and type II traces. Hereafter we will discuss only dynamic scanned traces (produced with sample translation). All characteristic types of damages are displayed in Fig. 8.1.

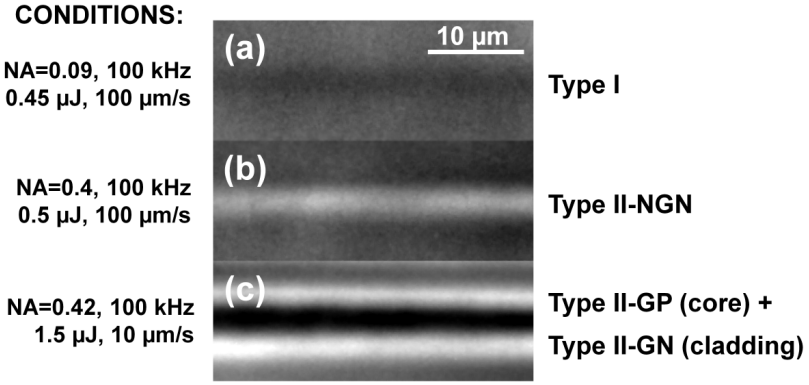

Figure 8.1: Various regimes of modification induced by femtosecond laser pulses in BK7 glass as a function of the writing conditions. These are: a) type I of weak positive RIC, b) type II-NGN with negative RIC and c) Strong positive RIC type II-GP region in the core surrounded by negative RIC cladding type II-GN region.

At very low laser fluences shallow positive index changes ($\Delta n \approx 10^{-4}$) can be produced, which we will call type I accompanied by a slight coloration of the sample. These RIC can be made either with the use of a low-NA or with the slit-shaping technique that preserves a low energy density. In the first case, we used OB3 with NA_{eff}=0.09 to focus 0.45 μJ pulses of 150 fs at 100 kHz and with the translation speed of 100 μm/s. Slit-shaping work was performed by our colleagues at the Institute of Optics, Madrid using alternatively a low repetition rate system (1 kHz) [Sol].

Increasing the laser fluence, negative RIC can be produced, called type II-NGN traces (see Fig. 8.1b). We generated them by focusing 0.5 μJ pulses at 100 kHz with the translation speed of 100 μm/s with the use of the objective OB1 of NA_{eff}=0.4. The reason for the negative RIC can be associated with thermomechanical expansion of the heated region followed by quenching in

the low density phase [MBM+08].

Increasing the energy of the pulses and the effective number of acting pulses even more, positive refractive index changes could be induced in the core again, which we will denote as type II-GP (Δn>5×10^{-3}). This can be seen as a replication of compression shell appearing around the interaction region. This region is surrounded by a zone of negative refractive index changes denoted as type II-GN. These modifications were generated by focusing 1.5 μJ and 150 fs ultrashort laser pulses at 100 kHz with the translation speed of 10 μm/s via the objective OB1 of NA$_{eff}$=0.4.

As a side note, no nanogratings were observed in case of type II in BK7 glass.

8.3 PL spectroscopy

Following the same strategy utilized for fused silica we have tried to characterize these specific regions via PL and Raman spectroscopy. The objective was to indicate specific electronic and structural transitions characterizing type I and type II structures.

Defects excitation occurs via several absorption bands attributed to the borosilicate glasses. Following the previous optical studies on alkali borosilicate glasses [GAG+01] we will take into account H_1^+ H_2^+, H_3^+, H_4^+ centers. These hole trap centers are attributed to a more studied alkali-silicates [MSH66]; however, due to certain similarities in the chemical composition and network structure we expect appearance of these centers in BK7 glass. In addition to these hole-trapping centers placed near the valence band, one considers equally electrons traps, placed near the conduction band. Here we will consider only hole-trapping centers since the used excitation sources cover their characteristic absorption energies, which are presented in Tab. 8.1.

In terms of photoluminescence we have observed the 540 nm (2.3 eV), the 650 nm (1.9 eV), and the 775 nm (1.6 eV) PL bands under different excitation sources. PL occurs even in unmodified BK7 glass sample as indicated in Fig. 8.2. The assignment of these PL bands could be related to intrinsic point defects but also to the luminescence of the metallic ions. These ions can be included in the network as impurities. For example, numerous works reported PL broad luminescence bands in the red part of the visible spectrum produced by Fe^{3+} ions in alkali-silica and borosilicates. Photoluminescence was equally reported in these host materials centered at 625–725 nm for tetrahedral Fe^{3+} and in the near infra-red at 875 nm for octahedral Fe^{3+}.

The 650 nm band observed under Ar^+ 488 nm (2.54 eV) excitation and the 775 nm band appearing under HeCd 442 nm (2.81 eV) excitation were

Table 8.1: Absorption and photoluminescence bands of point defects reported for borosilicate glasses.

Name	Absorption band (eV)	PL band (eV)	Comments
H_1^+		3–3.8	Stable up to 500 K
H_2^+	2.8		Stable up to 350–425 K *
H_3^+	2.0		Stable up to 350–425 K
H_4^+	4.0		Stable up to 425–550 K

* Could be thermally transformed to H_3

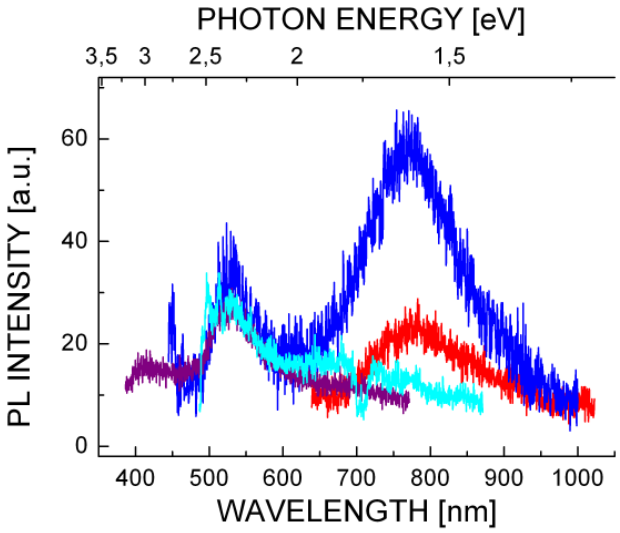

Figure 8.2: PL spectra of the pristine BK7 glass for different excitation sources. PL spectra under different excitation sources are indicated by different colors. The red line is the HeNe 633 nm (2 eV) excitation, light blue – Ar+ 488 nm (2.54 eV), blue – HeCd 442 nm (2.81 eV) and magenta – HeCd 325 nm (3.8 eV).

previously observed and reported in the present work in the case of fused silica, where they characterize NBOHCs. Additionally, as it will be seen below, the intensities of these two bands show a certain correlation for the different modified regions, thus, we assume that the PL of these bands and the PL at 775 nm under HeNe 633 nm (2 eV) are likely caused by NBOH

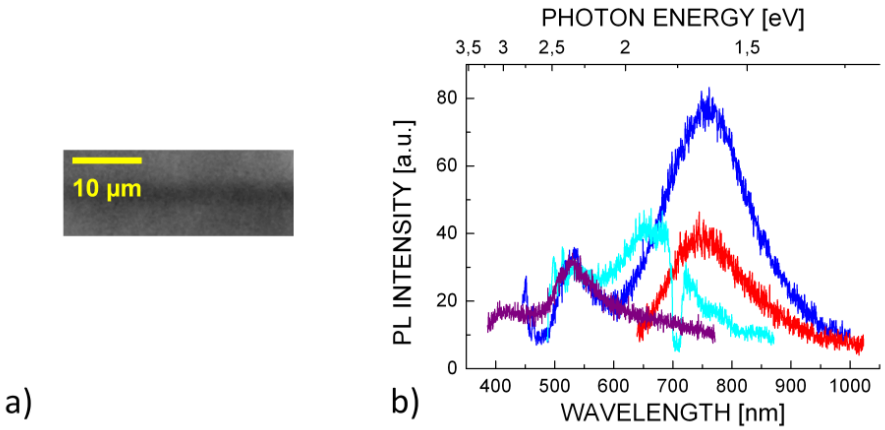

Figure 8.3: a) PCM image of type I modification of the BK7 glass and b) PL spectra assigned with type I structures. Color indications of different excitation sources are the same as in Fig. 8.2.

centers. Concerning the 540 nm (2.3 eV) band, there is no clear evidence of its assignment.

8.3.1 PL results

Hereafter we will present the main results of the spectroscopic study performed on the modified glass samples. The characteristic PL spectra for different excitations will be presented for each type of modification.

Typical PL spectra of type I traces displayed in Fig. 8.3 indicate a slight increase of the 775 nm band under HeNe laser light (633 nm) and HeCd laser light (442 nm) but an increase of the 650 nm band under Ar^+ 488 nm light is especially visible. This may perhaps mean an increase of NBOHC states. However, it is equally possible that the concentration of some third center increases since, since Ar^+ and HeCd (442 nm) laser sources are non resonant for NBOHCs, and their excitation occurs after energy transfer via intermediate defect states.

Since type II (NGN, GP, GN) traces show radial inhomogeneities of the modification distribution across the section of the longitudinal traces, the samples were cut and polished to study the cross-section of these traces and the corresponding spectral maps were plotted. HeCd 442 nm light excitation reveals the 540 nm luminescence band characterizing unknown defects and the 775 nm band characterizing NBOHCs. Thus, spectral maps of these single bands can be plotted after spectral deconvolution. The deconvolution was

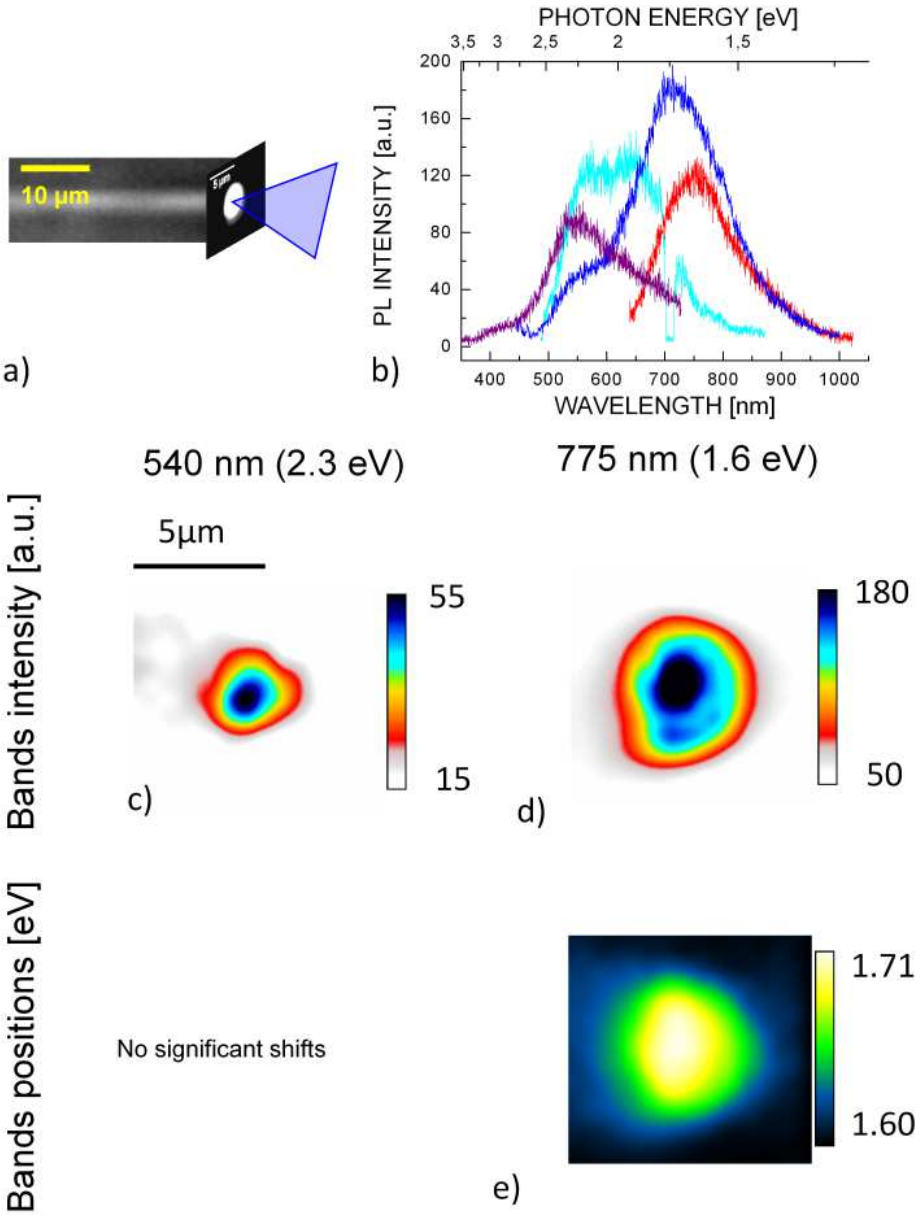

Figure 8.4: a) PCM image of type II-NGN modification in BK7 glass showing schematically the geometry of cross-section map spectroscopy. b) The associated cross-section PL spectra, where color indications of different excitation sources are the same as in Fig. 8.2. Bottom: 2D spectral maps of c) the 540 nm band. d) The 775 nm band intensities and e) 775 nm band shift upon excitation with HeCd (442 nm) light.

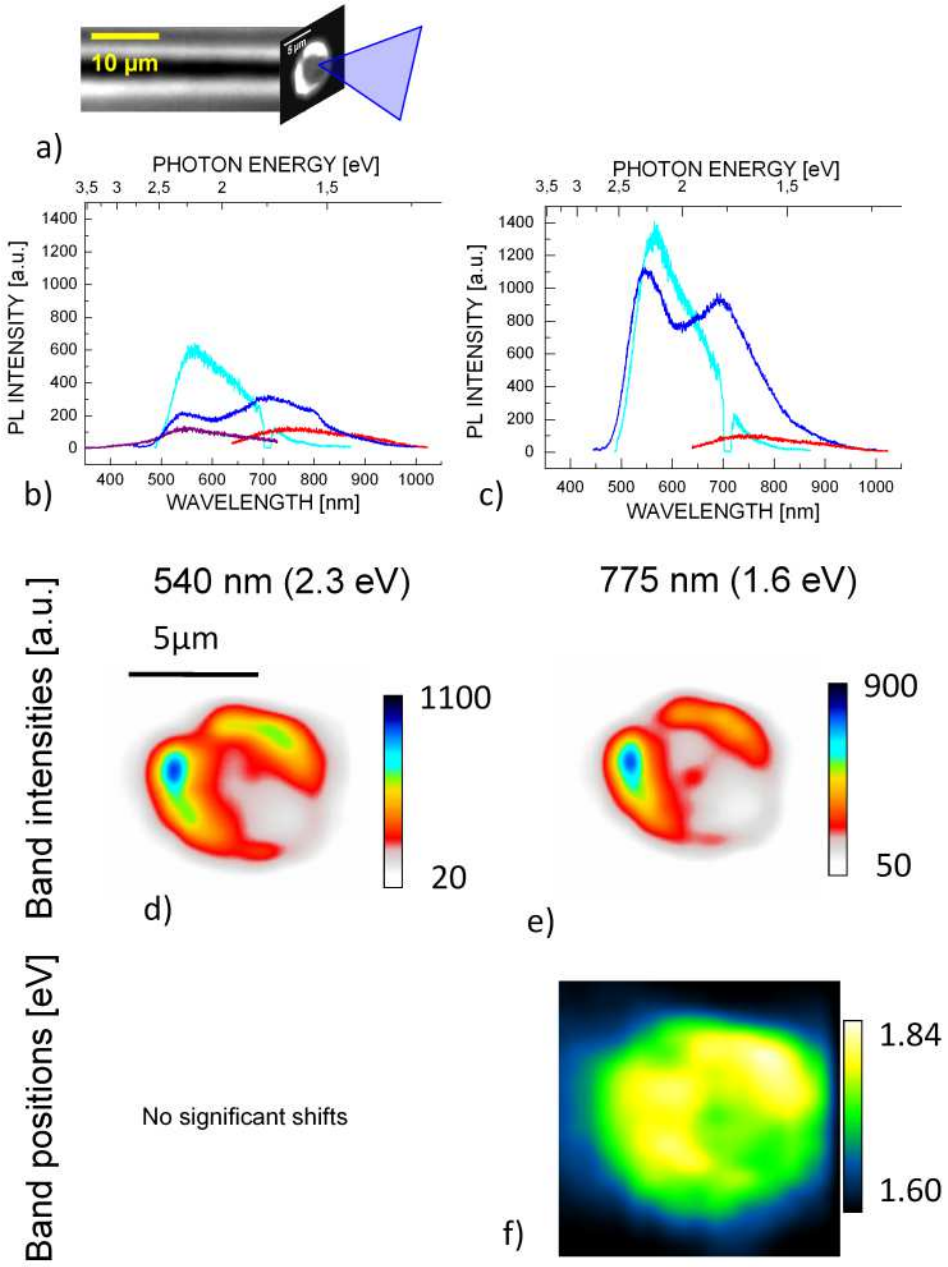

Figure 8.5: a) PCM image of type II-G modification in BK7 glass showing schematically the geometry of cross-section map spectroscopy. PL spectra of b) type II-GP and c) type II-GN regions, where color indications of different excitation sources are the same as in Fig. 8.2. Bottom: 2D spectral maps of d) the 540 nm band. e) The 775 nm band intensities and f) 775 nm band shift upon excitation with HeCd (442 nm) light.

performed in the energetic domain (eV), where the bands have a symmetrical form.

2D spectral PL maps of type II traces show already significant modifications in both 775 nm and 540 nm bands, with sufficient increase of the bands intensities and a shift of the 775 nm band position. The results are presented in Figs. 8.4 and 8.5.

Considering the type II-NG trace, two regions of interest can be identified. The central region of the negative RIC is the region where the 540 nm band and the 650 nm band intensities increase. The 775 nm band intensity augments as well with the shift of the band position towards the blue spectral region. On the periphery, another region with different spectral patterns can be defined. There the 650 and 775 nm bands there exhibit the most visible changes, but the 540 nm band rests unmodified. The spectral signature of this region is similar to the type I region. Based on the above facts the following structure of the type II nonguiding longitudinal traces can be proposed: this is type II negative RIC region, surrounded by the shallow type I positive RIC regions on the periphery, where the energetic conditions were not such strong as in the center of the cross-section.

Equally, the spectroscopy map of the type II guiding trace shows two different spectral patterns. In the type II-GP region of positive RIC in the core a strong increase of the 540 nm and the 775 nm bands was observed. In the type II-GN region of negative RIC an even stronger increase of the 540 nm band was detected.

Additionally, the 775 nm band excited with 442 nm (2.81 eV) excitation is strongly distorted in the modified regions (both type II-GP and type II-GN) and shifts toward the lower wavelength achieving the minimum at approximately 700 nm (1.8 eV). One should note here, that the value 700 nm (1.8 eV) corresponds to the NBOHC luminescence under 442 nm excitation in fused silica. This can indicates that the observed 775 nm band excited with 442 nm (2.81 eV) and 622 nm (2.0 eV) has complex structure with contribution of different centers including NBOHC, Fe^{3+} or other metallic impurities. The increase of this band accompanied by the shift to 700 nm (1.8 eV) means dominant luminescence of NBOHCs there.

As the 488 nm (2.54 eV)and the 442 nm (2.81 eV) excitations do not resonantly activate NBOHCs, we can not directly address the observed PL intensity of the 700 nm band with the concentration of these centers. More likely that in the negative RIC zones high signal of NBOHC more is caused by precursor centers and H_2^+-centers, having absorption band at 2.8 eV. To supplement these data, we have used the 633 nm, as presented in Fig. 8.6, since it directly excited the NBOHCs. In this case the 650 nm and the 775 nm bands are not so intense in the cladding region comparing to the region of

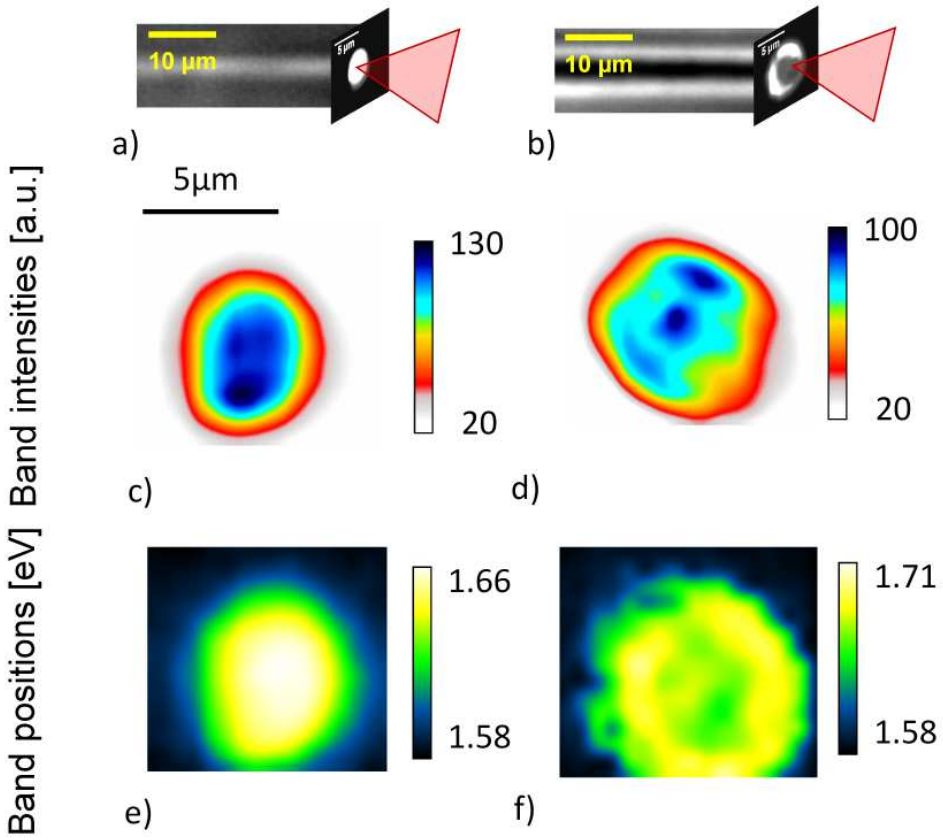

Figure 8.6: PCM image of a) type II-NG and b) type II-G modifications in BK7 glass showing schematically the geometry of cross-section map spectroscopy. Bottom: 2D spectral maps of c), d) the 775 nm band intensities and e), f) the 775 nm band shifts upon excitation with HeNe (633 nm) light of the type II-NG and the type II-G modifications, respectively.

the core, indicating a smaller concentration of NBOHCs in the type II-GN region.

Summarizing the observations, a general pattern can be identified. In regions of positive RIC the 650 nm and the 775 nm bands showing the presence of NBOHC are always well defined indicating a dominant presence of these centers. However, in the region of negative RIC, apart the NBOHC luminescence, the band at 540 nm related to yet unknown centers appears and start to play a visible role, suggesting a different chemical and structural environment.

8.4 Interpretation of the Raman spectra.

We give below a complementary view of the laser-modified structures using Raman spectroscopy. Typical Raman spectra are displayed in Fig. 8.7. Since BK7 is composed from silica at around 70 %, it is natural to consider the vibrational bands on that ones, associated with silicate and boron subnetworks including possible vibrations of Si–O–B units. Assuming this, the following assignment of the bands could be given.

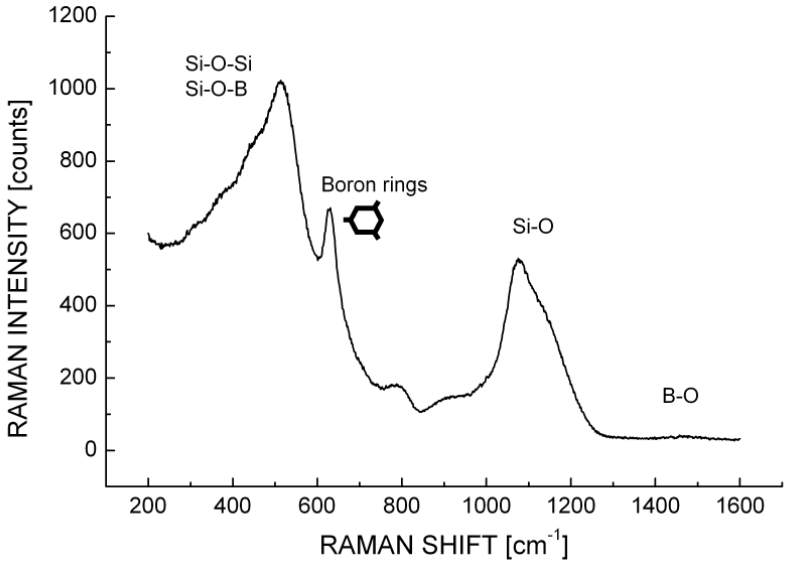

Figure 8.7: Raman spectrum of the pristine BK7 glass.

Vibrations of the silica network are in many details similar with those observed in the fused silica Raman spectra (see Chapter 7). The exact band

positions however may change due to the environment. These are: a main band centered at 520 cm^{-1} which is a result of Si–O–Si bending vibration, and the 790 cm^{-1} band vibrations of silica network with substantial Si atoms movement. The strong peak in the high frequency region appears due to the vibrations of the nonbridging oxygens. It consists of three bands at 950 cm^{-1}, 1080 cm^{-1} and 1160 cm^{-1} indicating stretching vibrations of Si–O bonds in the Q_2, Q_3 and Q_4 units. Those are SiO_4 tetrahedra with 2 and 1 nonbridging oxygens, and completely connected tetrahedra.

Considering the vibrations of the boron subnetwork, as already reported, we will take into account boron incorporated in the silica network and pure boron network. Several indications based on the spectroscopic observations point out to the validity of this argument. The characteristic peak at 628 cm^{-1} was assigned in different works either to danburite-like units or to metaborate units which are 3-membered boron rings. Reedmergnerite and danburite ring units vibrations at 580 and 614 cm^{-1} respectively were already indicated [BTH+88, MGN09]. Another assignment is based on the existence of small rings by analogy with the D_2 peak. These are metaborate units $B_3O_6^{3-}$ reported for potassium (sodium) metaborate $R_3B_3O_6$ crystalline networks. The position of the Raman peak can be tuned in a certain range depending on the chemical composition of the glass. In such a way crystals have Raman lines placed either at 610 cm^{-1} (for K) or 630 cm^{-1} (for Na). These vibrations correspond to symmetric bending vibrations of all 3 boron atoms in the ring [Kon75, Bri76]. Nevertheless, we will not exclude wide bands in the region $\sim$600 cm^{-1} which could possibly derive from bending vibrations of the Si–O–B bridge [MGN09]. Finally, in the high-frequency region at 1470 cm^{-1}, a band associated to the stretching vibrations of boron nonbridging oxygens is placed [FW81].

8.5 Raman spectroscopy results

Spectroscopic measurements were performed on the cross-sections of the longitudinal traces. After background subtraction, the spectra were normalized at the main band intensity of the unmodified BK7 glass sample. For further interpretation, differential Raman spectra were calculated, indicating the difference between the spectra of normalized modified and pristine glass regions.

8.5.1 Type I traces

Since only small positive variations in the refractive index were measured for such traces, equally, minimal changes in the network reorganization were detected. That is why expecting very small changes in Raman spectrum and, consequently, in order to to diminish the signal from the non-irradiated sample we performed our studies on the longitudinal traces written with slit shaping technique (these ones have higher diameter) in cross-sectional geometry. Refractive index change of the traces was estimated in the order of $\Delta n = 2.5{\times}10^{-4}$.

The spectral changes are illustrated on the differential Raman spectra in Fig. 8.8. Negative changes in the band intensities occur at 450, 630, and 1080 cm^{-1} which are the positions of the main spectral maxima of the pristine BK7 sample. At the same time, the spectral signal increases in the range of 800–900 cm^{-1}. This can be interpreted either by increasing of a particular spectral band in that region or by the broadening of main and high frequency bands. The latter means introducing a certain degree of disorder in the lattice.

One question relies to the mechanism of positive soft RIC in BK7 and we believe that these kinds of structural modifications show significant differences as compared to the positive RIC induced in fused silica. We have indicated in Chapters 2 and 7 that in the fused silica case, the changes in the optical properties are connected with the changes in the material density and could be deduced from the fictive temperature model. The non-standard behavior leads to higher density upon fast cooling (Fig. 3.4). In the case of BK7 glass the situation is not similar. We expect a standard cooling behavior with a density decrease upon cooling due to the domination of the thermal expansion of the BK7 glass network. Thus, the thermodynamical approach should give negative refractive index changes. We observe nevertheless a RIC similar to type I on fused silica. This indicates that, on the contrary, type I modification in BK7 glass is characterized by bond breaking (see results in Section 7.3.1) with little of network reorganization. Such kind of rearrangements can induce refractive index changes via variations in atomic polarizability [LAG+11].

8.5.2 Nonguiding type II longitudinal traces

A certain class of changes was detected for vibrations characterizing silica subnetwork in type II-NG traces. To this extent, we observe slight changes in the main band. We assume that some vibrational acoustic modes of around 300–400 cm^{-1} decrease in strength. In the high-frequency region changes in

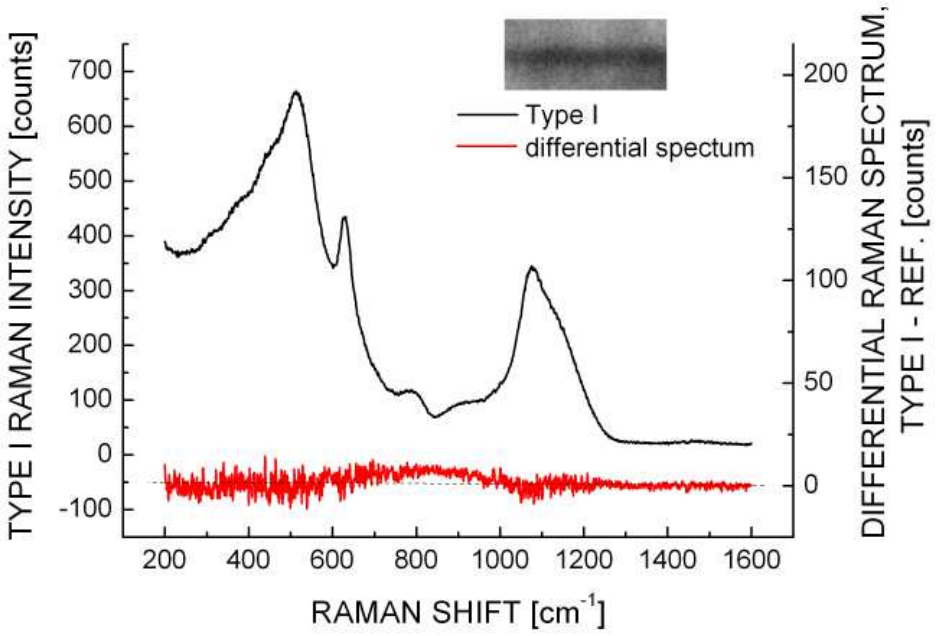

Figure 8.8: Raman spectrum of type I positive RIC longitudinal trace.

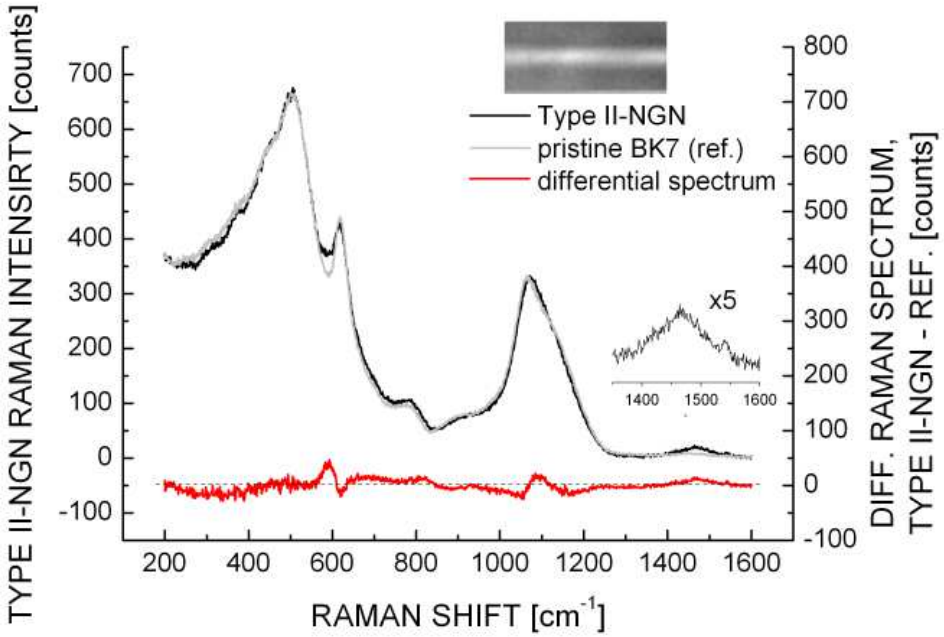

Figure 8.9: Raman spectrum of nonguiding longitudinal trace of negative RIC (type II-NGN).

the spectral form of the 1080 cm^{-1} band were equally measured. The changes can be attributed to shifts of the 1080 cm^{-1} band towards higher frequencies with the slight decrease of 1160^{-1} bands indicating bond breaking in the silica subnetwork.

The boron subnetwork undergoes on the contrary significant changes. The 630 cm^{-1} peak decreases sufficiently and becomes broader indicating the breaking of bonds in the boron subnetwork. The detected augmentation of the 1470 cm^{-1} band indicating the increase of B–O breaking bonds fits the previous finding.

Finally, a small peak centered at 1540 cm^{-1} indicating molecular oxygen appears (see Fig. 8.9). This confirms a bond breaking scenario accompanying rarefaction/cavitation scenario similarly observed in β-irradiated borosilicate glasses [BPG+99].

8.5.3 Guiding type II longitudinal traces

The silica subnetwork undergoes the greatest changes in this writing regime. In the positive RIC region (type II-GP), the main peak shifts approximately 7 cm^{-1} to higher frequencies. We consider this as a sign of densification via the reduction of the interbonding angles in the silica network. At the same time considerable changes happen in the high-frequency spectral region. The 950 cm^{-1} band slightly increases, the 1080 cm^{-1} increases sufficiently, while the 1160 cm^{-1} band decreases. This involves the rise in the number of SiO_4 tetrahedra with 1 and 2 nonbridging O atoms, with a decrease of fully connected tetrahedra, indicating efficient processes of bond breaking.

In the boron subnetwork the 630 cm^{-1} peak decreases a little. The background level under this band goes up, which could be a result of the increase of the ∼650 cm^{-1} region associated with the changes in the main band. The 1470 cm^{-1} band becomes higher, indicating the presence of B–O nonbridging oxygens.

Considering the negative RIC region (type II-GN), no significant shifts in the main band were detected; however, its form changes. Almost no changes happen with the 630 cm^{-1} peak. Observing the high-frequency region, the intensities of the 950, 1080 and 1470 cm^{-1} bands are increasing; however, the character of the band changes looks different if compared to the type II-GP region. For example, the 1080 cm^{-1} peak is less intense.

The small peak at 1540 cm^{-1} characterizing molecular oxygen is presented in type II-GP region; however, it seems absent in type II-GN.

These observations allow us to conclude the following: the negative RIC observed in this case has a different character than that one observed type II-NGN regime. Firstly, important spectral changes occur in the bands char-

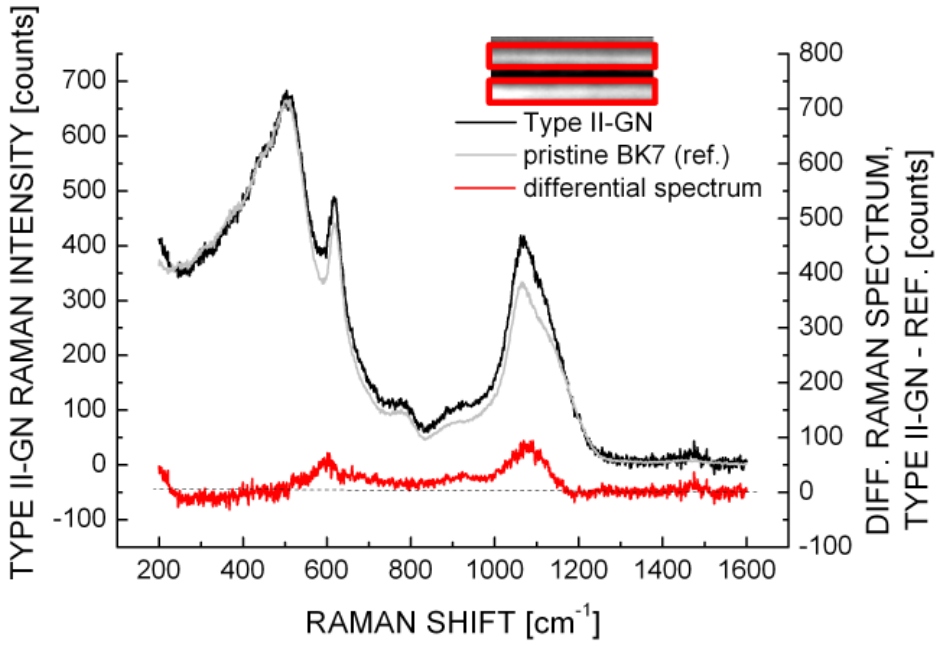

Figure 8.10: Raman spectrum of the negative RIC region for the guiding longitudinal trace (type II-GN).

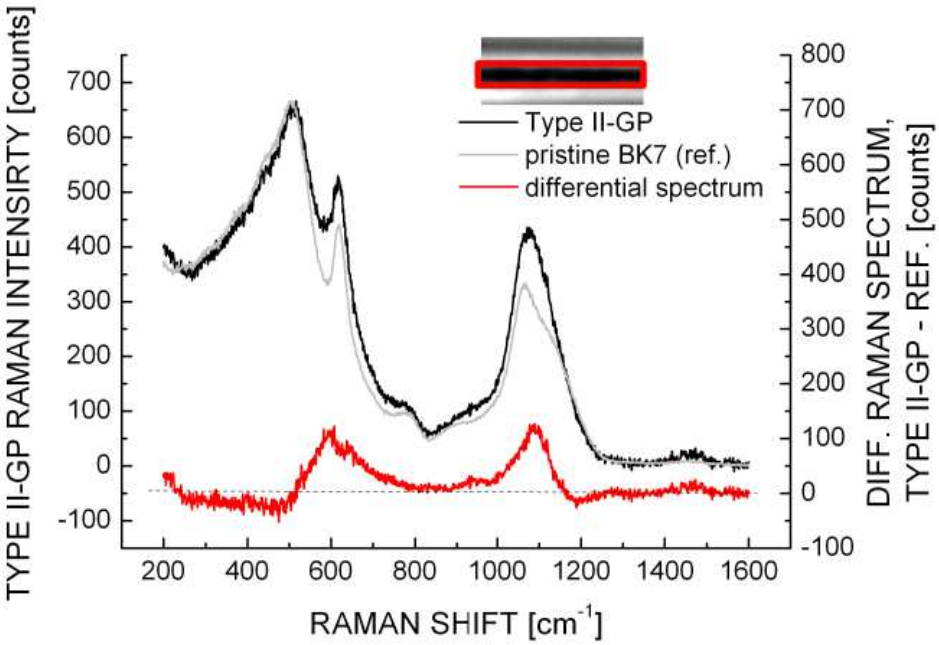

Figure 8.11: Raman spectrum of the positive RIC region for the guiding longitudinal trace (type II-GP).

acterizing silica subnetwork. Secondly, it is situated on the periphery of the traces, where the intensity of laser field was the lowest; therefore, structural changes are possibly caused by the incubation effect or due to thermomechanical mechanism and subsequent accumulation effects.

In the case of the type II-NGN traces, the 630 and 1470 cm^{-1} bands, characterizing the boron subnetwork undergoes greater changes. In addition, the modified zone is placed on the axis of the laser beam. Thus, rupture of the bonds mainly in boron/ boron-incorporated network is caused by strong interaction with the light and relaxation of the photoionized material. This effect is accompanied with oxygen dissociation, which rests stable in the form of O_2 long time after exposure. The last was detected in β-irradiated silicate glasses [BPG+99], where oxygen can be stored in the generated pores (small bubbles of 50 Å diameter). Therefore, it indicates that negative index changes of type II-NGN traces could be explained by density changes produced due to material expansion.

Positive RIC region is also sustained by the bond breaking in the whole network; however, hydrodynamical mechanisms lead to material redistribution and consequent compaction in this region [MBM+08]. This is expressed in the reduction of the interbonding angles in the silica subnetwork.

8.6 Discussion and conclusions

We have investigated both positive and negative refractive index changes induced in BK7 glass samples irradiated by femtosecond laser pulses. The produced modifications can be divided in the two classes similar to fused silica. These involve shallow positive refractive index changes called type I and more stable to heat treatment type II modification. The latter could be equally divided in positive or negative RIC domains.

We demonstrated that under low energetic densities, smooth type I positive RIC are induced in BK7 glass. However, these kind of structural modifications have a significant difference with positive RIC induced in fused silica. Type I modification in BK7 glass were shown to be characterized by bond breaking with only slight network reorganization. Thus, refractive index changes can be induced by changes in the atomic polarizability in this case.

Type II modifications are generated under high energies of laser irradiation and are characterized by substantial bond breaking and defect formation. This is visible on the associated PL and Raman spectra. Generally due to high thermal expansion, laser pulses induce negative refractive index changes in the focal zone. However, this expansion leads to an appearance of the shell

of compacted material around the focal zone with positive RIC. This zone is characterized by the reduction of Si–O–Si or Si–O–B angle which demonstrate material compaction. Additionally, we were able to indicate generation of molecular oxygen in these regimes of interaction.

Chapter 9

Conclusions

The work discussed in this dissertation explores how femtosecond laser pulses induce refractive index variation changes in glasses. Specifically, it focuses on investigating structural changes using spatially resolved photoluminescence and Raman spectroscopy in order to analyse the effect of ultrafast writing conditions, such as energy density, pulse duration, accumulated energetic dose, and glass composition. These results are then used to explain the femtosecond laser modification process.

Different regimes of interaction are described producing both isotropic or self-arranged anisotropic refractive index patterns.

Photoinscription procedure

We discussed first the importance of precisely controlling the focusing conditions and indicated regimes of photoinscription mainly governed by thermodynamical mechanisms in fused silica and BK7 glass. There, we identified a variety of irradiation outcomes strongly related to nonlinear propagation effects.

In irradiation of fused silica we have demonstrated that the energy deposition largely determines the structural transitions leading to refractive index changes and optical anisotropies. Smooth type I material changes occur at low density of energy deposition or using short pulse durations. These lead to low-loss ($<$1 dB/cm) waveguides. However, high energy doses and prolonged exposure lead to the self-arrangement of the material in periodic nanolayers in type II regime. These determine lead to particular polarization dependent light transport properties, such as phase retardation between different polarization of transmitted light and anisotropic scattering.

By controlling and tailoring the laser irradiation, the birefringence and

the associated anisotropic light scattering properties characteristic to the ordered nanostructures, polarization sensitive devices can be designed and fabricated. Several polarization functions were demonstrated in the present work including polarization routers and phase retarder (quarter-wave plate).

PL spectroscopy

A main challenge is the characterization of the electronic and atomic structural modifications induced by ultra-short laser pulses. A spectroscopy study was therefore performed on laser-modified fused silica.

It was also observed that three types of luminescent defects were present in the written traces: NBOHC defects with a peak around 650 nm, E'_δ centers with a peak around 545 nm and unknown laser induced defects (LID) with a peak around 530 nm. The study revealed that NBOHC and LID were predominant in many type I static traces and waveguides, and that NBOHC and E'_δ defects were predominant in waveguides fabricated using high laser pulse energies, where birefringence regions were detected. E'_δ centers were equally observed in the regions of void and at high energies of laser pulses.

Additionally, PL study reveals two different regions of NBOHC at early stages of photoinscriptions. The maximum of NBOHC signal was observed in the region that had no visible permanent index changes produced under low energy density of incident irradiation. Concerning the concentration of breaking bonds, it is several times higher in this region than in adjacent area of visible modification.

The 650 nm band excited at 488 nm in the region of void and in the birefringence region of type II traces revels a complex structure of several bands placed 0.11 eV one from the other, indicating on the presence of O_2^- molecules. To our knowledge, such luminescence have been reported for a first time in femtosecond irradiated fused silica. Thus, this finding can be easily applied for molecular oxygen detection with the photoluminescence means. In the present work the ions separation effect, suggested to take place in the region of birefringence and in the voids, obtains support by experimental detection of molecular oxygen in these regions.

We therefore put into evidence a spatial selectivity of defect formation as a function of local energy character. These serves as a marker for type of modification.

Raman spectroscopy

We built up our Raman studies on addressing of the changes in the Raman spectra to the characteristic structural parameters of the fused silica network. These are: interbonding angles θ, interbonding distance r, intertetrahedral angles δ, and rings statistic. The most Raman studies performed on femtosecond-laser irradiated fused silica samples show general trends of densification. The main spectral signatures identifying densification are the decrease of interbonding angles θ, narrowing of dihedral intertetrahedral angles δ distribution and the increase of the amount of three-membered rings. The spectra of modified fused silica, however, depends on the irradiation conditions. Thus, we highlight several regions with different spectral patterns. These are: 1) region of efficient bonds breaking where no refractive index changes happens; 2) region of positive RIC located in the focal region on axis of the laser beam and characterized by changes in ring statistics and angles reduction; 3) densified regions outside the axis of the beam, observed in extreme energetic conditions which are characterized by decrease of interbonding angles with no significant changes in three-fold rings.

Considering differences between traces produced in type I and type II regimes, the results are the following. In type I regime of writing, an increase of three-fold rings and a decrease of interbonding angle were observed. Both these parameters change as a function of pulse energy and pulse number. Regions of lower density observed in the void-like regions or in the birefringent regions for multiple pulse type II traces are characterized by smaller changes of interbonding angle if compare with densified type I regions having the same increase of three membered rings.

Certain of these findings can be applied to other silicate glasses. For example, we observed a decrease in the interbonding angles θ in irradiated BK7 glass in the region of positive RIC, indicating similar

Revised modification mechanisms

From a more fundamental point of view, while the present work reports on significant advances regarding the understanding of the physical processes leading to a bulk modification, questions are still to be addressed. Our findings reveal that simple theories such as fictive temperature model can not be fully applied for characterization of femtosecond laser modified silica. In fact, material reorganization, depending on the focusing and irradiation conditions, is an interplay of thermal, defect-assisted, and pressure compaction mechanisms of densification all with contributions to Δn of 10^{-4} to 10^{-3}.

Consideration of the type I writing regime, where temperature elevation are not sufficient to melt the glassy material, is particularly important from this point of view. We propose that the "cold" densification takes place in this case as a result of defects relaxation. This process starts from bond breaking after self-trapped exciton relaxation. If this process is efficient enough then defect-assisted densification, characterized by the creation of new bonds and material rearrangement, takes place. These modification can be further accumulated due to a repetitive character of interaction between the glassy material and femtosecond laser pulses as the network undergoes modification after each new arriving pulse. The zones with high concentration of NBOHC where no visible RIC and densification signs are considered as a precursors for densification.

Considering type II regime, we propose that the birefringent regions are developing from the nucleation centers by the cumulative action of few hundred of pulses. Voids forming in moderate to tight focusing regimes (NA>0.4) and cracks appearing after local stress release or other density inhomogeneities in loose focusing (NA<0.3) are these nucleation centers.

Perspectives

This investigation provides, thus, key elements in further elucidating of the nature of ultrafast laser induced changes in the bulk of dielectrics. On a fundamental level, other types of experiments are needed to elucidate the mechanisms of densification for example, direct measurements of temperature in the bulk of the silica or Raman spectroscopy performed at ps–μs time scale after pulses arrival in order to observe the structure of silica before resolidification. On such long time-scale the main phenomena should be temporally decoupled, thus, allowing to observe the contribution of each mechanism into the densification.

We equally point out on the certain discrepancies of the simple thermodynamical models to describe phase transformation of fused silica under laser irradiation. Perhaps, a more complex approach based on equation of states should be considered to accurately describe existing non-equilibrium phase of fused silica in the temperature region below or near the softening point and pressures below the GPa.

Considering a practical aspect of the work, we indicated the conditions favoring the birefringence development under femtosecond laser irradiated silica. We equally demonstrated that birefringence properties can be monitored by diffraction of light occurring due to refractive index modulation. Appropriate light for diffraction can be generated *in situ* during writing as the

third harmonics of the fundamental writing wavelength appears due to the nonlinear mechanisms, or injected from outside. This allow real-time probing of the onset of an anisotropic nanoscale modification. Thus, tailoring and control of the birefringence properties by the pulse shaping apparatus and varying the accumulation dose during writing procedure can be performed, that is important in polarization sensitive devices fabrication.

Bibliography

[ADS+94] P. Audebert, Ph. Daguzan, A. Dos Santos, J. C. Gauthier, J. P. Geindre, S. Guizard, G. Hamoniaux, K. Krastev, P. Martin, G. Petite, and A. Antonetti. *Space-time observation of an electron gas in SiO_2.* Physical Review Letters, **73**(14):1990–1993, 1994.

[AK03] K. Awazu and H. Kawazoe. *Strained Si–O–Si bonds in amorphous SiO_2 materials: A family member of active centers in radio, photo, and chemical responses.* Journal of Applied Physics, **94**(10):6243–6262, 2003.

[AKM+91] K. Awazu, H. Kawazoe, K. Muta, T. Ibuki, K. Tabayashi, and K. Shobatake. *Characterization of silica glasses sintered under Cl_2 ambients.* Journal of Applied Physics, **69**(4):1849–1852, 1991.

[Awa04] K. Awazu. *Ablation and compaction of amorphous SiO_2 irradiated with ArF excimer laser.* Journal of Non-Crystalline Solids, **337**(3):241–253, 2004.

[Bat74] J. B. Bates. *Neutron irradiation effects and structure of noncrystalline SiO_2.* The Journal of Chemical Physics, **61**(10):4163–4176, 1974.

[Bau77] W. H. Baur. *Silicon–oxygen bond lengths, bridging angles Si–O–Si and synthetic low tridymite.* Acta Crystallographica B, **33**:2615–2619, 1977.

[BBS+07] I. M. Burakov, N. M. Bulgakova, R. Stoian, A. Mermillod-Blondin, E. Audouard, A. Rosenfeld, A. Husakou, and I. V. Hertel. *Spatial distribution of refractive index variations induced in bulk fused silica by single ultrashort and short laser pulses.* Journal of Applied Physics, **101**(4):043506, 2007.

[BBS+08] Y. Bellouard, E. Barthel, A. A. Said, M. Dugan, and P. Bado. *Scanning thermal microscopy and Raman analysis of bulk fused silica exposed to low energy femtosecond laser pulses.* Optics Express, **16**(24):19520–19534, 2008.

[BCJL68] N. Bloembergen, R. K. Chang, S. S. Jha, and C. H. Lee. *Optical second-harmonic generation in reflection from media with inversion symmetry.* Physical Review, **174**(3):813–822, 1968.

[BdLG+11] L. Bressel, D. de Ligny, E.G. Gamaly, A.V. Rode, and S. Juodkazis. *Observation of O_2 inside voids formed in GeO_2 glass by tightly-focused fs-laser pulses.* Optical Materials Express, **1**(6):1150–1157, 2011.

[BGL+08] J. Burgin, C. Guillon, P. Langot, F. Vallée, B. Hehlen, and M. Foret. *Vibrational modes and local order in permanently densified silica glasses: Femtosecond and Raman spectroscopy study.* Physical Review B, **78**(18):184203, 2008.

[BGME93] R. A. Barrio, F. L. Galeener, E. Martínez, and R. J. Elliott. *Regular ring dynamics in AX_2 tetrahedral glasses.* Physical Review B, **48**(21):15672, 1993.

[Boy07] R. W. Boyd. *Nonlinear optics.* Academic Press, 2007.

[BPG+99] B. Boizot, G. Petite, D. Ghaleb, B. Reynard, and G. Calas. *Raman study of β-irradiated glasses.* Journal of Non-Crystalline Solids, **243**(2–3):268–272, 1999.

[Bri76] T.W. Bril. *Raman spectroscopy of crystalline and vitreous borates.* PhD thesis, Technological University Eindhoven, 1976.

[Bru70] R. Brueckner. *Properties and structure of vitreous silica. I.* Journal of Non-Crystalline Solids, **5**:123–175, 1970.

[Bru71] R. Brueckner. *Properties and structure of vitreous silica. II.* Journal of Non-Crystalline Solids, **5**:177–216, 1971.

[BS70] M. J. W. Boness and G. J. Schulz. *Structure of O_2.* Physical Review A, **2**(6):2182–2186, 1970.

[BSC+05] V. R. Bhardwaj, E. Simova, P. B. Corkum, D. M. Rayner, C. Hnatovsky, R. S. Taylor, B. Schreder, M. Kluge, and

J. Zimmer. *Femtosecond laser-induced refractive index modification in multicomponent glasses*. Journal of Applied Physics, **97**(8):083102, 2005.

[BSR+06] V. R. Bhardwaj, E. Simova, P. P. Rajeev, C. Hnatovsky, R. S. Taylor, D. M. Rayner, and P. B. Corkum. *Optically produced arrays of planar nanostructures inside fused silica*. Physical Review Letters, **96**:057404, 2006.

[BSR10] N. M. Bulgakova, R. Stoian, and A. Rosenfeld. *Laser-induced modification of transparent crystals and glasses*. Quantum Electronics, **40**(11):966–985, 2010.

[BTH+88] B. C. Bunker, D. R. Tallant, T. J. Headley, G. L. Turner, and R. J. Kirkpatrick. *The structure of leached sodium borosilicate glass*. Physics and chemistry of glasses, **29**(3):106–120, 1988.

[Bus07] G. Buscarino. *Experimental investigation on the microscopic structure of intrinsic paramagnetic point defects in amorphous silicon dioxide*. PhD thesis, University of Palermo, 2007.

[BW05] M. Born and E. Wolf. *Principles of Optics*. Cambridge University Press, 2005.

[Car82] M. Cardona. Resonance phenomena. In *Light Scattering in Solids II* edited by M. Cardona and G. Güntherodt, vol. 50 of *Topics in Applied Physics*, pp. 19–178. Springer Berlin / Heidelberg, 1982.

[CCB00] J.R. Chelikowsky, D. J. Chadi, and N. Binggeli. *Oxygen configurations in silica*. Physical Review B, **62**(4):R2251–R2254, 2000.

[CG83] M. Cardona and G. Güntherodt. *Light Scattering in Solids I*, vol. 8 of *Topics in Applied Physics*. Springer Berlin / Heidelberg, 1983.

[CHRK03] J.W. Chan, T.R. Huser, S.H. Risbud, and D.M. Krol. *Modification of the fused silica glass network associated with waveguide fabrication using femtosecond laser pulses*. Applied Physics A, **76**(3):367–372, 2003.

[CLC+11] J. Canning, M. Lancry, K. Cook, A. Weickman, F. Brisset, and B. Poumellec. *Anatomy of a femtosecond laser processed silica waveguide*. Optical Materials Express, **1**(5):998–1008, 2011.

[CMM+09] G. Cheng, K. Mishchik, C. Mauclair, E. Audouard, and R. Stoian. *Ultrafast laser photoinscription of polarization sensitive devices in bulk silica glass.* Optics Express, **17**(12):9515–9525, 2009.

[Coh] Coherent. *Operator's manual RegA model 9000 laser.*

[CS77] J. R. Chelikowsky and M. Schlüter. *Electron states in α-quartz: A self-consistent pseudopotential calculation.* Physical Review B, **15**(8):4020–4029, 1977.

[CSF+05] A. Couairon, L. Sudrie, M. Franco, B. Prade, and A. Mysyrowicz. *Filamentation and damage in fused silica induced by tightly focused femtosecond laser pulses.* Physical Review B, **71**:125435, 2005.

[CTRK01] J.W. Chan, T.Huser, S. Risbud, and D.M. Krol. *Structural changes in fused silica after exposure to focused femtosecond laser pulses.* Optics Letters, **26**(21):1726–1728, 2001.

[CXW05] I. H. Chowdhury, X. Xu, and A. M. Weiner. *Ultrafast double-pulse ablation of fused silica.* Applied Physics Letters, **86**(15):151110, 2005.

[DBA90] E. Duval, A. Boukenter, and T. Achibat. *Vibrational dynamics and the structure of glasses.* Journal of Physics: Condensed Matter, **2**(51):10227–10234, 1990.

[DBX83] W.J. Dell, P.J. Bray, and S.Z. Xiao. *^{11}B NMR studies and structural modeling of $Na_2O{\cdot}B_2O_3{\cdot}SiO_2$ glasses of high soda content.* Journal of Non-Crystalline Solids, **58**(1):1–16, 1983.

[DD96] L. Douillard and J. P. Duraud. *Amorphization of α-quartz under irradiation.* Journal de Physique III, **6**(12):1677–1687, 1996.

[DeL80] J.A. DeLuca. *An introduction to luminescence in inorganic solids.* Journal of Chemical Education, **57**(8):541–545, 1980.

[dG02] P.-G. de Gennes. *A simple picture for structural glasses.* Comptes Rendus Physique, **3**(9):1263–1268, 2002.

[DMSH96] K. M. Davis, K. Miura, N. Sugimoto, and K. Hirao. *Writing waveguides in glass with a femtosecond laser.* Optics Letters, **21**(21):1729–1731, 1996.

[Dol65] W. A. Dollase. *Reinvestigation of the structure of low cristobalite*. Zeitschrift für Kristallographie, **121**(5):369–377, 1965.

[Dol66] W. A. Dollase. *The crystal structures of some phases of silica*. PhD thesis, Massachusetts Institute of Technology, 1966.

[DP94] R. T. Downs and D. C. Palmer. *The pressure behaviour of α–crystobalite*. American Mineralogist, **79**(1–2):9–14, 1994.

[DR06] J.-C. Diels and W. Rudolph. *Ultrashort laser pulse phenomena*. Academic Press, 2006.

[DVTO+07] G. Della Valle, S. Taccheo, R. Osellame, A. Festa, G. Cerullo, and P. Laporta. *1.5 μm single longitudinal mode waveguide laser fabricated by femtosecond laser writing*. Optics Express, **15**(6):3190–3194, 2007.

[EF82] A. H. Edwards and B. W. Fowler. *Theory of the peroxy-radical defect in a-SiO_2*. Physical Review B, **26**(12):6649–6660, 1982.

[Exa84] G.J. Exarhos. *Vibrational Raman studies of particle induced damage in oxide glasses*. Nuclear Instruments and Methods in Physics Research B, **1**(2-3):498–502, 1984.

[EZN+08] S.M. Eaton, H. Zhang, M.L. Ng, J. Li, W.-J. Chen, S. Ho, and P.R. Herman. *Transition from thermal diffusion to heat accumulation in high repetition rate femtosecond laser writing of buried optical waveguides*. Optics Express, **16**(13):9443–9458, 2008.

[FBT+02] H.-J. Fitting, T. Barfels, A.N. Trukhin, B. Schmidt, A. Gulans, and A. von Czarnowski. *Cathodoluminescence of Ge^+, Si^+, and O^+ implanted SiO_2 layers and the role of mobile oxygen in defect transformations*. Journal of Non-Crystalline Solids, **303**(2):218–231, 2002.

[FGSW79] E. J. Friebele, D. L. Griscom, M. Stapelbroek, and R. A. Weeks. *Fundamental defect centers in glass: The peroxy radical in irradiated high-purity fused silica*. Physical Review Letters, **42**(20):1346–1349, 1979.

[FH88] E. J. Friebele and P. L. Higby. Radiation effects in amorphous SiO_2 for windows and mirror substrates. In *Laser induced damage in optical materials:1987* edited by H. E. Banett *et al.*, pp. 89–97. ASTM International, 1988.

[FHS90] A. J. Fisher, W. Hayes, and A. M. Stoneham. *Structure of the self-trapped exciton in quartz.* Physical Review Letters, **64**(22):2667–2670, 1990.

[FSS07] H.-J. Fitting, R. Salh, and B. Schmidt. *Multimodal electronic–vibronic spectra of luminescence in ion-implanted silica layers.* Journal of Luminescence, **122–123**:743–746, 2007.

[FW81] T. Furukawa and W.B. White. *Raman spectroscopic investigation of sodium borosilicate glass structure.* Journal of Materials Science, **16**(10):2689–2700, 1981.

[FWT+11] L.B. Fletcher, J.J. Witcher, N. Troy, S.T. Reis, R.K. Brow, R. Martinez Vazquez, R. Osellame, and D.M. Krol. *Femtosecond laser writing of waveguides in zinc phosphate glasses.* Optical Materials Express, **1**(5):845–855, 2011.

[GAG+01] A. V. Gomonnai, Yu. M. Azhniuk, D. B. Goyer, I. G. Megela, and V. V. Lopushansky. *Optical studies of alkali borosilicate glass irradiated with high-energy electrons.* Journal of Optoelectronics and Advanced Materials, **3**(1):37–44, 2001.

[Gal79] F. L. Galeener. *Band limits and the vibrational spectra of tetrahedral glasses.* Physical Review B, **19**(8):4292–4297, 1979.

[GBME84] F. L. Galeener, R. A. Barrio, E. Martinez, and R. J. Elliott. *Vibrational decoupling of rings in amorphous solids.* Physical Review Letters, **53**(25):2429–2432, 1984.

[GF86] D. L. Griscom and E. J. Friebele. *Fundamental radiation-induced defect centers in synthetic fused silicas: Atomic chlorine, delocalized E' centers, and a triplet state.* Physical Review B, **34**(11):7524–7533, 1986.

[GG83a] F. L. Galeener and A. E. Geissberger. *Vibrational dynamics in ^{30}Si-substituted vitreous SiO_2.* Physical Review B, **27**(10):6199–6204, 1983.

[GG83b] A. E. Geissberger and F. L. Galeener. *Raman studies of vitreous SiO_2 versus fictive temperature.* Physical Review B, **28**(6):3266–3271, 1983.

[GGL+10] D. Grojo, M. Gertsvolf, S. Lei, T. Barillot, D. M. Rayner, and P. B. Corkum. *Exciton-seeded multiphoton ionization in bulk SiO_2.* Physical Review B, **81**(21):212301, 2010.

[GJN+06] E.G. Gamaly, S. Juodkazis, K. Nishimura, H. Misawa, B. Luther-Davies, L. Hallo, P. Nicolai, and V.T. Tikhonchuk. *Laser-matter interaction in the bulk of a transparent solid: Confined microexplosion and void formation.* Physical Review B, **73**:214101, 2006.

[GL76] F. L. Galeener and G. Lucovsky. *Longitudinal optical vibrations in glasses: GeO_2 and SiO_2.* Physical Review Letters, **37**(22):1474–1478, 1976.

[GLS+04] L. N. Gaier, M. Lein, M. I. Stockman, P. L. Knight, P. B. Corkum, M. Yu. Ivanov, and G. L. Yudin. *Ultrafast multiphoton forest fires and fractals in clusters and dielectrics.* Journal of Physics B, **37**(3):L57–L67, 2004.

[GM97] E. N. Glezer and E. Mazur. *Ultrafast-laser driven micro-explosions in transparent materials.* Applied Physics Letters, **71**(7):882–884, 1997.

[GM98] D. L. Griscom and M. Mizuguchi. *Determination of the visible range optical absorption spectrum of peroxy radicals in gamma-irradiated fused silica.* Journal of Non-Crystalline Solids, **239**(1–3):66–77, 1998.

[GM08] R. R. Gattass and E. Mazur. *Femtosecond laser micromachining in transparent materials.* Nature Photonics, **2**(4):219–225, 2008.

[GMP+96] S. Guizard, P. Martin, G. Petite, P. D'Oliveira, and P. Meynadier. *Time-resolved study of laser-induced colour centres in SiO_2.* Journal of Physics: Condensed Matter, **8**(9):1281–1290, 1996.

[Gra67] R. W. Grant. *New data on tridymite.* American Mineralogist, **52**(3–4):536–541, 1967.

[Gra01] H. Graetsch. *X-ray powder diffraction study on the modulated high temperature forms of SiO_2 tridymite between 110 and 220 °C.* Physics and Chemistry of Minerals, **28**(5):313–321, 2001.

[GRD08] D. Giordano, J.K. Russell, and D.B. Dingwell. *Viscosity of magmatic liquids: A model.* Earth and Planetary Science Letters, **271**(1-4):123–134, 2008.

[Gri91] D. L. Griscom. *Optical properties and structure of defects in silica glass.* Journal of the Ceramic Society of Japan, **99**(1154):923–942, 1991.

[Gri00] D. L. Griscom. The natures of point defects in amorphous silicon dioxide. In *Defects in SiO_2 and related dielectrics: science and technology* edited by G. Pacchioni, L. Skuja, and D. L. Griscom, pp. 117–159. Springer, 2000.

[Gru07] V. E. Gruzdev. *Photoionization rate in wide band-gap crystals.* Physical Review B, **75**(20):205106, 2007.

[GS78] F. L. Galeener and P. N. Sen. *Theory for the first-order vibrational spectra of disordered solids.* Physical Review B, **17**:1928–1933, 1978.

[HBT+07] L. Hallo, A. Bourgeade, V. T. Tikhonchuk, C. Mezel, and J. Breil. *Model and numerical simulations of the propagation and absorption of a short laser pulse in a transparent dielectric material: Blast-wave launch and cavity formation.* Physical Review B, **76**(2):024101, 2007.

[Hea94] P. J. Heaney. *Silica: Physical behavior, geochemistry & materials applications.* Mineralogical Society of America, 1994.

[HG91] D. M. Hatch and S. Ghose. *The α-β phase transition in cristobalite, SiO_2.* Physics and Chemistry of Minerals, **17**(6):554–562, 1991.

[HM98] K. Hirao and K. Miura. *Writing waveguides and gratings in silica and related materials by a femtosecond laser.* Journal of Non-Crystalline Solids, **239**(1-3):91–95, 1998.

[HMBM86] R. J. Hemley, H. K. Mao, P. M. Bell, and B. O. Mysen. *Raman spectroscopy of SiO_2 glass at high pressure.* Physical Review Letters, **57**(6):747–750, 1986.

[HP01] P. J. Heaney and J. E. Post. *Evidence for an $I2/a$ to $Imab$ phase transition in the silica polymorph moganite at $\sim$570 K.* American Mineralogist, **86**(11–12):1358–1366, 2001.

[HTS+05] C. Hnatovsky, R. S Taylor, E. Simova, V. R Bhardwaj, D. M Rayner, and P. B Corkum. *High-resolution study of photoinduced modification in fused silica produced by a tightly focused*

femtosecond laser beam in the presence of aberrations. Journal of Applied Physics, **98**(1):013517, 2005.

[IWNS06] K. Itoh, W. Watanabe, S. Nolte, and C. B. Schaffer. *Ultrafast processes for bulk modification of transparent materials.* MRS Bulletin, **31**(8):620–625, 2006.

[JGM+92] W. Joosen, S. Guizard, P. Martin, G. Petite, P. Agostini, A. Dos Santos, G. Grillon, D. Hulin, A. Migus, and A. Antonetti. *Femtosecond multiphoton generation of the self-trapped exciton in α-SiO_2.* Applied Physics Letters, **61**(19):2260–2262, 1992.

[JRG+03] S. Juodkazis, A.V. Rode, E.G. Gamaly, S. Matsuo, and H. Misawa. *Recording and reading of three-dimensional optical memory in glasses.* Applied Physics B, **77**:361–368, 2003.

[KD03] S. O. Kucheyev and S. G. Demos. *Optical defects produced in fused silica during laser-induced breakdown.* Applied Physics Letters, **82**:3230–3232, 2003.

[Kea54] P. P. Keat. *A new crystalline silica.* Science, **120**(3113):328–330, 1954.

[Kel58] L. V. Keldysh. *Behavior of non-metallic crystals in strong electric fields.* Soviet Physics JETP, **6**(4):763–770, 1958.

[Kel65] L. V. Keldysh. *Ionization in the field of a strong electromagnetic wave.* Soviet Physics JETP, **20**(5):1307–1314, 1965.

[KH94] K. J. Kingma and R. J. Hemley. *Raman spectroscopic study of microcrystalline silica.* American Mineralogist, **79**(3–4):269–273, 1994.

[KHSH05] K. Kajihara, M. Hirano, L. Skuja, and H. Hosono. *Reactions of SiCl groups in amorphous SiO_2 with mobile interstitial chemical species: Formation of interstitial Cl_2 and HCl molecules, and role of interstitial H_2O molecules.* Journal of Applied Physics, **98**(4):043515, 2005.

[Kih90] K. Kihara. *An X-ray study of the temperature dependence of the quartz structure.* European Journal of Mineralogy, **2**(1):63–77, 1990.

[Kit53] C. Kittel. *Introduction to solid state physics*. Wiley: New York, 1953.

[KKH+05] K. Kajihara, H. Kamioka, M. Hirano, T. Miura, L. Skuja, and H. Hosono. *Interstitial oxygen molecules in amorphous SiO_2. III. measurements of dissolution kinetics, diffusion coefficient, and solubility by infrared photoluminescence*. Journal of Applied Physics, **98**(1):013529, 2005.

[KKP+00] S. P. Karna, H. A. Kurtz, A. C. Pineda, W. M. Shedd, and R. D. Pugh. Point defects in Si–SiO_2 systems: current understanding. In *Defects in SiO_2 and related dielectrics: science and technology* edited by G. Pacchioni, L. Skuja, and D. L. Griscom, pp. 599–615. Springer, 2000.

[Kon75] W.L. Konijnendijk. *The structure of borosilicate glasses*. PhD thesis, Technological University Eindhoven, 1975.

[KRVS00] A. Kaiser, B. Rethfeld, M. Vicanek, and G. Simon. *Microscopic processes in dielectrics under irradiation by subpicosecond laser pulses*. Physical Review B, **61**(17):11437–11450, 2000.

[KS75] W.L. Konijnendijk and J.M. Stevels. *The structure of borate glasses studied by Raman scattering*. Journal of Non-Crystalline Solids, **18**(3):307–331, 1975.

[KS08] P. G. Kazansky and Yasuhiko Shimotsuma. *Self-assembled sub-wavelength structures and form birefringence created by femtosecond laser writing in glass: properties and applications*. Journal of the Ceramic Society of Japan, **116**(1358):1052–1062, 2008.

[LAG+11] D. J. Little, M. Ams, S. Gross, P. Dekker, Ch. T. Miese, A. Fuerbach, and M. J. Withford. *Structural changes in BK7 glass upon exposure to femtosecond laser pulses*. Journal of Raman Spectroscopy, **42**(4):715–718, 2011.

[Lin87] M. Lines. *Absolute Raman intensities in glasses I. Theory*. Journal of Non-Crystalline Solids, **89**:143–162, 1987.

[Lit09] D. J. Little. *Glass modification in femtosecond laser written waveguides and the effect of laser polarisation*. PhD thesis, Macqarie University, 2009.

[LJ77] R. B. Laughlin and J. D. Joannopoulos. *Phonons in amorphous silica*. Physical Review B, **16**(6):2942–2952, 1977.

[LL75] L. D. Landau and E. M. Lifshitz. *The classical theory of fields*. Butterworth-Heinemann, 1975.

[LL84] L. D. Landau and E. M. Lifshitz. *Electrodynamics of continuous media*. Pergamon Press, 1984.

[LM03] M. Lazzeri and F. Mauri. *First-principles calculation of vibrational Raman spectra in large systems: Signature of small rings in crystalline SiO_2*. Physical Review Letters, **90**(3):036401, 2003.

[LMG02] F. Ladieu, Ph. Martin, and S. Guizard. *Measuring thermal effects in femtosecond laser-induced breakdown of dielectrics*. Applied Physics Letters, **81**(6):957–959, 2002.

[LP81] L. Levien and C. T. Prewitt. *High-pressure crystal structure and compressibility of coesite*. American Mineralogist, **66**(3–4):324–333, 1981.

[LP02] R. Le Parc. *Diffusion de rayonnements et relaxation structurale dans les préformes de fibres optiques et les verres de silice*. PhD thesis, Université Claude Bernard – Lyon I, 2002.

[LPW80] L. Levien, C. T. Prewitt, and D. J. Weidner. *Structure and elastic properties of quartz at pressure*. American Mineralogist, **65**(9–10):920–930, 1980.

[LSB06] D. L. Lakshtanov, S. V. Sinogeikin, and J. D. Bass. *High-temperature phase transitions and elasticity of silica polymorphs*. Physics and Chemistry of Minerals, **34**(1):11–22, 2006.

[LSH83] A. Lehmann, L. Schumann, and K. Hübner. *Optical phonons in amorphous silicon oxides. I. Calculation of the density of states and interpretation of LO–TO splittings of amorphous SiO_2*. physica status solidi (b), **117**(2):689–698, 1983.

[Mau10] C. Mauclair. *Spatio-temporal ultrafast laser tailoring for bulk functionalization of transparent materials*. PhD thesis, Université Jean Monnet, 2010.

[MB83] L. McCaughan and E. Bergmann. *Index distribution of optical waveguides from their mode profile.* Journal of Lightwave Technology, **1**(1):241–244, 1983.

[MB07] A. Mermillod-Blondin. *Analysis and optimization of ultrafast laser-induced bulk modifications in dielectric materials.* PhD thesis, Université Jean Monnet, 2007.

[MBM+08] A. Mermillod-Blondin, I. M. Burakov, Yu. P. Meshcheryakov, N. M. Bulgakova, E. Audouard, A. Rosenfeld, A. Husakou, I. V. Hertel, and R. Stoian. *Flipping the sign of refractive index changes in ultrafast and temporally shaped laser-irradiated borosilicate crown optical glass at high repetition rates.* Physical Review B, **77**(10):104205, 2008.

[MBR+09] A. Mermillod-Blondin, J. Bonse, A. Rosenfeld, I. V. Hertel, Yu. P. Meshcheryakov, N. M. Bulgakova, E. Audouard, and R. Stoian. *Dynamics of femtosecond laser induced voidlike structures in fused silica.* Applied Physics Letters, **94**(4):041911, 2009.

[MC96] I. Mansour and F. Caccavale. *An improved procedure to calculate the refractive index profile from the measured near-field intensity.* Journal of Lightwave Technology, **14**(3):423–428, 1996.

[MCH+10] K. Mishchik, G. Cheng, G. Huo, I. M. Burakov, C. Mauclair, A. Mermillod-Blondin, A. Rosenfeld, Y. Ouerdane, A. Boukenter, O. Parriaux, and R. Stoian. *Nanosize structural modifications with polarization functions in ultrafast laserirradiated bulk fused silica.* Optics Express, **18**(24):24809–24824, 2010.

[McM84] P. F. McMillan. *Structural studies of silicate glasses and melts. applications and limitations of Raman spectroscopy.* American Mineralogist, **69**(7–8):622–644, 1984.

[MGD+97] P. Martin, S. Guizard, Ph. Daguzan, G. Petite, P. D'Oliveira, P. Meynadier, and M. Perdrix. *Subpicosecond study of carrier trapping dynamics in wide-band-gap crystals.* Physical Review B, **55**(9):5799–5810, 1997.

[MGN09] D. Manara, A. Grandjean, and D.R. Neuville. *Structure of borosilicate glasses and melts: A revision of the Yun, Bray and Dell model.* Journal of Non-Crystalline Solids, **355**(50-51):2528–2531, 2009.

[min] Mindat.org - the mineral and locality database.

[MMBH+08] C. Mauclair, A. Mermillod-Blondin, N. Huot, E. Audouard, and R. Stoian. *Ultrafast laser writing of homogeneous longitudinal waveguides in glasses using dynamic wavefront correction.* Optics Express, **16**(8):5481–5492, 2008.

[MR86] P. F. McMillan and R.L. Remmele. *Hydroxyl sites in SiO_2 glass; a note on infrared and Raman spectra.* American Mineralogist, **71**(5–6):772–778, 1986.

[MSH66] J.H. Mackey, H.L. Smith, and A. Halperin. *Optical studies in X-irradiated high purity sodium silicate glasses.* Journal of Physics and Chemistry of Solids, **27**(11–12):1759–1772, 1966.

[MVC+10] M. J. Matthews, R. M. Vignes, D. Cooke, S. T. Yang, and J. S. Stolken. *Analysis of microstructural relaxation phenomena in laser-modified fused silica using confocal Raman microscopy.* Optics Letters, **35**(9):1311–1313, 2010.

[MW69] R. L. Mozzi and B. E. Warren. *The structure of vitreous silica.* Journal of Applied Crystallography, **2**:164–172, 1969.

[Nak09] K. Nakamoto. *Infrared and Raman spectra of inorganic and coordination compounds.* Wiley, 2009.

[NG80] M. D. Newton and G. V. Gibbs. *Ab initio calculated geometries and charge distributions for H_4SiO_4 and $H_6Si_2O_7$ compared with experimental values for silicates and siloxanes.* Physics and Chemistry of Minerals, **6**:221–246, 1980.

[NGM85] V. Nathan, A. H. Guenther, and S. S. Mitra. *Review of multiphoton absorption in crystalline solids.* Journal of the Optical Society of America B, **2**(2):294–316, 1985.

[NTO+89] H. Nishikawa, R. Tohmon, Y. Ohki, K. Nagasawa, and Y. Hama. *Defects and optical absorption bands induced by surplus oxygen in high-purity synthetic silica.* Journal of Applied Physics, **65**(12):4672–4678, 1989.

[NWI+96] H. Nishikawa, E. Watanabe, D. Ito, Y. Sakurai, K. Nagasawa, and Y. Ohki. *Visible photoluminescence from Si clusters in γ-irradiated amorphous SiO_2.* Journal of Applied Physics, **80**(6):3513–3517, 1996.

[OR83] E. O'Reilly and J. Robertson. *Theory of defects in vitreous silicon dioxide*. Physical Review B, **27**(6):3780–3795, 1983.

[ORS+99] M. Okuno, B. Reynard, Y. Shimada, Y. Syono, and C. Willaime. *A Raman spectroscopic study of shock-wave densification of vitreous silica*. Physics and Chemistry of Minerals, **26**(4):304–311, 1999.

[Pau60] L. Pauling. *The nature of the chemical bond and the structure of molecules and crystals*. Cornell University Press, 1960.

[PC98] A. Pasquarello and R. Car. *Identification of Raman defect lines as signatures of ring structures in vitreous silica*. Physical Review Letters, **80**(23):5145–5147, 1998.

[PDGM96] G. Petite, Ph. Daguzan, S. Guizard, and P. Martin. *Conduction electrons in wide-bandgap oxides: a subpicosecond time-resolved optical study*. Nuclear Instruments and Methods in Physics Research B, **107**(1–4):97–101, 1996.

[Pea73] D. R. Peacor. *High-temperature single-crystal study of the cristobalite inversion*. Zeitschrift für Kristallographie, **138**(1–4):274–298, 1973.

[PI98] G. Pacchioni and G. Ierano. *Ab initio theory of optical transitions of point defects in SiO_2*. Physical Review B, **57**(2):818–832, 1998.

[PMB+11] K. I. Popov, C. McElcheran, K. Briggs, S. Mack, and L. Ramunno. *Morphology of femtosecond laser modification of bulk dielectrics*. Optics Express, **19**(1):271–282, 2011.

[Pri58] W. Primak. *Fast-neutron-induced changes in quartz and vitreous silica*. Physical Review, **110**(6):1240–1254, 1958.

[Pri72] W. Primak. *Mechanism for the radiation compaction of vitreous silica*. Journal of Applied Physics, **43**(6):2745–2754, 1972.

[PSS08] C.W. Ponader, J.F. Schroeder, and A.M. Streltsov. *Origin of the refractive-index increase in laser-written waveguides in glasses*. Journal of Applied Physics, **103**(6):063516, 2008.

[PT11] D. G. Papazoglou and S. Tzortzakis. *Physical mechanisms of fused silica restructuring and densification after femtosecond laser excitation*. Optical Materials Express, **1**(4):625–632, 2011.

[QGM+99] F. Quere, S. Guizard, P. Martin, G. Petite, O. Gobert, P. Meynadier, and M. Perdrix. *Ultrafast carrier dynamics in laser-excited materials: subpicosecond optical studies.* Applied Physics B, **68**:459–463, 1999.

[RCS+07] W.J. Reichman, J.W. Chan, C.W. Smelser, S.J. Mihailov, and D.M. Krol. *Spectroscopic characterization of different femtosecond laser modification regimes in fused silica.* Journal of the Optical Society of America B, **24**(7):1627–1632, 2007.

[Rei06] W.J. Reichman. *Understanding how femtosecond laser waveguide fabrication in glasses works.* PhD thesis, University of California, 2006.

[Ret04] B. Rethfeld. *Unified model for the free-electron avalanche in laser-irradiated dielectrics.* Physical Review Letters, **92**(18):187401, 2004.

[Rit56] H. N. Ritland. *Limitations of the fictive temperature concept.* Journal of the American Ceramic Society, **39**(12):403–406, 1956.

[RKS+06] W.J. Reichman, D.M. Krol, L. Shah, F. Yoshino, A. Arai, S.M. Eaton, and P.R. Herman. *A spectroscopic comparison of femtosecond-laser-modified fused silica using kilohertz and megahertz laser systems.* Journal of Applied Physics, **99**(12):123112, 2006.

[RL+99] A. Rosenfeld, M. Lorenz, , R. Stoian, and D. Ashkenasi. *Ultrashort-laser-pulse damage threshold of transparent materials and the role of incubation.* Applied Physics A, **69**:S373–S376, 1999.

[RLK61] J. Rolfe, F. R. Lipsett, and W. J. King. *Optical absorption and fluorescence of oxygen in alkali halide crystals.* Physical Review, **123**(2):447–454, 1961.

[Rol79] J. Rolfe. *First excited state of the O_2^- ion.* The Journal of Chemical Physics, **70**(5):2463–2465, 1979.

[San05] N. Sanner. *Mise en forme programmable de faisceau laser femtoseconde pour le micro-usinage et la photoinscription de guides d'ondes.* PhD thesis, Université Jean Monnet, 2005.

[SB02] A.M. Streltsov and N.F. Borrelli. *Study of femtosecond-laser-written waveguides in glasses.* Journal of Optic Society of America B, **19**(10):2496–2504, 2002.

[SBWH10] R. Stoian, T. Baumert, A. Wollenhaupt, and V. I. Hertel. Pulse shaping in laser material processing. In *Laser Precision Microfabrication* edited by M. Meunier A. Piqué K. Sugioka, pp. 121–144. Springer, 2010.

[SCF+02] L. Sudrie, A. Couairon, M. Franco, B. Lamouroux, B. Prade, S. Tzortzakis, and A. Mysyrowicz. *Femtosecond laser-induced damage and filamentary propagation in fused silica.* Physical Review Letters, **89**(18):186601, 2002.

[SCS62] C. B. Sclar, L. C. Carrison, and C. M. Schwartz. *Optical crystallography of coesite.* American Mineralogist, **47**(11-12):1292–1302, 1962.

[SG70] R. Shuker and R. W. Gammon. *Raman-scattering selection-rule breaking and the density of states in amorphous materials.* Physical Review Letters, **25**:222–225, 1970.

[SG93] P. N. Saeta and B. I. Greene. *Primary relaxation processes at the band edge of SiO_2.* Physical Review Letters, **70**(23):3588–3591, 1993.

[She04] J. Shelby. *Density of vitreous silica.* Journal of Non-Crystalline Solids, **349**:331–336, 2004.

[SHHK05] L. Skuja, M. Hirano, H. Hosono, and K. Kajihara. *Defects in oxide glasses.* physica status solidi (c), **2**(1):15–24, 2005.

[SI12] N. Shcheblanov and T. Itina. *Femtosecond laser interactions with dielectric materials: insights of a detailed modeling of electronic excitation and relaxation processes.* Applied Physics A, 2012.

[SKQH03] Y. Shimotsuma, P.G. Kazansky, J. Qiu, and K. Hirao. *Self-organized nanogratings in glass irradiated by ultrashort light pulses.* Physical Review Letters, **91**:247405, 2003.

[Sku98] L. Skuja. *Optically active oxygen-deficiency-related centers in amorphous silicon dioxide.* Journal of Non-Crystalline Solids, **239**(1–3):16–48, 1998.

[Sku00] L. Skuja. Optical properties of defects in silica. In *Defects in SiO_2 and related dielectrics: science and technology* edited by G. Pacchioni, L. Skuja, and D. L. Griscom, pp. 73–116. Springer, 2000.

[Sku01] L. Skuja. Laser-induced color centers in silica. In *Proceedings of SPIE*, vol. 4347, pp. 155–168, 2001.

[SKV59] J. Shropshire, P. P. Keat, and P. A. Vaughan. *The crystal structure of keatite, a new form of silica.* Zeitschrift für Kristallographie, **112**(1–6):409–413, 1959.

[SMM+05] P. Sushko, S. Mukhopadhyay, A. Mysovsky, V. Sulimov, A. Taga, and A. Shluger. *Structure and properties of defects in amorphous silica: new insights from embedded cluster calculations.* Journal of Physics: Condensed Matter, **17**(21):S2115–S2140, 2005.

[SMN81] S. K. Sharma, J. F. Mammone, and M. F. Nicol. *Raman investigation of ring configurations in vitreous silica.* Nature, **292**:140–141, 1981.

[SN99] Y. Sakurai and K. Nagasawa. *Green photoluminescence band in γ-irradiated oxygen-surplus silica glass.* Journal of Applied Physics, **86**(3):1377–1381, 1999.

[SO97] R.E. Schenker and W. G. Oldham. *Ultraviolet-induced densification in fused silica.* Journal of Applied Physics, **82**(3):1065–1071, 1997.

[Sol] J. Solis. Private communications.

[Sos29a] R. B. Sosman. Electrical and optical properties of silica. In *International critical tables of numerical data, physics, chemistry and technology* edited by E. W. Washburn, vol. 6, pp. 341–344. McGraw-Hill, 1929.

[Sos29b] R. B. Sosman. Mechanical and thermal properties of the various forms of silica. In *International critical tables of numerical data, physics, chemistry and technology* edited by E. W. Washburn, vol. 3, pp. 19–22. McGraw-Hill, 1929.

[Sos65] R. B. Sosman. *The phases of silica.* Rutgers University Press, 1965.

[SS90] A. Shluger and E. Stefanovich. *Models of the self-trapped exciton and nearest-neighbor defect pair in SiO_2.* Physical Review B, **42**(15):9664–9673, 1990.

[SSB+00] Y. Sikorski, A. A Said, P. Bado, R. Maynard, C. Florea, and K. A Winick. *Optical waveguide amplifier in nd-doped glass written with near-IR femtosecond laser pulses.* Electronics Letters, **36**(3):226–227, 2000.

[SSM11] Y. Shimotsuma, M. Sakakura, and K. Miura. *Manipulation of optical anisotropy in silica glass.* Optical Materials Express, **1**(5):803–815, 2011.

[ST77] P. N. Sen and M. F. Thorpe. *Phonons in AX_2 glasses: From molecular to band-like modes.* Physical Review B, **15**(8):4030–4039, 1977.

[STI96] L. Skuja, K. Tanimura, and N. Itoh. *Correlation between the radiation-induced intrinsic 4.8 eV optical absorption and 1.9 eV photoluminescence bands in glassy SiO_2.* Journal of Applied Physics, **80**(6):3518–3525, 1996.

[STS+11] M. Sakakura, M. Terazima, Y. Shimotsuma, K. Miura, and K. Hirao. *Thermal and shock induced modification inside a silica glass by focused femtosecond laser pulse.* Journal of Applied Physics, **109**(2):023503, 2011.

[SvdL00] K. Sokolowski-Tinten and D. von der Linde. *Generation of dense electron-hole plasmas in silicon.* Physical Review B, **61**(4):2643–2650, 2000.

[SWH+08] J. Song, X. Wang, X. Hu, Y. Dai, J. Qiu, Y. Cheng, and Zh. Xu. *Formation mechanism of self-organized voids in dielectrics induced by tightly focused femtosecond laser pulses.* Applied Physics Letters, **92**(9):092904, 2008.

[Tem04] V.V. Temnov. *Ultrafast laser-induced phenomena in solids studied by time-resolved interferometry.* PhD thesis, University of Duisburg-Essen, 2004.

[Tho83] M.F. Thorpe. *Continuous deformations in random networks.* Journal of Non-Crystalline Solids, **57**(3):355–370, 1983.

[THS08] R. Taylor, C. Hnatovsky, and E. Simova. *Applications of femtosecond laser induced self-organized planar nanocracks inside fused silica glass.* Laser & Photonics Reviews, **2**(1-2):26–46, 2008.

[TKD01] M. G. Tucker, D. A. Keen, and M. T. Dove. *A detailed structural characterization of quartz on heating through the alpha-beta phase transition.* Mineralogical Magazine, **65**(4):489–507, 2001.

[Too46] A. Q. Tool. *Relation between inelastic deformabilty and thermal expansion of glass in its annealing range.* Journal of the American Ceramic Society, **29**(9):240–253, 1946.

[Tru86] A. N. Trukhin. *Luminescence of fused silica containing sodium.* physica status solidi (a), **93**(2):K185–K190, 1986.

[Tsa95] T. Y. F. Tsang. *Optical third-harmonic generation at interfaces.* Physical Review A, **52**(5):4116–4125, 1995.

[TSZ+06] V. V. Temnov, K. Sokolowski-Tinten, P. Zhou, A. El-Khamhawy, and D. von der Linde. *Multiphoton ionization in dielectrics: Comparison of circular and linear polarization.* Physical Review Letters, **97**(23):237403, 2006.

[Ure04] H. Urey. *Spot size, depth-of-focus, and diffraction ring intensity formulas for truncated gaussian beams.* Applied Optics, **43**(3):620–625, 2004.

[VSR66] K. Vedam, E. D. D. Schmidt, and R. Roy. *Nonlinear variation of refractive index of vitreous silica with pressure to 7 Kbars.* Journal of the American Ceramic Society, **49**(10):531–535, 1966.

[Wal81] G. E. Walrafen. *Raman spectrum of pressure compacted fused silica.* The Journal of Chemical Physics, **74**(9):5328–5330, 1981.

[web] http://webmineral.com/. Mineralogy Database.

[Wei00] A. M. Weiner. *Femtosecond pulse shaping using spatial light modulators.* Review of Scientific Instruments, **71**(5):1929–1960, 2000.

[WH86] G. E. Walrafen and M. S. Hokmabadi. Raman structural correlation from stress-modified and bombarded vitreous silica. In *Structure and Bonding in Noncrystalline Solids* edited by G. E. Walrafen and A. G. Revesz, pp. 185–202. Plenum Press, 1986.

[WJS+99] M. Watanabe, S. Juodkazis, H.B. Sun, S. Matsuo, and H. Misawa. *Luminescence and defect formation by visible and near-infrared irradiation of vitreous silica.* Physical Review B, **60**(14):9959–9964, 1999.

[WNCT02] M. Will, S. Nolte, B. N. Chichkov, and A. Tünnermann. *Optical properties of waveguides fabricated in fused silica by femtosecond laser pulses.* Applied Optics, **41**(21):4360–4364, 2002.

[WS98] S. Wang and J. F. Stebbins. *On the structure of borosilicate glasses: a triple-quantum magic-angle spinning ^{17}O nuclear magnetic resonance study.* Journal of Non-Crystalline Solids, **231**(3):286–290, 1998.

[YB78] Y.H. Yun and P.J. Bray. *Nuclear magnetic resonance studies of the glasses in the system $Na_2O{\cdot}B_2O_3{\cdot}SiO_2$.* Journal of Non-Crystalline Solids, **27**(3):363–380, 1978.

[Zac32] W. H. Zachariasen. *The atomic arrangement in glass.* Journal of American Chemical Society, **54**(10):3841–3851, 1932.

[ZAF+06] L. Zheng, Q. An, R. Fu, S. Ni, and S.N. Luo. *Densification of silica glass at ambient pressure.* The Journal of Chemical Physics, **125**(15):154511, 2006.

[ZLS04] L. Zheng, J.C. Lambropoulos, and A.W. Schmid. *UV-laser-induced densification of fused silica: a molecular dynamics study.* Journal of Non-Crystalline Solids, **347**(1–3):144–152, 2004.

[ZRG+06] A. Zoubir, C. Rivero, R. Grodsky, K. Richardson, M. Richardson, T. Cardinal, and M. Couzi. *Laser-induced defects in fused silica by femtosecond IR irradiation.* Physical Review B, **73**(22):224117, 2006.

[ZRR+04] A. Zoubir, M. Richardson, C. Rivero, A. Schulte, C. Lopez, K. Richardson, N. Hô, and R. Vallée. *Direct femtosecond laser writing of waveguides in As_2S_3 thin films.* Optics Letters, **29**(7):748–750, 2004.

List of publications

Publications in refereed journals

G. Cheng, K. Mishchik, C. Mauclair, E. Audouard, and R. Stoian, *Ultrafast laser photoinscription of polarization sensitive devices in bulk silica glass*, Optics Express 17, no. 12: 9515-9525, (2009).

K. Mishchik, G. Cheng, G. Huo, I.M. Burakov, C. Mauclair, A. Mermillod-Blondin, A. Rosenfeld, Y. Ouerdane, A.Boukenter, O.Parrieux, and R. Stoian, *Nanosize structural modifications with polarization functions in ultrafast laser-irradiated bulk fused silica*, Optics Express 18, no. 24: 24809-24824, (2010).

C. Mauclair, K. Mishchik, A. Mermillod-Blondin, A. Rosenfeld, I. V. Hertel, and R. Stoian *Optimization of the energy deposition in glasses with temporally-shaped femtosecond laser pulses*, Phys. Proc. 12, 76 (2011).

C. Mauclair, M. Zamfirescu, J.P. Colombier, G. Cheng, K. Mishchik, E. Audouard, and R. Stoian. *Control of ultrafast laser-induced bulk nanogratings in fused silica via pulse time envelopes*, Optics Express, accepted.

Publications in proceedings

R. Stoian, A. Mermillod-Blondin, C. Mauclair, G. Cheng, K. Mishchik, J.P. Colombier, A. Rosenfeld, N.M. Bulgakova, Yu.P. Meshcheryakov, N. Huot, E. Audouard, *Adaptive spatio-temporal techniques for smart ultrafast laser processing of optical glasses*, ICALEO proceedings, Laser Institute of America (2009).

K. Mishchik, G. Cheng, C. Mauclair, E. Audouard, Y. Ouerdane, A. Boukenter and R. Stoian, *Ultrafast laser photoinscription of polarization sensitive devices in bulk silica glass*, OSA Proceedings, BGPP (2010).

C. Mauclair, K. Mishchik, A. Mermillod-Blondin, J. Bonse, A. Rosenfeld, I.V. Hertel, E. Audouard, R. Stoian, *Time-resolved observation of energy deposition in fused silica by utrashort laser pulses in single and cumulative regime*, OSA Proceedings, CLEO (2010).

R. Stoian, G. Cheng, C. Mauclair, A. Mermillod-Blondin, K. Mishchik, E. Audouard, A. Rosenfeld, and I. V. Hertel *3D adaptive spatio-temporal control of laser-induced refractive index changes in optical glasses*, SPIE Proceedings, Photonics West (2011).

Participation in conferences

BGPP2010, oral presentation, *Ultrafast laser photoinscription of polarization sensitive devices in bulk silica glass*, Advanced Optics, Bragg Gratings, Photosensitivity and Poling in Glass Waveguides, Karlsruhe, 2010.

ALT2011, oral presentation, *Structural modifications in bulk fused silica after interaction with ultrashort laser pulses*, Advanced Laser Technologies, Golden Sands, 2011.